MSc Thesis

Improved modeling of propeller-wing interactions with a lifting-line approach

Investigation of a suitable correction method to account for the finite slipstream height

Robert Nederlof

Delft University of Technology

Challenge the future

Cover image: D. Cherkasov; `https://www.airliners.net`

Improved modeling of propeller-wing interactions with a lifting-line approach

Investigation of a suitable correction method to account for the finite slipstream height

by

Robert Nederlof

to obtain the degree of

Master of Science
in Aerospace Engineering

at the Delft University of Technology,
to be defended publicly on Wednesday May 13, 2020 at 13:00.

Student number:	4204271	
Thesis committee:	Prof. Dr. Ing. G. Eitelberg	TU Delft, chair and supervisor
	Dr. Ir. T. Sinnige	TU Delft, daily supervisor
	Prof. Dr. Ir. L. L. M. Veldhuis	TU Delft
	Dr. Ir. S. J. Hulshoff	TU Delft

Acknowledgments

This thesis report marks the end of my Master program in Aerospace Engineering at Delft University of Technology. It has been a challenging but fulfilling period of my life and it has given me the opportunity to pursue my passion in aerospace. In the FPP master track, I was able to combine my interest in both propulsion systems and aerodynamics and this thesis provided me with the opportunity to perform research on the subject of propeller-wing interactions.

I would like to thank my daily supervisor Dr. Tomas Sinnige for his help, comments, ideas and feedback on my work. The meetings we had were always very useful and interesting, and provided me with the right steps to finish my thesis. Furthermore, thanks to Prof. Georg Eitelberg for his assistance along the way and his critical attitude during our discussions, which helped to improve my understanding of the subject.

Many thanks to my fellow students in room NB1.09, who were always very friendly and helpful in the numerous discussions we had, even though the subject was not always study related. Above all, I would like to thank my parents Fred and Franny and my girlfriend Denise who always supported me in the past years and encouraged me to achieve my goals.

Robert Nederlof
Dordrecht, May 2020

Summary

In the current age of noticeable climate change and accompanying impact on the environment, it is necessary to reduce the fuel consumption of aircraft even further. Especially since the aviation sector keeps on growing together with the world population. The use of propeller propulsion can benefit this process, due to its higher propulsive efficiency compared to jet engines. Furthermore, propellers are easy to scale and could be used in the form of distributed propulsion systems, possibly in combination with an electric energy source such as batteries, since propellers can easily be driven by electric motors. The problem is the energized and swirling flow behind the propeller that washes over the wing, the so-called slipstream. The slipstream influences the local lift and drag of the wing and needs to be modeled properly to be able to optimize propeller-wing interaction and to increase the total efficiency of the aircraft.

The increased axial velocity in the slipstream results in an increase in lift of the wing segments behind the propeller. The rotational momentum introduced in the flow, results in a circumferential velocity field in the slipstream, which is known as swirl and this also influences the lift distribution. The tangential flow of the slipstream creates an upwash at the wing segments behind the up-going blade side, effectively increasing the local angle of attack. This results in an increase of lift, while on the down-going blade side, the opposite happens. The effective angle of attack is decreased and therefore the lift. The spanwise position of the propeller has a large impact on the effect of the swirl component. In this thesis, only the time-averaged effects of the propeller on the wing lift distribution are considered.

In the use of modern optimization frameworks, a quick and reliable tool is needed to model the aerodynamics instead of time consuming CFD analyses. Therefore, often a low-fidelity tool, based on potential flow aerodynamics, is used in these frameworks. The potential flow tools are often based on the use of horseshoe vortices, such as the lifting line method and the vortex lattice method. Unfortunately, in the modeling of propeller-wing interactions, discrepancies are found between the low-fidelity tools and the high-fidelity validation data such as from CFD analyses and wind tunnel experiments and these are quite substantial. This is possibly due to the fact that the potential flow theory does not incorporate the varying inflow velocity field as seen by a specific wing segment in the slipstream. In these methods, an infinite height of the propeller slipstream is assumed at each 2D slice. The finite slipstream height in reality will influence the sectional lift and will therefore alter the impact of the propeller-wing interaction on the wing lift distribution. The aim of this thesis is to come up with a potential flow method that accounts for the effect of finite propeller slipstream dimensions on the lift distribution of the wing. Therefore, the emphasis lies on finding a correction method for the axial induced component of the slipstream and hence most of the analyses performed only include the axial velocity increase of the slipstream. These methods will be validated using CFD simulations.

A lifting-line method was chosen to model the propeller-wing interaction and this strip method was adjusted to account for the finite slipstream dimensions. Both 2D and 3D potential flow methods were investigated to include the effect of the slipstream boundaries on the lift distribution. Firstly, the lifting-line method was adjusted using a 2D correction method to alter the sectional aerodynamics of each strip to include the effect of the finite slipstream height. To model the finiteness of the slipstream of the propeller in 2D, the same approach is taken as in the case of an airfoil close to a velocity discontinuity. An example of this application is the wing in ground effect and this is modeled by the use of images to satisfy the boundary conditions at the discontinuity. This image method can be extended to account for two dividing streamlines, as is the case for the airfoil submerged in a jet, as found in the work by L. Ting. The circulation distribution, which represents the 2D thin airfoil, is reflected in the two dividing streamlines at the edges of the slipstream and these reflections are also reflected again and this process is theoretically extended to infinity. The strength of the reflected images is scaled compared to the original circulation and is related to the velocity jump across the jet boundaries. The system of equations can be solved using linear algebra techniques and a correlation between the lift and the slipstream height is found. Using this method, the correction factor can be applied to the sectional lift coefficient and this can then be used in the adjusted lifting-line tool.

Secondly, two more advanced 3D correction methods were investigated to also account for the spanwise boundary of the slipstream and its effect on the lift distribution. To use these 3D correction methods, the lifting-line approach was improved to a single panel vortex lattice method to be able to include the induced velocity effect of the bound vortex. The first of two 3D image correction methods is the intermediate 3D image approach. The images defined in the 2D correction approach are placed as extra components in the lattice of horseshoe vortices. The vertical position of these images above and below the wing was determined by the sectional propeller slipstream height, as was done in the 2D case. However, by adding the images in 3D, their downwash is also affecting the neighboring segments.

The second of the two and most complete method of the three correction methods is referred to as the full 3D image method. To fully include the disturbance effect of the bound vortex on the slipstream boundaries, the images must be defined differently compared to the 2D case. The used method, which was derived by S. Rethorst, divides each horseshoe vortex in an even and odd part. The even system of vortices is similar to the 2D approach, where the location and strength of the images compared to the original locations is easily determined. However, the odd system, which models the effect of the bound vortex part of each horseshoe vortex on the downwash of the wing, is more complicated. Bessel functions were used to determine the influence of the odd system and this was added to the influence of the even part. All the three mentioned correction methods are limited to the analysis of axial propeller slipstreams only. Unfortunately, the equations of this method were derived with the assumption of symmetry, meaning that only propeller slipstreams can be analyzed which are in the middle of the wing. No current method exists to account for the finiteness of the swirl velocity component.

The different correction methods were validated using CFD simulations, which were set up such as to approximate the potential flow and hence to discard any viscosity. A very fine mesh was needed to avoid the production of numerical viscosity and a grid convergence study was performed both in 2D and 3D to determine the discretization error. The data from the 2D CFD analyses showed good agreement with the potential flow analysis result. Therefore, it was hypothesized that the 2D correction method could be used to improve the 3D lifting-line analysis by applying the correction to each wing segment using the local slipstream height as input. However, this application of the 2D correction method into the adjusted lifting-line analysis did not lead to satisfactory results. The wing lift in the axial jet was still largely over-predicted compared to the CFD simulations.

The intermediate 3D image method showed an increase in correction and hence a decrease in local lift coefficient in the jet region compared to the adjusted lifting-line method. However, the decrease was not substantial and still a large over-prediction was present compared to the CFD data. The shortcomings of this intermediate method were emphasized by an analysis of a rectangular jet of finite width, but with an infinite height. This hypothetical jet would not result in any image corrections, since the vertical slipstream boundary is infinitely far away. However, the results of this analysis also did not show agreement with the results of a similar CFD simulation. Finally, the full 3D image method was validated using the results of the CFD simulations. The results of this third correction method showed remarkably good agreement with the CFD simulations and the method overcomes the shortcomings of the adjusted lifting-line and the intermediate 3D image method. To investigate the restriction of the full 3D image method, CFD simulations were performed in which the propeller slipstream was not located in the middle of the wing. The analysis results also showed good agreement with these simulations. This is due to the fact that created downwash of the jet boundary is large close to it, but quickly becomes negligible compared to the created downwash of the original horseshoe vortices when moving away from the jet.

In conclusion, the results of the full 3D image method show a good agreement with the CFD data of an axial jet. The method also seems to be useful for non-symmetrical cases, even though the equations were derived for the case of a symmetric propeller-wing interaction. Unfortunately, the method does not account for the swirl component in the slipstream and future research should be conducted to come up with a correction factor for this slipstream component. However, the full 3D image method is a fast and accurate addition to the existing potential flow modeling tools and the method can be used in future optimization frameworks, which will yield more accurate results, increasing the efficiency of the installed propeller-wing system. This can aid in the challenge of reducing fuel consumption of aircraft even further and to make for a greener world.

Contents

List of Figures

List of Tables

List of Symbols and Abbreviations

Symbol	**Description**	**Unit**
Greek Symbols:		
α	Angle of attack	[°]
α_{0_L}	Zero-lift angle of attack	[°]
α_{eff}	Effective angle of attack	[°]
α_g	Geometric angle of attack	[°]
α_i	Induced angle of attack	[°]
α_p	Swirl induced angle of attack	[°]
α_t	Twist angle	[°]
α_v	Velocity coefficient for U_1 & U_2	[-]
β	Velocity correction factor U_1 & U_3	[-]
β_v	Velocity coefficient for U_1 & U_3	[-]
γ	Distributed vorticity	[m/s]
ϵ_h	Discretization error	[%]
ϵ_{rel}	Relative error	[%]
ζ	Non-dimensionalized z-coordinate (z/R_p)	[-]
η	Non-dimensionalized y-coordinate (y/R_p)	[-]
η_p	Propulsive efficiency	[-]
θ	Circumferential position at airfoil	[rad]
θ_p	Pitch angle	[rad]
λ	Variable of integration in Bessel functions	[-]
λ_β	Variable of integration for the running variable z in Bessel functions	[-]
μ	Jet velocity ratio (V_∞/V_j)	[-]
ν	Order of Bessel function	[-]
ξ	Non-dimensionalized x-coordinate (x/R_p)	[-]
ρ_∞	Free stream density	[kg/m^3]
ς	Complex coordinate of horseshoe vortex	[-]
ϕ	Velocity potential function	[-]
φ	Angular location at airfoil	[rad]
ψ	Stream function	[-]
ω	Propeller angular velocity	[rad/s]
Roman Symbols:		
A_{disk}	Area of the propeller disk	[m^2]
A_m	Fourier coefficient m of the distributed vorticity	[-]
a	Distance from airfoil to upper domain	[m]
a_p	Axial inflow factor	[-]
b	Distance from airfoil to lower domain	[m]
b_p	Angular (swirl) inflow factor	[-]
C_D	3D drag coefficient	[-]
C_L	3D lift coefficient	[-]
C_d	2D drag coefficient	[-]
C_l	2D lift coefficient	[-]
C_{l_∞}	Lift coefficient of the airfoil in the classical case (no slipstream)	[-]
C_{l_j}	Lift coefficient of the airfoil submerged into a slipstream with finite height	[-]
C_T	Thrust coefficient	[-]
C_P	Power coefficient	[-]
c	Chord	[m]
D	Drag	[N]

D_i	Lift induced drag	[m]
D_p	Propeller diameter	[m]
d	Distance from velocity discontinuity	[m]
d_m	Fourier coefficient m of camber line	[-]
e	Spanwise location of the left horseshoe vortex edge	[-]
e_k	Indicator for image vortex location k	[m]
F_{ij}	Horseshoe vortex influence coefficient	[-]
F_k	Indicator for image vortex strength k	[-]
f	Spanwise location of the right horseshoe vortex edge	[-]
G_{ij}	Jet boundary influence coefficient	[-]
h/c	Slipstream to chord ratio	[-]
h	Height of middle domain/slipstream	[m]
h_i	Typical cell size of grid i	[m]
I	Number of airfoil elements	[-]
I_v	Modified Bessel function of the first kind with order v	[-]
I'_v	Derivative of the modified Bessel function of the first kind with order v	[-]
J	Advance ratio	[-]
J_m	Influence integral of Fourier coefficient m	[-]
K_v	Modified Bessel function of the second kind with order v	[-]
K'_v	Derivative of the modified Bessel function of the second kind with order v	[-]
K_{C_l}	Lift coefficient correction factor (C_{l_j}/C_{l_∞})	[-]
K_l	Sectional lift ratio (l_j/l_∞)	[-]
L	Lift force	[N]
l	Sectional lift force	[N/m]
l_∞	Sectional lift force of the airfoil in the classical case (no slipstream)	[N/m]
l_j	Sectional lift force of the airfoil submerged into a slipstream with finite height	[N/m]
M	Number of Fourier coefficients	[-]
$m(x)$	Slope of airfoil camber line at location x	[-]
$\dot{m}$	Mass flow rate	[kg/s]
N	Number of image reflection sets	[-]
N_b	Number of propeller blades	[-]
n	Propeller rotational speed	[rps]
P	Propeller power	[W]
p	Pressure	[Pa]
p_∞	Pressure in the free stream	[Pa]
p_1	Pressure in front of the propeller disk	[Pa]
p_2	Pressure behind of the propeller disk	[Pa]
p_j	Pressure in the slipstream	[Pa]
Q	Propeller torque	[Nm]
R	Resultant aerodynamic force	[N]
R_{hub}	Propeller hub radius	[m]
R_p	Propeller radius	[m]
r	Radial location along propeller	[m]
T	Propeller thrust	[N]
U	Velocity in the x-direction	[m/s]
U_1	Velocity of the middle domain	[m/s]
U_2	Velocity of upper domain	[m/s]
U_3	Velocity of lower domain	[m/s]
u	Disturbance velocity in x-direction	[m/s]
u_p	Upstream x-location of propeller	[m]
V	Velocity	[m/s]
V_∞	Free stream velocity	[m/s]
V_Ω	Tangential velocity at blade element	[m/s]
V_a	Axial velocity behind propeller	[m/s]
V_b	Total velocity at blade element	[m/s]
V_{eff}	Effective free stream velocity	[m/s]

V_{disk}	Velocity at the propeller disk	[m/s]
V_j	Jet velocity	[m/s]
V_l	Local inflow velocity at wing segment	[m/s]
V_r	Radial velocity behind the propeller	[m/s]
V_t	Tangential (swirl) velocity behind propeller	[m/s]
V_x	Velocity in the x-direction	[m/s]
V_y	Velocity in the y-direction	[m/s]
V_z	Velocity in the z-direction	[m/s]
v	Disturbance velocity in y-direction	[m/s]
w	Vorticity	[m^2/s]
x	Streamwise direction	[m]
Y_{jk}	Location coefficient for image vortex j, k	[-]
y	Vertical direction	[m]
z	Spanwise direction	[m]

Abbreviations & Acronyms	**Description**
$1D$	One-Dimensional
$2D$	Two-Dimensional
$3D$	Three-Dimensional
AD	Actuator Disk
AR	Aspect Ratio
$AIAA$	American Institute of Aeronautics and Astronautics
$APIAN$	Advanced Propulsion Integration Aerodynamics and Noise
BEM	Blade Element Momentum
CFD	Computational Fluid Dynamics
KJ	Kutta-Joukowski
LE	Leading Edge
LL	Lifting Line
$NASA$	National Aeronautics and Space Administration
NS	Navier-Stokes (equations)
PDE	Partial Differential Equation
$RANS$	Reynolds-Averaged Navier–Stokes (equations)
Re	Reynolds number
$SCEPTOR$	Scalable Convergent Electric Propulsion Technology Operations Research
SRF	Swirl Recovery Factor
SRV	Swirl Recovery Vane
TE	Trailing Edge
VLM	Vortex Lattice Method

1

Introduction

Increasing fuel prices and efforts to reduce climate effects have led to the importance of reducing fuel consumption of aviation even more. One way to reduce fuel consumption is to 'switch back' to propeller propulsion. Propellers have higher propulsive efficiency than jet engines and hence consume less fuel [1]. Furthermore, the use of propellers allows for the implementation of distributed propulsion systems, which could further reduce fuel consumption. The flow behind the propeller is a swirling and energized flow, which will have its influence on the trailing surfaces, amongst others, the main wing.

The propeller-wing interaction can be beneficial for the lifting performance due to the increase in axial velocity in the slipstream. Distributed leading edge propellers can be used as means of high-lift augmentation, while they can be stowed during cruise to increase aerodynamic efficiency. Two examples of such designs can be seen in Figure 1.1. Furthermore, the propulsive performance of the aircraft can be improved due to the recovery of slipstream swirl by the wing [2]. To capture these aerodynamic effects, it is important that the influence of the propeller on the wing is understood correctly and can be analyzed properly. Already in the time of Prandtl, wind tunnel experiments were performed to investigate this interaction and in the 80's, when fuel prices increased, it was noted that the swirl recovery could result in a significant reduction in induced drag [3].

(a) The APIUS i-6 [4]

(b) The SCEPTOR 9 passenger commuter [5]

Figure 1.1: Conceptual designs of electrical distributed propeller aircraft

The use of CFD analyses or wind tunnel experiments for the designing and testing of new models, is time-wise very expensive. It is impossible to test hundreds of different configurations to find a propeller-wing design with the highest efficiency gain, since this will simply take too long. So there is a need for fast and accurate optimization tools, from which the best possible configuration can be designed and tested in a wind tunnel. The design tools developed previously at Delft University of Technology [2, 6–8] are mainly based on simple 2D and 3D potential flow analysis. The tools have proven to be able to generate wing designs which indeed increase the total propulsive efficiency.

However, there are still discrepancies between the results from the tools and high-fidelity validation data, such as CFD simulations and wind tunnel tests, and it is not known precisely where these discrepancies come from. The potential flow tools show in general an over-estimation of the propeller induced velocities. Most often, an empirical correction factor without much physical substantiation was applied to correct for these errors [2, 6, 9]. Since the wing recovers part of the incoming swirl, it was thought that the wing would not experience the full increase in tangential velocity due to the swirl component in the slipstream [2]. Therefore, a so-called swirl recovery factor was calculated, based on the decrease in tangential momentum, and applied to reduce the effective angle of attack. Furthermore, it turned out that also a correction factor for the axial velocity component was needed, since the swirl recovery factor alone was not sufficient to account for the discrepancies at higher axial slipstream velocities [6].

Most of the propeller-wing interaction models have been based on the application of the lifting-line theory or the vortex lattice method. These methods make use of several potential flow assumptions such that the inflow field is assumed to be infinitely high and uniform. However, the flow behind the propeller is not uniform in any direction and the slipstream has a finite extent due to the finite propeller dimensions. The flow field around each wing segment behind the propeller will look more like the representation in Figure 1.2. Here, only the axial component of the propeller slipstream is shown for simplicity. It turns out that the influence of the propeller slipstream on the lift distribution is greatly dependent on the relative scales of the chord and the slipstream [10].

In the figure, V_j denotes the increased axial slipstream velocity, while V_∞ represents the freestream velocity. Furthermore, the important geometric aspect of the flow field is the height of the slipstream (h) in relation to the airfoil chord (c). The existing models do not account for this effect and this may explain the observed discrepancies with the validation data. Therefore, the main aim of this thesis is to investigate different potential flow methods that can be used to correct the existing models, such that they account for the effect of the slipstream boundaries. By validating these correction methods, the best one can be used for the 3D propeller-wing analysis. If the correction methods could reduce the discrepancies between the potential flow tools and high-fidelity results, better optimized wing shapes can be designed and these can aid in reducing the fuel consumption of propeller powered aircraft in the future.

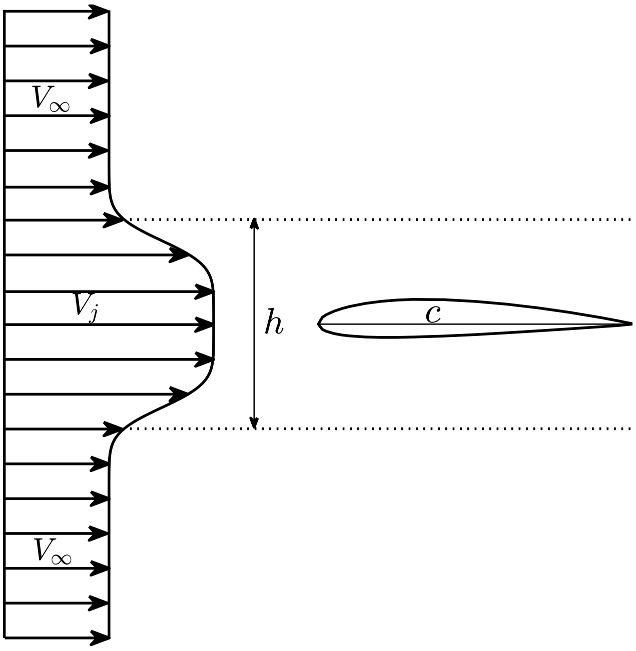

Figure 1.2: Schematic representation of the non-uniform inflow field

Research Aim and Objectives

The lack of proper understanding of the effects of the finite size of the propeller slipstream together with the current discrepancies between the low-fidelity lifting-line and vortex lattice method design tools and the high-fidelity CFD results and wind tunnel experimental data lead to the following research objective:

> *Investigate the effects of the propeller slipstream dimensions on the potential flow propeller-wing modeling, by finding a potential flow correction method which is able to capture the influence of the non-uniform inflow field of the wing.*

To reach the objective, the following research question and subsequent sub-questions were defined:

- What is the effect of the finite height and width of the slipstream on the wing lift distribution in the potential flow modeling of propeller-wing interaction?
    - How does the inflow field of the wing look like?
    - How is the propeller-wing interaction modeled in current potential flow methods?
    - Which different 2D methods exist to include the effect of the finite slipstream height on the airfoil lift?
    - What is the accuracy of these methods compared to CFD results?
    - Which different methods exist to adjust the wing lift distribution to account for the propeller slipstream boundaries in 3D?
    - What is the accuracy of the adjusted 3D potential flow tools compared to CFD results?
    - What is the difference between applying 2D and 3D correction methods to the potential flow modeling of the propeller-wing interaction?

To find an answer to these questions, the current existing propeller-wing analysis tools must be investigated in order to identify the shortcomings. Most of the tools are based on potential flow analysis, so the assumptions and shortcomings of this theory should be discussed. Furthermore, the shape and velocity profile of the propeller slipstream needs to be determined and hence knowledge of slipstream modeling is needed. Once the shortcomings of the existing models are known, a correction method must be found that can account for these shortcomings and can reduce the over-prediction of the propeller induced velocities.

The next step is to implement the correction model into the existing wing analysis tools and validate the consistency of the results by CFD simulations using Ansys. The aim is to provide a validity of the correction methods, so these can be implemented in design and optimization processes in the future. In this way, further optimized propeller aircraft designs could be made which help in the process of reducing fuel consumption even further.

Research Outline

The body of this thesis consist of three parts and containing a total of eleven chapters. The order of the chapters can be seen in the roadmap presented in Figure 1.3. After this introduction, Part I contains primarily background information on the potential flow modeling of propeller slipstreams and the effect of the induced velocities on the lift distribution of a wing. The principles of propellers and their influence on the lifting surfaces is treated in Chapter 2, followed by Chapter 3 which presents the modeling aspects and the current shortcomings of the analysis tools, which could be the origin of the discrepancies.

Thereafter, Part II can be found which focuses on the 2D analysis of an airfoil submerged in a slipstream. An approach to model the effect of the slipstream height on the lift of a 2D airfoil is presented in Chapter 4. Also, a convergence and parametric study is done to better understand the numerical nature of the applied method. This correction method had to be validated and therefore it was chosen to use CFD simulations. The setup of the 2D simulations is discussed in Chapter 5, after which the results of these simulations are presented in Chapter 6.

After the validation of the 2D correction method, Part III begins, which is about the 3D modeling of the propeller-wing interactions. First, it is discussed how the 2D correction method can be applied to the existing lifting-line tools in Chapter 7. Furthermore, two other correction methods are discussed which are 3D in nature. These tools have to improve the lift correction for the wing analysis, compared to the application of the 2D correction model. The two models range in complexity and are discussed in Chapter 8. The three presented propeller-wing correction models also had to be validated and this was done using CFD again. The setup of the 3D simulations is discussed in Chapter 9. Chapter 10 treats the results of the 3D validation process and shows which correction model is the most accurate. The thesis is finalized with the conclusions in Chapter 11, together with the recommendations for future work.

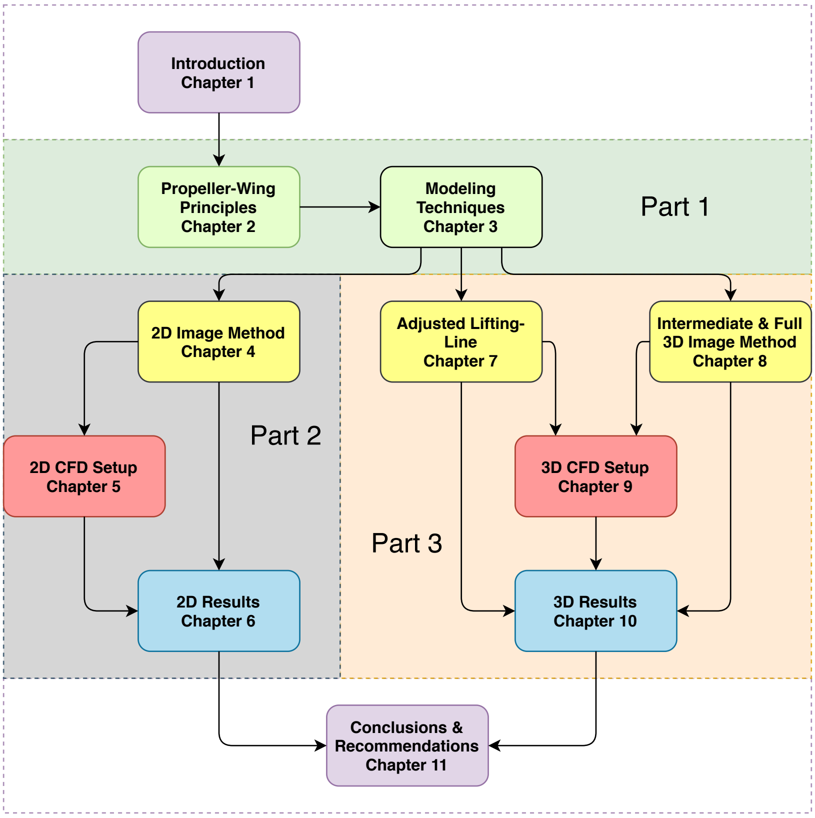

Figure 1.3: Thesis roadmap

Part I
Background Theory

In this first part, the focus is put on the understanding of the propeller slipstream and the interaction of it with lifting surfaces and vice versa. Firstly, the fundamentals of the propeller-wing interaction is discussed in Chapter 2. The propeller slipstream and the interaction with the main wing can be modeled in different ways and these techniques are presented in Chapter 3.

2

Principles of Propeller-Wing Interaction

This chapter focuses on the basic understanding of propeller propulsion, including the slipstream characteristics and the propeller-wing interaction. In Chapter 3, the modeling of the propeller slipstream and its effect on the spanwise lift distribution is discussed. In Section 2.1, the general principles of propellers are discussed, explaining the high propulsive efficiency. The characteristics of the propeller slipstream are presented in Section 2.2. In Section 2.3, the effects of the propeller slipstream on trailing surfaces are discussed. The opposite effect is elaborated on in Section 2.4.

2.1. Propulsion of Aircraft Using Propellers

Aircraft are generally propelled in two different ways: by the use of propellers or jet engines. Both types rely on the principle that air is accelerated backward to generate thrust. The equation for thrust can be seen in Equation 2.1, where $\dot{m}$ is the mass flow rate through the propulsor, V_j is the outgoing jet velocity and V_∞ is the incoming freestream velocity. Propellers often have a higher propulsive efficiency compared to jet engines having the same weight. This is because the outer cowling is not present, which saves weight and reduces drag, and hence the propeller can be larger in size.

$$T = \dot{m}(V_j - V_\infty) \tag{2.1}$$

$$\eta_p = \frac{2}{1 + \frac{V_j}{V_\infty}} \tag{2.2}$$

For the same amount of thrust, the propeller gives a large amount of air a small increase in velocity, while turbojet engines give a small amount of air a large increase in velocity. The former situation results in high propulsive efficiency, while the latter case results in lower propulsive efficiency. The definition of the propulsive efficiency can be seen in Equation 2.2. This equation is derived from the ratio of propulsive power and the power required to adjust the kinetic energy of the flow. The propeller accelerates air backwards to produce thrust, but by spinning the propeller, also angular momentum is introduced into the slipstream. The resulting angular flow in the slipstream is called the swirl and is a form of energy loss, since this flow does not contribute to the axial velocity increment [11].

To determine the performance of the propeller, the total thrust and power required must be calculated. These parameters of the propeller should be normalized to be able to compare propellers of different sizes and operating conditions. The thrust coefficient (C_T) can be seen in Equation 2.3. In this equation, n is the rotational speed ([revs/s]) of the propeller, ρ_∞ is the freestream density and D_p is the propeller diameter. The power of the propeller (P) is non-dimensionalized in the same manner, see Equation 2.4. To non-dimensionalize the velocity of the propeller, relative to the freestream velocity, the advance ratio is used (J). The definition can be seen in Equation 2.5. Using these propeller coefficients, a different expression for the propulsive efficiency can be defined, see Equation 2.6 [12].

$$C_T = \frac{T}{\rho_\infty n^2 D_p^4} \tag{2.3}$$

$$C_P = \frac{P}{\rho_\infty n^3 D_p^5} \tag{2.4}$$

$$J = \frac{V_\infty}{n\, D_p} \tag{2.5}$$

$$\eta_p = \frac{C_T\, J}{C_P} \tag{2.6}$$

2.2. Propeller Slipstream

The propeller adds axial and tangential momentum into the flow. The flow behind the propeller is therefore different compared to the freestream and this will influence the aerodynamics of lifting surfaces, which are submerged in or in close proximity of the slipstream. Especially for highly loaded propellers, the induced velocities are large and this will significantly alters the lift and drag distribution of these lifting surfaces [2]. Therefore, a detailed understanding of the propeller slipstream is needed to asses its effect on for example the main wing. The slipstream has three main velocity components, being the axial velocity (V_a), tangential or swirl velocity (V_t), and radial velocity (V_r). The velocity components are shortly discussed in Section 2.2.1, 2.2.2 and 2.2.3 respectively.

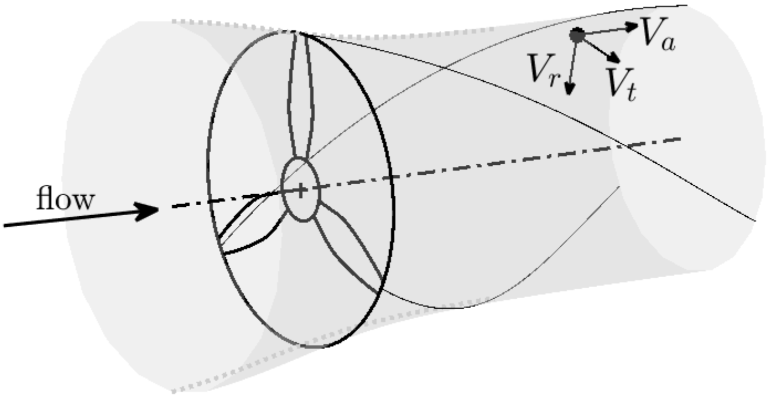

Figure 2.1: Schematic visualization of the propeller slipstream with the relevant velocity components

2.2.1. Axial Velocity

The main velocity component in the propeller slipstream is in the axial direction. This velocity component is creating the actual thrust as discussed in Section 2.1, which is the main function of the propeller. The propeller can be seen as multiple rotating wings, creating a helical vortex system [2]. The axial velocity is a function of the radial position (r) inside the slipstream, since the aerodynamic forces vary along the blade span. A typical distribution of axial velocity behind the propeller can be seen in Figure 2.2. This distribution is based on the circumferential-averaged results of the APIAN propeller analysis and was created using CFD [13, 14]. The velocity components are extracted from a plane parallel to the propeller disk and at a distance of $0.9 \cdot R_p$ behind the propeller. The axial velocity increases while going outward on the blade, but near the tip, it sharply drops to V_∞ due to the loss of lift caused by the pressure equalization and the tip vortex.

2.2.2. Swirl Velocity

The tangential velocity, or swirl, created by the rotation of the propeller is the origin of the helical shape of the slipstream. While varying the propeller loading, the tangential velocity distribution changes, while the axial velocity distribution remains constant [2]. In the axial direction however, there is no change in angular momentum and hence the swirl velocity remains unchanged. On the contrary, the axial velocity changes due to the contraction of the slipstream. This means that the swirl angle, which is defined by the two velocity components mentioned, also varies in the axial direction. A typical tangential velocity distribution along the propeller blade can be seen in Figure 2.2. The leading edge vortex is clearly visible in the tangential velocity distribution, which is the bump at around 75% of the radius. Due to the vortex, the tangential velocity does not directly go to zero at the tip [13].

2.2.3. Radial Velocity

The pressure jump across the propeller results in an acceleration of the slipstream downstream of it. Far away from the propeller, the pressure must be equal to the freestream pressure and hence the axial velocity has to increase to decrease the static pressure. This means that the axial velocity distribution along the radius of the slipstream varies as function of axial position. The increase in axial velocity results in a contraction of the slipstream such that the same mass flow is maintained. This contraction introduces a radial velocity component to the slipstream. The contraction however, is often found to be small and is largest around the propeller disk it self [2]. This means that the radial velocity component further away from the propeller is small and often neglected in the slipstream analysis [13]. Therefore, in this thesis the radial velocity is not taken into account and for the propeller-wing analysis, it is assumed that the slipstream is fully developed. More information regarding the modeling of the propeller slipstream is presented in Section 3.1.

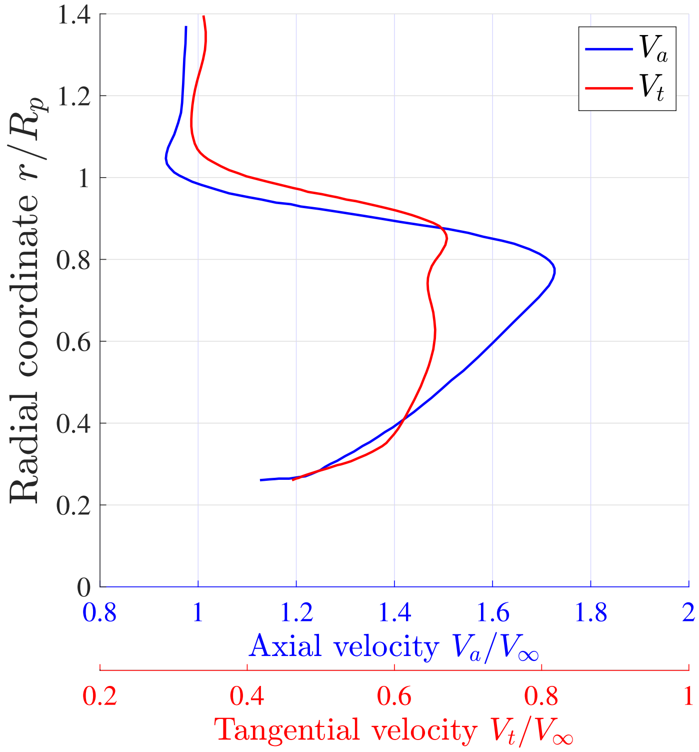

Figure 2.2: Circumferential-averaged axial and tangential velocity components from the APIAN CFD analysis [13]

2.2.4. Slipstream Vorticity

In the propeller slipstream boundary, there is a large amount of vorticity, which is primarily generated due to the tip vortex. The tip vortex streamlines are shown in Figure 2.3a. Next to the tangential velocity, the tip vortex of the blade introduces concentrated vorticity in the slipstream. The concentrated vorticity of the tip vortex can be represented by an isosurface [13]. The isosurfaces of the tip and hub vortex of the APIAN propeller are shown in Figure 2.3b. The velocity is plotted as a contour plot around the isosurfaces, where red indicates high values and blue low values of the velocity. As can be seen, the tip region of the blade has a lower pitch, since the axial displacement per rotation is less than for the hub vortex. The swirling and turbulent wake behind the propeller including the tip and hub vortices will have an influence on any trailing surface.

2.2.5. Steady and Unsteady Effects

The flow characteristics of the slipstream discussed in the previous sections are time dependent. The propeller has a finite number of blades and hence a fixed point in the slipstream will see varying velocity components as the blades pass by. However, the time-averaged effects are most important in the analysis of the influence of the slipstream on the wing performance. The effects of the cyclic variation are often small compared to these averaged effects [2, 13]. The time-averaged effects are mainly inviscid effects, such as increased dynamic pressure (axial flow) and swirl (tangential flow). Therefore, these velocity components are often circumferential-averaged, as was done for the results in Figure 2.2, to remove the time dependency. The unsteady effects that remain are mainly originating from viscous effects such as the tip vortices, as was shown in Figure 2.3. These unsteady effects are more important for the analysis of aeroelasticity aspects, structural vibrations or noise generation [15]. Since the focus in this thesis is put on the effect of the slipstream on the integral wing loading, only time-averaged effects are taken into account.

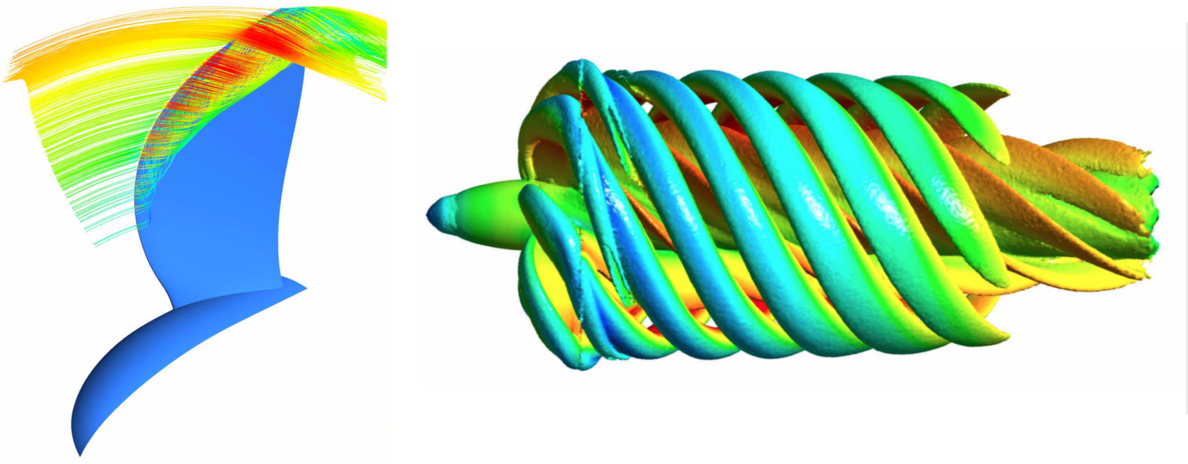

(a) Velocity streamlines of the tip vortex

(b) Vorticity isosurface of the slipstream

Figure 2.3: Velocity streamlines and vorticity isosurface of the APIAN propeller CFD simulation [13]

2.3. Aerodynamic Effects of the Propeller on Trailing Surfaces

The first effect that is reviewed is the influence of the propeller on lifting surfaces behind it. For most aircraft, the propellers are located in front of the main wing, the so-called tractor configuration. For this configuration, the swirling and energized slipstream of the propeller will influence the wing aerodynamic characteristics [2].

2.3.1. Effect on Lift Distribution

The axial and tangential velocity induced by the propeller cause separate effects on the spanwise lift distribution [2]. The two effects are visualized in Figure 2.4, where it was assumed that the propeller was in the center of the wing. For this figure, the non-dimensionalized lift coefficient (C_l) is used on the y-axis. As said, the axial velocity increment increases the lift. This can be seen in Figure 2.4a. In the center of the propeller slipstream, the axial velocity increase is small due to the spinner. The effects of the tangential flow on the C_l-distribution of the wing are visualized in Figure 2.4b. The lift on the propeller down-going side becomes less, while the lift on the up-going side gets bigger. The shape of the C_l-distribution is therefore dependent on the rotation direction [2].

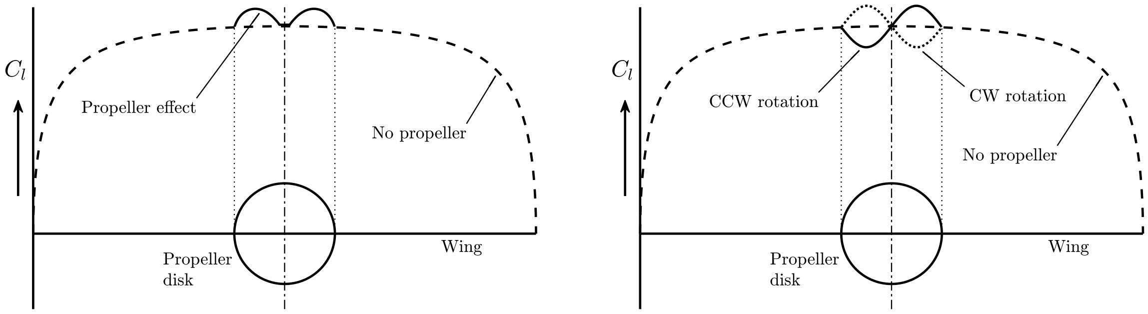

(a) Axial induced velocity effect

(b) Tangential (swirl) induced velocity effect

Figure 2.4: Isolated effects of the propeller induced velocities on the wing lift distribution [2]

The real effects of the axial and tangential velocity are more complicated than just adding the two up. The sudden increase or decrease in lift at the slipstream boundary creates strong trailing vortices. These vortices also influence the surrounding regions. So, the lift of the wing segments not directly submerged in the slipstream are also affected, which on its turn creates a different trailing vortex sheet. This means that the whole lift distribution over the entire span is changed and that the initially large peaks are more spread out [2]. This is schematically visualized for the single prop configuration in Figure 2.5.

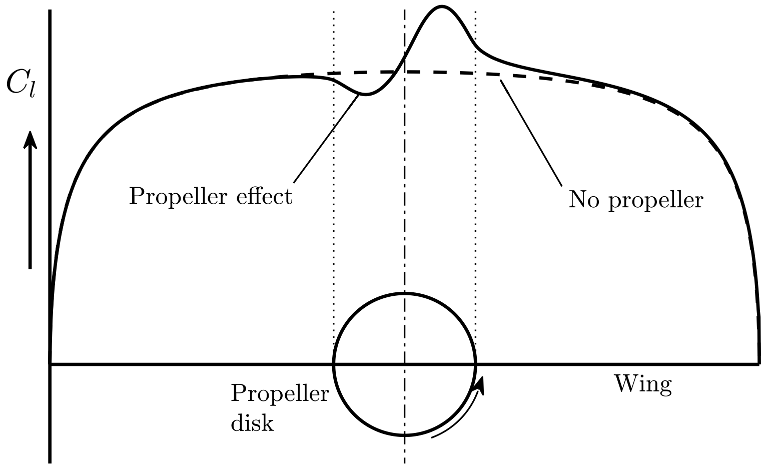

Figure 2.5: Combined effect of the propeller induced axial and tangential velocity on the wing C_l distribution

It shows that the distribution of C_l along the span is not only affected directly behind the propeller. The higher the propeller loading, the larger the axial and tangential induced velocities in the slipstream, and hence the larger the effects on the C_l-distribution. This lift distribution results in a rolling tendency of the aircraft and to counteract this imbalance, some trim of the ailerons in required. This trimming results in more drag of the control surfaces compared to the untrimmed condition and hence a smaller amount of drag reduction in total. For the case presented above, where the propeller is at the symmetry line of the wing (in the middle), the rotation direction does not directly matter. Rotating the propeller the other way around will result in a mirrored distribution compared to the one in Figure 2.5.

2.3.2. Swirl Recovery

The propeller swirl induces regions of different vertical velocity along the wingspan. The wing part behind the up-going side of the propeller is in the upwash of the propeller, whereas the other side of the wing, behind the down-going side, experiences downwash. These vertical velocity components cause a change in the aerodynamics of the 2D airfoil sections. This is visualized in Figure 2.6 [13]. In this figure, the case for both the symmetric and cambered airfoil are shown, assuming that the freestream velocity is parallel to the cord line ($\alpha = 0°$). The vertical component alters the effective angle of attack, while the lift force is still perpendicular to V_∞. For a symmetric airfoil at $\alpha = 0°$, the resultant force in the upwash region is tilted forward and hence the drag force is actually in the direction of the thrust. On the other side, the downwash of the propeller results in a negative resultant force (pointed down) but still rotated forward, resulting in negative drag. The wing recovers part of the swirl and produces a contribution to the thrust [3].

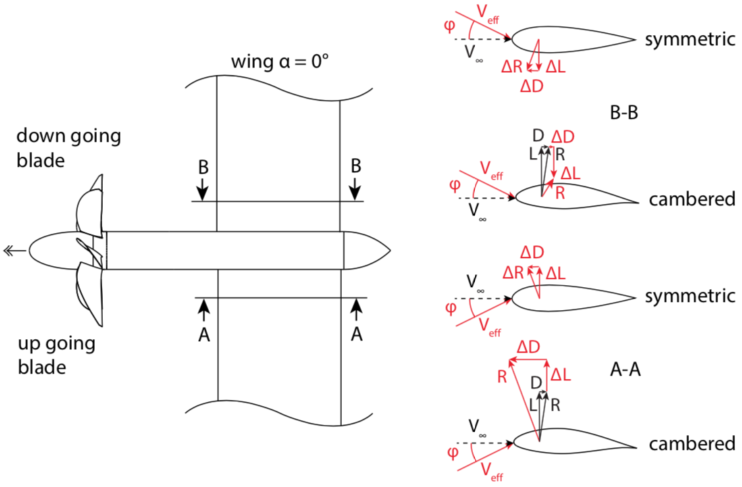

Figure 2.6: Swirl recovery by the main wing [2, 13]

With a cambered airfoil, the situation is slightly different. For the airfoil in the upwash, the resultant force is still augmented and tilted forward. The airfoil in the downwash, however, still has a resultant force in the positive lift direction, but it is reduced and tilted backward. This is due to the fact that cambered airfoils have a non-zero zero-lift angle of attack α_{0_L}. The cambered airfoil will still create positive lift at small swirl angles (φ). The backward tilted force results in more drag, but since the magnitude of it is smaller than compared to the augmented side, the increase in drag is smaller than the decrease in drag in the upwash region. So the net induced drag is still negative and the overall lift is increased due to the increased axial velocity [3]. Since the flow behind the propeller contracts, as shown in Figure 3.2, the axial velocity increases more after the propellers and hence the distance between the propeller and the wing is an important factor.

The swirl recovery of the wing can be investigated by comparing the vertical velocity component in front of the wing with the values behind the wing. To see this effect, a lifting-line code was used, which includes the propeller induced velocities [16]. More information regarding the modeling of the propeller-wing interaction is presented in Section 3.2.2. The used tool assumed a constant cross-sectional axial velocity increase behind the propeller, meaning there is no contraction of the slipstream and hence this induced velocity remains constant in the flow direction. For the swirl component, a sine wave like tangential velocity distribution was used for qualitative purposes only. Depending on the chosen propeller slipstream model, the tangential velocity distribution can look differently. Since the propeller axis is modeled to be on the same plane as the lifting-line, the tangential velocity at the wing is pointing precisely in the vertical (y)-direction. The velocity in this direction is denoted by V_y and the variation along the span can be seen in Figure 2.7. It can be seen that the vertical velocity behind the wing is slightly reduced, indicating swirl recovery.

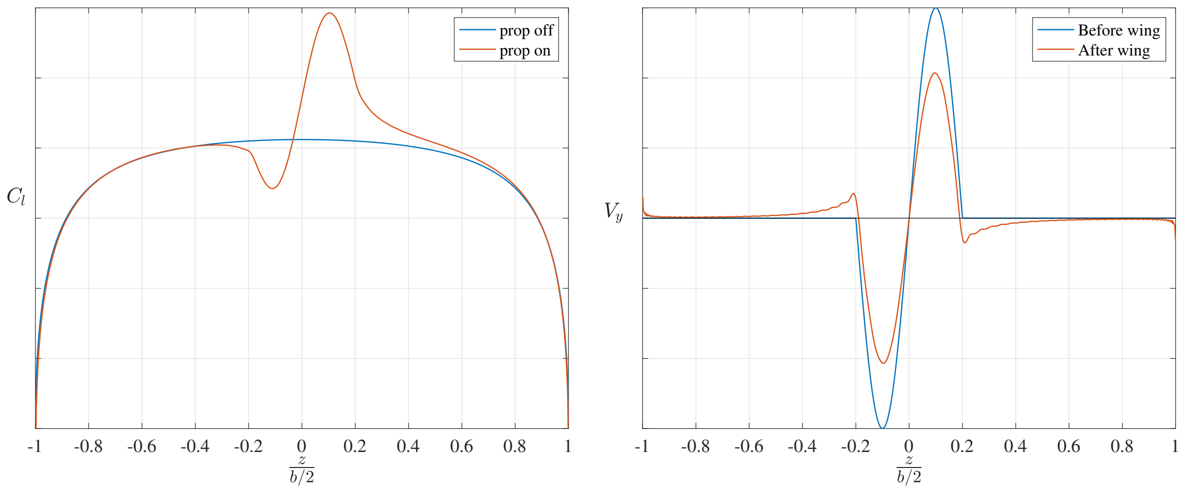

(a) C_l-distribution over the wing

(b) Swirl recovery across the wing

Figure 2.7: Lifting-line tool results including propeller induced velocities [16]

A negative effect of the propeller on the wing is the possible increase in aeroacoustic emissions. This effect is mainly caused by the vortex from the propeller tip. The interaction of the tip vortex with the boundary layer of the wing causes the tip vortex to split at the Leading Edge (LE) and shift while going over the pressure and suction side of the wing. After the Trailing Edge (TE), the two sides do not reattach. Surface pressure measurements revealed that vortex core impingement results in a sudden rise in suction, producing noise and vibrations [17].

2.3.3. Influence of Spanwise Propeller Location

When the propeller is no longer placed at the center of the wing, but somewhere along the mid-span, as is often the case for multi-propeller aircraft, the questions arise if the rotation direction is still irrelevant for the effect on the lift distribution. Spanwise load variation is an important factor for the thrust augmentation [3]. This means that the higher loaded inboard part of the wing can contribute more to the increase of thrust, than the lower loaded outboard part. Hence, the largest reduction in drag can be obtained if the propeller is rotating inboard-up. This is visually shown in Figure 2.8.

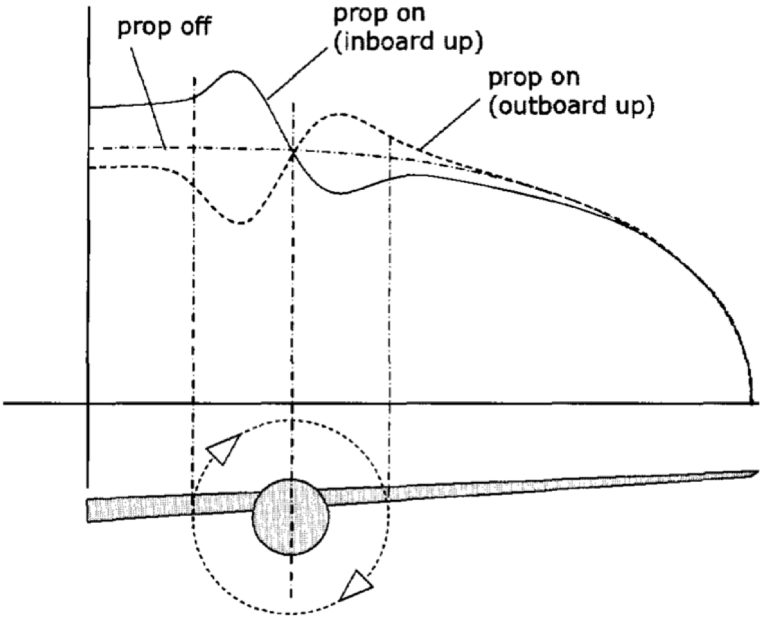

Figure 2.8: C_l distribution of one half of a wing including propeller influences [2]

An outboard-up propeller will generate a larger amount of drag, since the augmentation takes place at a lower loaded part and hence the negative effects of the downwash region start to dominate. Similarly, the spanwise location of the propeller is a factor which influences the drag reduction. The variation of lift is greater near the wing tip which implies that the influence of the variation will be stronger if the propeller is located there. For a tip mounted inboard-up propeller, the downwash effect is even omitted since the downwash part of the slipstream goes past the wing [3].

2.3.4. Swirl Recovery Optimization

Wind tunnel experiments of a rectangular wing including a propeller upstream showed a maximum possible drag reduction of 46% at $C_L = 0.1$ and $J = 1.15$ for an 8.25 aspect ratio (AR) wing as compared to the wing alone case without propeller [3]. However, no information regarding the thrust is given and perhaps the trust at the mentioned J is in excess compared to the wing drag. The advance ratio of 1.15 was the lowest measured, so this could indicate a high thrust setting. To say something about the potential increase of the propulsive efficiency, also information regarding change of the C_P is needed. More information regarding the change of the propeller performance is given in Section 2.4. It must also be noted that in the experiment [3], half-span mounted wing models were used where the propeller model was placed near the tip of the wing. The propeller was rotating inboard up and hence the negative influence of the downwash in the slipstream only acted on a very small portion of the wing. This might also account for the high decrease of drag coefficient.

To maximize the propeller swirl recovery by the main wing, an optimization of the wing could be done to maximize the increase in propulsive efficiency. For an optimized wing in a low-speed situation, the total drag reduction could be around 35.6% and for the cruise condition around 13.8% compared to the non-optimized wing [2]. A different numerical research showed a similar total wing drag reduction of 34.6% [6] for an optimized wing. Unfortunately, the results from these wing optimization tools are characterized by highly varying twist and chord distributions [2]. Such wings are not manufacturable and hence are not realistic for real flight usage. One study [18], included more constraints for the wing planform, in the optimization process. A wing with $AR = 12$, is optimized for maximal drag reduction, while keeping the AR, taper ratio and linear washout constant. Finally, constraints on the root and tip chord were applied and the result was a decrease of 9.15% of the induced drag. Still, the maximum variation in the chord is around 37% [18]. When the bounds on the root and tip twist are removed, the drag reduction increases to around 38.5%, similar to the previously discussed results. However, then the shape of the wing is unrealistic again. To conclude, very high drag reduction can be attained by optimizing the wing planform. However, when the shape of the wing needs to be kept within certain limits, the drag reductions quickly drop.

2.4. Aerodynamic Effects of Trailing Surfaces on the Propeller

Another effect that should be investigated is the effect on propeller performance due to the presence of the wing or another lifting surface behind it. The lifting surface creates an upwash in front and also gives rise to blockage of the flow, hence the experienced inflow field of the propeller changes [2]. The upwash creates a yawing moment, the bound circulation of the wing creates a pitching moment and the blockage results in increased axial velocity near the nacelle [3]. The upwash is strongest closest to the wing, since the distance to the bound vortex is the smallest here. The same can be said for the effects of blockage. This means that the closer the wing is to the propeller, the stronger the effects.

The creation of the yawing moment is visualized in Figure 2.9. It is created by the fact the down-going propeller blade moves against the upwash and sees an increased tangential velocity. This is depicted in the lower right sketch and the increased tangential velocity results in an increased α. The consequence of the larger α is an increase of thrust on the down-going side of the propeller. For the up-going blade side, the opposite happens, meaning the blades move with the upwash. This is depicted in the upper right sketch. The tangential velocity is reduced and with that the angle of attack and hence the resulting thrust. This will create an extra normal force together with a yawing moment in the direction of the up-going side [2].

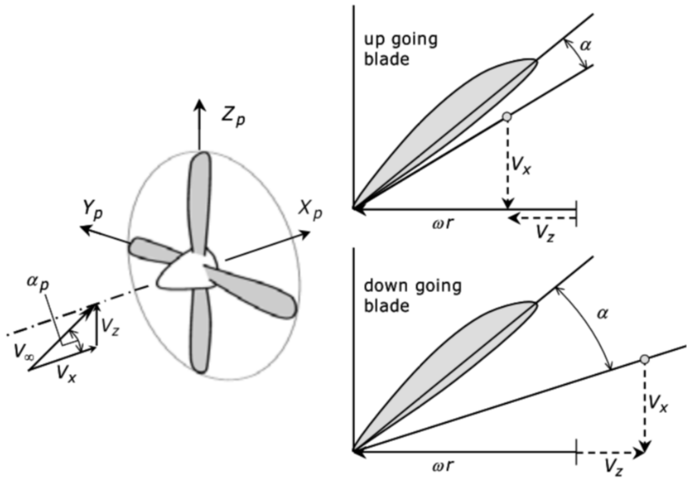

Figure 2.9: Upwash effects of the wing on an upstream propeller [2]

A pitching moment is created due to the bound circulation of the lifting surface [3]. The bound circulation will create an increased axial velocity at the top of the propeller disk and a decreased axial velocity at the bottom of the propeller disk. The increased axial velocity at the upper part of the propeller will increase the thrust, while the opposite happens at the lower part of the propeller. This creates a pitching down moment. The yawing and the pitching moment also need to be trimmed out, again resulting in more drag of the trim surfaces. The unsteady loading of the blades also means that the slipstream flow is no longer axisymmetric [2]. The unsteady loading also can result in additional noise produced by the propeller [19].

The changed inflow field of the propeller changes its aerodynamic performance. The thrust and power of the propeller are likely to change and hence the propulsive efficiency is influenced by the upwash effect of the wing. When the swirl recovery of the wing is included, it could be that the resulting increase in power required is larger than the decrease in trust required, hence the gain in propulsive efficiency can actually be negative. Not only the interference effects between the wing and propeller should be examined, but also other effects that contribute to the total drag of the whole aircraft and hence the propulsive efficiency, such as the increase in trim drag, should be investigated. Optimizing the wing for swirl recovery results often in unfeasible designs [2]. Also for existing aircraft, modifying the whole wing is a costly and difficult task.

Now the principles of propeller-wing interaction are discussed, more information regarding the modeling of these processes can be presented. In Chapter 3, the modeling of both the propeller slipstream and the propeller-wing interaction are discussed, after which the current shortcomings of these models are highlighted.

3

Modeling of the Propeller-Wing Interference Effects

The fundamentals of the propeller slipstream and the interference between the propeller and the wing are described in the previous chapter. Since the effect of the slipstream on the wing lift and drag distribution can be large, there is a need for models that can accurately describe this interference. High-fidelity CFD analyses are computationally expensive and therefore not convenient in modern optimization frameworks. These frameworks need fast and reliable aerodynamic results and hence tools of lower fidelity are needed. For the modeling of the propeller slipstream and corresponding induced velocities, different approaches exist ranging from 1D to 3D analysis. These approaches are discussed in Section 3.1. The modeling of 3D aerodynamics is often done using potential flow tools. The modeling of the propeller-wing interaction can be done by adjusting these models to include the propeller induced velocities. This is explained in Section 3.2, including the shortcomings of the current models. Different authors discussed the discrepancies between the potential flow tools and experimental results and defined correction models to account for these differences. This approach is presented in Section 3.3. Finally, some initial CFD results performed previously are presented in Section 3.4.

3.1. Modeling Techniques of Propeller Slipstream

The modeling of the propeller is essential to obtain the correct velocity components throughout the slipstream. The simplest approach to model propellers is by only taking the axial momentum into account and modeling the propeller as a uniform disk where the pressure changes instantaneously. This actuator disk theory is explained in Section 3.1.1. To take the aerodynamics of the blades into account, 2D airfoil theory can be introduced and this results in a varying radial distribution of the induced velocity, including the swirl component. This blade element method is explained in Section 3.1.2. Finally, including the vortices allows for the modeling of 3D effects, such as the downwash due to the finite blade span. These vortex techniques are discussed in Section 3.1.3.

3.1.1. Actuator Disk Theory

The easiest representation of a propeller can be done using the momentum theory or so-called Actuator Disk (AD) theory. This general theory is basically a 1D analysis of the propeller in which the jet velocity and slipstream contraction can be calculated. A visualization of the AD theory is presented in Figure 3.1. The AD method assumes an infinitely thin propeller disk containing an infinite number of thin blades. The flow is characterized as incompressible, inviscid and irrotational. There is only a variation of momentum in the direction normal to the disk (x-direction), see Figure 3.1a [20]. The actuator disk is characterized by an instantaneous increase in static pressure of the flow, while the velocity increases continuously [21]. The distributions of those two flow parameters are shown in Figure 3.1b.

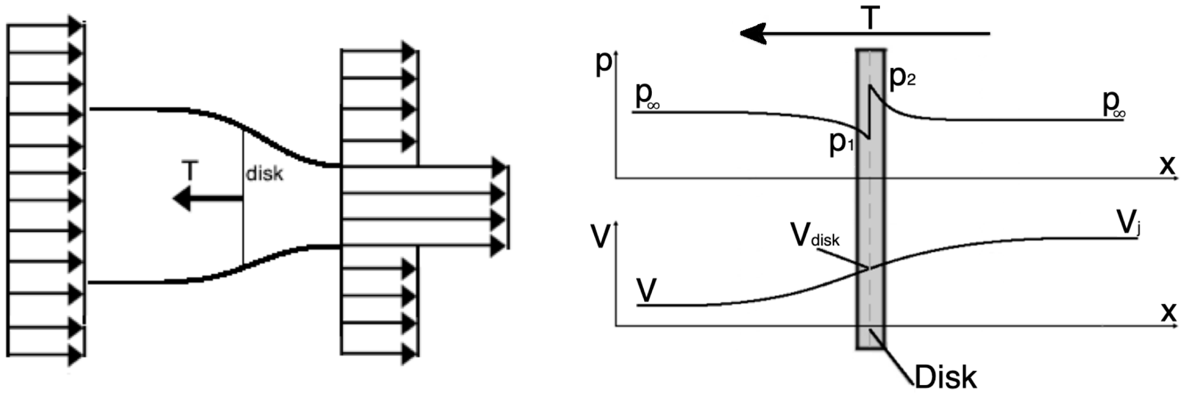

(a) Overall flow field (adapted from [20])

(b) Pressure and velocity distribution (adapted from [20])

Figure 3.1: Schematic visualization of the actuator disk theory

The thrust of the propeller is generated by the pressure difference across the disk, see Equation 3.1. Here A_{disk} is the frontal area of the disk, p_1 the pressure in front of the disk and p_2 the pressure behind the disk. Using Bernoulli's equation on either side of the disk, the velocity at the disk (V_{disk}) turns out to be the mean of V_j and V_∞, as can be seen in Equation 3.2. The velocity is assumed to be uniform over the entire cross-section of the slipstream and the distribution does not exhibit jumps [20]. By inverting the given equations, the jet velocity as a function of T and V_∞ can be calculated. This expression is given by Equation 3.3. ρ_∞ is the freestream density, which is assumed to be constant everywhere.

$$T = A_{disk}(p_2 - p_1) \qquad (3.1) \qquad\qquad V_{disk} = \frac{V_\infty + V_j}{2} \qquad (3.2) \qquad\qquad V_j = \sqrt{\frac{2T}{A_{disk}\rho_\infty} + V_\infty} \qquad (3.3)$$

Unfortunately, this simple method has its limitations. It does not account for any swirl in the flow, since it only assumes momentum variation in the x-direction. This means that losses due to the swirling motion are not included and hence the performance is over-predicted. Also, aerodynamic characteristics of the blades such as the resulting lift (L) and drag (D) are neglected. Furthermore, no blade planform parameters are incorporated, such as the camber, thickness, chord length and the number of blades [22]. In the next subsection, another propeller modeling method is discussed, which includes all these shortcomings.

3.1.2. Blade Element Method

To deal with the aforementioned shortcomings of the AD theory, a more advanced method can be used, such as the Blade Element Momentum (BEM) theory. A visualization of the BEM theory can be seen in Figure 3.2. The planform characteristics and aerodynamic characteristics of the blades are incorporated by discretizing the propeller blades into a number of sections and calculating the 2D aerodynamic forces on these sections, assuming 2D thin airfoil theory. The produced forces per section are used to calculate the resulting thrust and torque of the blade section. These forces are then compared to the values coming from the axial and circumferential momentum equation, which should be equal to each other.

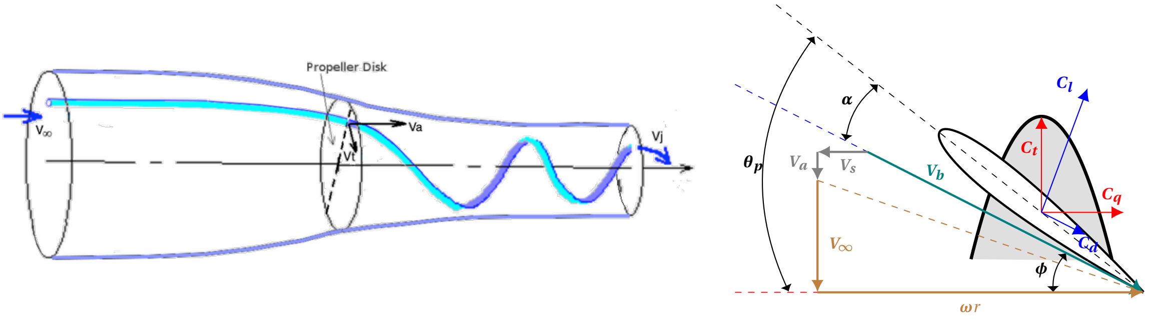

(a) Schematic representation of the overall flow field including swirl [23]

(b) 2D blade segment airfoil analysis [23]

Figure 3.2: Visualization of the blade element momentum method

However, due to the initial guess for the axial and angular inflow factors (a_p and b_p respectively), there will be a difference for both the thrust and torque. By iteration of the inflow factors, the correct blade velocity and angle of attack (α) for each blade section can be calculated and hence the axial and tangential (swirl) flow components of each section can be estimated. A schematic representation of the slipstream including the swirl component can be seen in Figure 3.2a.

The sectional lift can be calculated by numerical airfoil analysis with any two-dimensional method. In this way, also viscous effects can be accounted for [24]. The drag coefficient (C_d) of the blade section could be calculated by using an empirical relation using the zero-lift drag coefficient and a quadratic dependence on the lift coefficient (C_l). This empirical relation could be used since 2D potential flow cannot account for viscous drag or lift-induced drag. However, these potential flow approaches are not very accurate and a more sophisticated approach would be by using a viscous boundary layer model, such as is done in XFOIL. In this way, the lift and drag coefficients can be determined for each section including phenomena as separation and stall of the blade [25]. This will result in a more realistic propeller performance. This 2D sectional approach is presented in Figure 3.2b and by using the specific pitch angle of the segment, the sectional thrust and torque can be calculated.

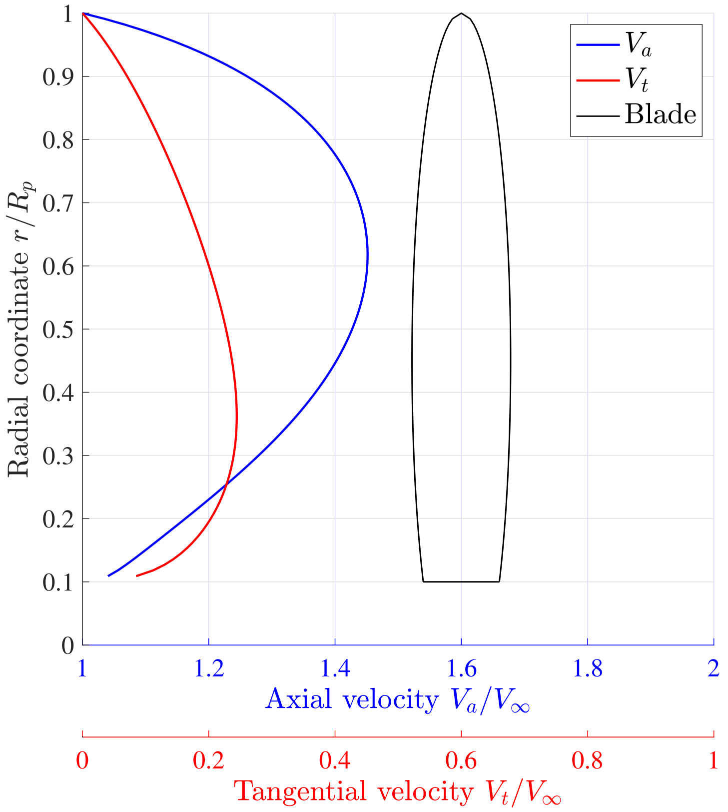

Figure 3.3: Results from the BEM analysis of an arbitrary propeller

The flow field behind the propeller can now be analyzed in terms of the axial and tangential velocity. The BEM theory was coded into Matlab and the results for an elliptical blade are shown in Figure 3.3. The outline of the blade is also plotted and the propeller was modeled with two blades. V_a and V_t are taken to be the values far from the blades, like V_j in the AD theory. As shown in Figure 3.3, the axial velocity is maximum at around 60% of the radius. This analysis is done using an elliptic blade. The blade is loaded most at the tip region, but since the chord is smaller there, the axial flow peaks at a lower radial location. The tangential velocity is highest close to the root and gets smaller towards the tip. The BEM theory can be used in first-order estimate design tools to optimize the propeller planform characteristics. To create even more realistic results or to model the development of the slipstream, 3D vortex theories or CFD simulations should be used. In the next section, the 3D vortex technique will be shortly discussed.

3.1.3. Potential Flow Techniques Including Vorticity

To capture the 3D phenomena around the blade and to model the wake of the propeller accurately, more advanced potential flow techniques can be used. There are different methods and the main difference between these is the way the wake is modeled. This can be free or a fixed wake, of which the latter is less accurate but computationally cheaper [26]. One example is the lifting-line theory for propellers. The general lifting-line for a wing will be explained in greater detail in Chapter 7, but the principle is similar for the propeller. The propeller blade is modeled using a bound vortex line. The variation in bound vorticity results in a shed vortex sheet behind the propeller. The vortex sheet will be helicoidal in shape and continue downstream as a cylindrical wake. The vortex sheet will propagate as rigid screw surfaces backwards, having a constant pitch and radius for each vortex portion, by assuming the fixed wake analysis. This is shown in Figure 3.4a for a propeller containing three blades. In this way, the induced velocity of the vortex sheet on the lifting-line can be calculated and hence the performance of the propeller [27].

Codes for the free wake model are more similar to panel codes, including also panels to describe the wake. This is an iterative procedure, since the initial wake shape is estimated. The trailing vortex filaments must be aligned with the local velocity, otherwise there will be a pressure difference across the sheet and hence a resultant force. The first iteration results in a vorticity distribution over the propeller blade, resulting in a different wake shape and this is therefore iterated until the full wake is prescribed and being force free [28]. These methods are often expensive in terms of computational cost, but are more simple and faster than CFD. In this research, only the time average effects are of interest and therefore to model the propeller slipstream, an infinite number of blades can be assumed such that the whole slipstream is radially symmetric [2].

It can be assumed that, due to the bound vortex interaction on the trailing vortex sheet, the wake will roll up behind the blades and the vorticity will be concentrated in the edge of the slipstream. This results in a so-called tube model, in which the outer edge is a continuous distribution of helically shaped vortex lines [2]. The helical vortex lines can be further split into two perpendicular sets of lines. The circumferential lines, only contributing to the axial velocity increase, are placed normal to the propeller disk. The axial lines, parallel to the propeller axis, contribute to the swirl component [2]. This propeller tube model is shown in Figure 3.4b. By modeling the slipstream, the induced velocities and therefore effect on the flow field can be modeled.

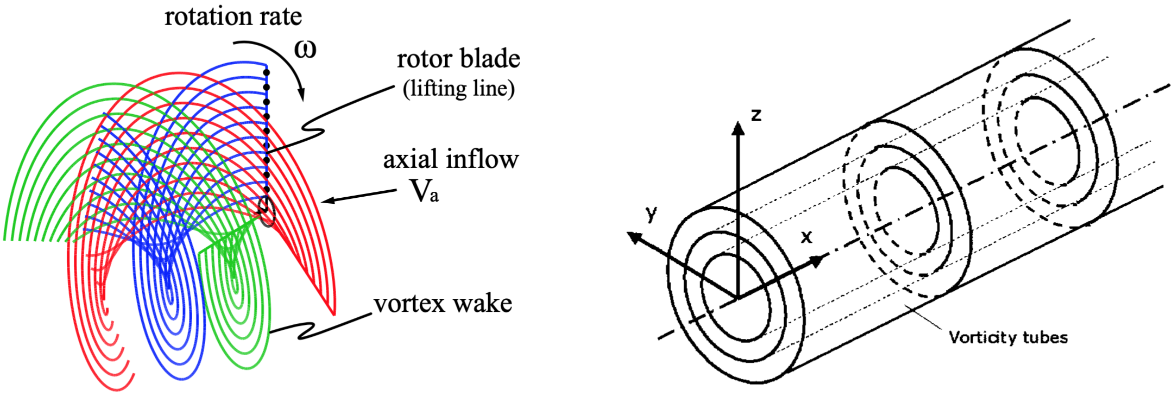

(a) Lifting-line representation for propeller [28]

(b) Propeller tube model [2]

Figure 3.4: 3D propeller modeling techniques

A similar approach can be done in 2D, assuming the jet velocity is constant throughout the jet. The axial propeller slipstream can be modeled using vortex lines on the boundary of the jet. This is equivalent to taking a slide of the tube model, where the vorticity is concentrated along two parallel sheets. This is shown schematically in Figure 3.5. The two vortex sheets are placed at the boundaries of the jet and are used to model the velocity increase. If the vortex sheets extend to infinitely far away, the increase will be an instantaneous jump in axial velocity across the vortex sheets. This means that the slipstream of the propeller is modeled to be fully developed and no vertical velocity component exists in the jet or in the freestream. A small portion of the flow field including the velocity vectors and the vortex sheets are shown in Figure 3.5a. This domain is far away from the ends of the vortex lines and therefore, there is no vertical velocity component. In Figure 3.5b, the axial velocity distribution is plotted for the same domain.

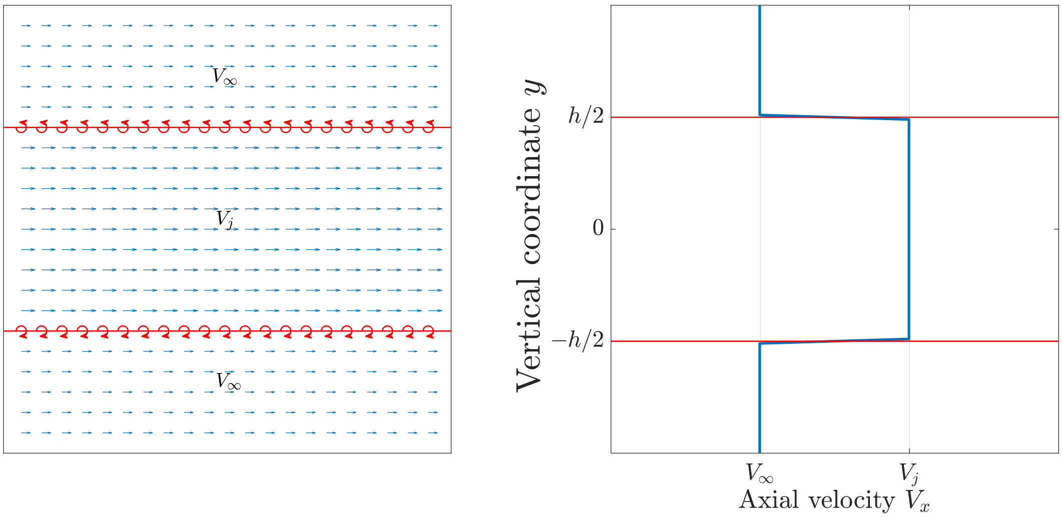

(a) Velocity field using vortex panels

(b) Velocity distribution in vertical direction

Figure 3.5: Modeling of the propeller slipstream using vortex panels

The AD and BEM methods were used in this thesis to further investigate the influence of the propeller slipstream induced velocities on the main wing in a tractor configuration. The 2D vortex method of describing the jet using two streamlines with concentrated circulation will be the basis for the correction method to account for finite height in 2D and the effect on the sectional lift. This is explained in Chapter 4. The influence of the propeller slipstream on the trailing wing and the modeling of this process will be discussed in the next section.

3.2. Modeling of Propeller-Wing Interaction

To model the aerodynamic interference as discussed in Chapter 2, different approaches can be taken. For an initial estimate of a tractor propeller slipstream effects on the main wing, low-fidelity potential flow analysis tools can be used. To get more reliable results, CFD simulations or wind tunnel experiments should be performed. Unfortunately, these high-fidelity methods have considerable setup and execution time. The most simple method to analyze the propeller-wing interaction is the use of an analytic formula, which can be used to find an optimal lift distribution while minimizing the induced drag, given the propeller induced velocities [29]. However, this analytic method can only be used for getting the optimal lift distribution and hence the wing planform should be derived from this. To analyze a certain wing design, a strip method should be chosen, in which the wing is divided into small control sections. These tools make use of potential flow theory and are discusses shortly in the coming sections. Firstly, in Section 3.2.1, theory of the potential flow are explained including the used assumptions and boundary conditions. These models have multiple advantages but have problems when it comes to combining the propeller slipstream with the freestream as is done in current models. This shortcoming is discussed in Section 3.2.3 and is the possible cause of the large discrepancies between the analysis results and the validation data.

3.2.1. Potential Flow Theory

Potential flow is a simplification of the aerodynamics using two main assumptions. Firstly, the flow is irrotational, meaning there is no curl of the velocity field or in other words, there is no vorticity in the flow. In the potential flow theory, the velocity field is described as the gradient of a scalar function. This scalar function is called the velocity potential (ϕ) and only exist if the flow is irrotational. Secondly, the flow is inviscid, meaning that the flow has no viscosity and hence friction does not exist. Potential flow does not necessarily have to deal with incompressible flows, but assuming that the density stays constant is a large advantage and makes the equations much simpler [30]. Potential flow is very often used in aerodynamic analysis, especially for first-order estimations of lift characteristics. For an incompressible potential flow field, the potential function satisfies the Laplace's equation. This linear PDE has the benefit that simple potential flow elements can be added following the principle of superposition [11].

No vorticity does not mean that there cannot be any circulation. Circulation can be seen as the macroscopic measure of rotation and is calculated as the line integral of the velocity along a simply closed curve, see Equation 3.7 [11]. Since a point (free) vortex is a singularity, the contour taken to calculate the circulation must be around this point and no singularity can lay on the contour, since the velocity is not defined in this point. Also, the vorticity at the exact location of the vortex is infinitely large, but anywhere else it is zero so the velocity field is still irrotational. For the circulation around a free vortex, the value is independent of the size and shape of the line. Therefore, the strength of a free vortex is denoted by the circulation (Γ) it produces [11].

The Laplace equation can be used for all kinds of flow problems and hence the difference is determined by the boundary conditions, that must be satisfied by the flow. When a body, such as an airfoil, is placed in a uniform stream (V_∞), the streamlines will be deflected close to the object. The main boundary conditions for potential flow are the following: at $x = \pm\infty$ and $y = \pm\infty$, the disturbances of any object are zero. The velocity in x-direction is denoted by u, as where the vertical velocity is presented by v. This is mathematically expressed in Equation 3.4 & 3.5. The streamlines of a 2D flow can be given by using the scalar stream function (ψ). The stream function is a useful addition and a result of the Laplace equation property that an orthogonal function also satisfies the equation. This means that the lines of constant potential and constant stream function always intersect each other perpendicularly. A rigid body deflects the streamlines, since the flow can not penetrate the surface. This means that the velocity normal to any surface (V_n) must be zero and that the body surface turns into a streamline of the flow [30]. This is expressed in Equation 3.6.

$$u = \frac{\partial \phi}{\partial x} = \frac{\partial \psi}{\partial y} = V_\infty \qquad (3.4) \qquad v = \frac{\partial \phi}{\partial y} = -\frac{\partial \psi}{\partial x} = 0 \qquad (3.5) \qquad V_n = \frac{\partial \phi}{\partial n} = \frac{\partial \psi}{\partial s} = 0 \qquad (3.6)$$

To model 2D airfoils or other shapes using potential flow theory, multiple elementary flows can be used to represent the influence of the airfoil on a uniform flow. One example and easiest way is to model the camber line as a vortex sheet. By setting the boundary condition on the camber line to have no velocity across the sheet, the camber line turns into a streamline. This is also known as the thin airfoil theory and gives estimates of the lift and moment coefficient of thin airfoils using only a sheet representation. It turns out that the slope of the lift coefficient versus angle of attack curve is equal to 2π for all airfoils [11]. However, by using the thin airfoil theory, the thickness of the airfoil is not included in the analysis and no accurate pressure distribution over the airfoil can be calculated. To analyze airfoils or other bodies of arbitrary shape and thickness, the use of numerical methods, which represent the airfoil using panels, is needed. A large benefit of panel methods is the fact that now the pressure distribution can be calculated without the need to calculate the whole flow field. Potential flow methods can also be expanded to 3D to be able to model wings.

Looking at the Laplace equation for the flow around a 2D airfoil, there exists an infinite amount of solutions satisfying the zero normal velocity boundary conditions and hence the undisturbed freestream velocity and the geometry of the body (airfoil) do not determine the strength of the circulation. The total circulation around the airfoil is related to the so-called Kutta condition. The Kutta condition states that at the sharp trailing edge, the flow cannot go around the corner, since this would result in an infinitely high velocity. Therefore, the stagnation point must be fixed at the trailing edge and this results in the fixed value for the circulation [11]. The Kutta condition and the accompanying circulation results in a velocity difference above and below the airfoil, generating lift. Without circulation, there is no lift generated, while in reality viscosity is needed to create lift. So the Kutta condition can be seen as an inviscid representation of the viscous effects that are responsible for the lift generation, without the need for boundary layer equations.

For 2D potential flow analysis of a uniform flow problem, it is found that the circulation generated by the airfoil, is directly proportional to the generated lift [11]. The Kutta-Joukowski (KJ) theorem states that the sectional lift of on object (l) is equal to the created circulation (Γ) multiplied by the freestream density and velocity , see Equation 3.8. So the lift is related to the velocity far upstream (V_∞) and the induced velocities at the surface are not directly taken into account in this theorem. When using a panel method, the distributed circulation of all panels can be added to find the total circulation and the lift can be calculated accordingly.

$$\Gamma = \oint_c V \cdot ds \qquad (3.7) \qquad\qquad l = \rho_\infty V_\infty \Gamma \qquad (3.8)$$

This lift value will be equal to the value found if the pressure distribution of the panels, determined by calculating all the induced velocities created by the same distributed vortices, is integrated in the chord wise direction. The potential flow approach is also often used in first-order estimation of 3D aerodynamic problems, such as flow over a wing. In Section 3.2.2, a small introduction into 3D modeling using potential flow is given, after which in Section 3.2.3, the shortcomings regarding these tools when the effects of the propeller slipstream are added, are explained.

3.2.2. Propeller-Wing Analysis Tools

The most simple wing analysis can be done using the lifting-line method. For the lifting-line, the wing is discretized in a finite number of sections. By making the sections as small as possible, the continuous circulation distribution is approached. The trailing vortices of the 2D sections create a vortex wake in the form of a vortex sheet, creating downwash over the wing. The shed vortex of each section creates induced velocities on the other sections. The induced velocities change the effective angle of attack at each section and the lift coefficient calculated using the 2D thin airfoil theory should produce the circulation that created the shed vortex sheet in the first place. The mathematics regarding the LL method are presented in Chapter 7. The local circulation is calculated using the KJ theorem and the 2D aerodynamics are based on the thin airfoil theory, where the slope of the lift curve is constant.

To analyze more general wing shapes, the lifting-line method can be extended to include the spanwise variations, such as the change in chord towards the tip, better known as taper. By doing this, also wings including sweep and dihedral can be analyzed. This is known as the vortex lattice method (VLM), where the whole wing is discretized in panels. On each panel, horseshoe vortex is placed at the 1/4 of the panel length and a control point is placed at 3/4 of the panel length. All the horseshoe vortices are generating up- and downwash on the other panels. At the control points, the component of these induced velocities normal to a panel should be equal and opposite in direction as the normal component of the incoming velocity, so the boundary condition of zero normal flow is fulfilled. In this manner, the strength of the total vortex system can be calculated and hence the distribution of bound circulation. The 3D panel method is similar, but takes into account the thickness distribution of the wing.

To conclude, both methods are based on the fact that each strip or panel must produce a certain amount of downwash to fulfill the boundary conditions. The vortex strength of each 2D section is dependent on the local incoming velocity (V_l). So for both the LL method and the VLM, the propeller induced velocities can be added to the freestream velocity to come up with this local velocity. This local velocity is then used to determine the circulation distribution. The circulation distribution from either the LL or the VLM is translated to the local lift using the KJ theorem. In this way, the effect of the propeller on the lift coefficient distribution can be analyzed as was done in multiple research projects in the past [2, 6–8].

As mentioned in Section 2.4, the wing will also influence the propeller performance. The axial and tangential velocity which are used for the wing analysis method can come from different propeller modeling methods, as discussed in Section 3.1. To accurately couple the slipstream and wing analysis model, an iterative procedure should be followed. The wing aerodynamics are calculated from an initial propeller analysis, after which the upwash and axial acceleration created by the wing can be used to alter the propeller data. This is repeated until the results converge [2, 6–8]. However, in this thesis, the focus is put on the effect of the slipstream on the wing lift distribution and hence only a one-way model is designed. This one-way model uses a propeller model to simulate an isolated propeller slipstream and add these induced velocities to the wing analysis tool.

3.2.3. Limitations of the Existing Potential Flow Tools

Unfortunately, in most studies found in literature, the results from the potential flow tools, as discussed above, do not match the results from wind tunnel experiments and influences are largely over-predicted. This was noted for larger propeller slipstream velocities compared to the freestream velocity and was extensively discussed in a previous study where both an LL and VLM method were used [6]. The general shortcoming of using the potential flow tools, such as the LL of the VLM, is the way the propeller slipstream velocities are included. These tools can be adapted to include the tangential and axial velocity components from the propeller as discussed above. It is often assumed that the propeller axis is in the same plane as the LL or the VLM sections and hence the induced axial velocity of the propeller can be completely added to the freestream velocity if a specific section is located inside the slipstream. Furthermore, it is assumed that the wing is in the middle of the slipstream and hence the wing is located at the horizontal symmetry plane of the propeller. By assuming this, the swirl velocity is always pointing in the vertical direction only. So the tangential velocity of the propeller can be added to the created downwash of the wing and hence the induced angle of attack is altered [6]. If the wing is not located in the horizontal symmetry plane, the tangential velocity will have a component in the spanwise direction. However, this spanwise velocity is parallel to the lifting line, meaning it does not influence the created circulation.

So the effective incoming velocity is only determined based on the location of the lifting-line strip or VLM chord wise row of panels. If a specific strip or panel row is located in the slipstream of the propeller, the total propeller induced velocities are added to the V_∞. If they are outside of the slipstream, nothing is added to the freestream flow. This strip process, for the LL method, is visualized in Figure 3.6. In this figure, only the axial component of the propeller slipstream is taken into account and it is assumed that the velocity in the slipstream has one uniform value of V_j. So if strip AA is analyzed, which is located outside of the slipstream, V_∞ is used to determine the specific α_{eff} for the LL method or V_n for the VLM. On the contrary, if strip BB is analyzed, V_j is used for these calculations.

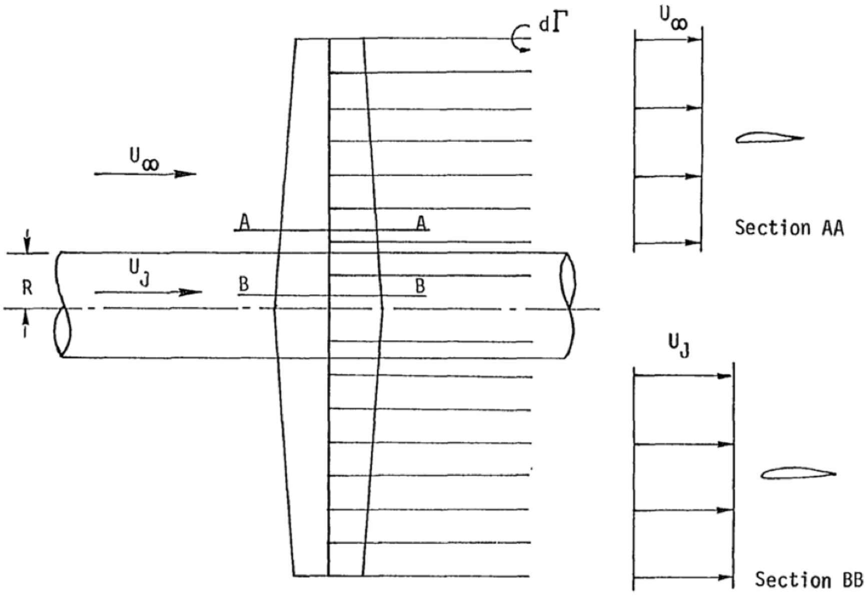

Figure 3.6: Schematic lifting-line representation including a circular jet in the middle [31]

Depending on the location of the vortex element, either V_∞ or V_j is used in to determine the sectional lift. By using this approach, it is assumed that the propeller is located infinitely far away and that the flow field vertically runs from -∞ to +∞. The actual slipstream height is therefore not taken into account and a section close to the edge of the slipstream is treated equally as a section in the middle of the jet. However, for a circular jet, the height varies along the span and the local lift should, therefore, depend on the slipstream height. A correction for this slipstream height should be included for each 2D section.

3.3. Empirical Correction Factors

The influence of the propeller slipstream on the wing lift distribution calculated by the previously designed potential flow tools has been largely over-predicted compared to experimental data. This has been attributed to two main factors, of which one is the swirl recovery of the wing. The swirl recovery of the main wing causes the vertical velocity to decrease and therefore the wing does not experience the full tangential velocity component of the propeller [2, 6, 7, 9]. In other words, the reduction in swirl by the main wing means that the effect of the tangential velocity component should be diminished. A so-called swirl recovery factor (SRF) was used, which was necessary to achieve good agreement with experimental results. Veldhuis estimated this factor to be approximately 0.5, based on wind tunnel data [2]. Alba expended this approach and tried to define a method so this SRF could be found for every wing and slipstream shape [7]. The reduction in tangential momentum across the wing was used to define this SRF. Unfortunately, the SRF is not really based on any physical flow phenomena and determination of it for arbitrary situations is difficult [6]. This indicates that not all the flow phenomena are modeled by the VLM and more investigation into the modeling of propeller-wing interaction should be performed.

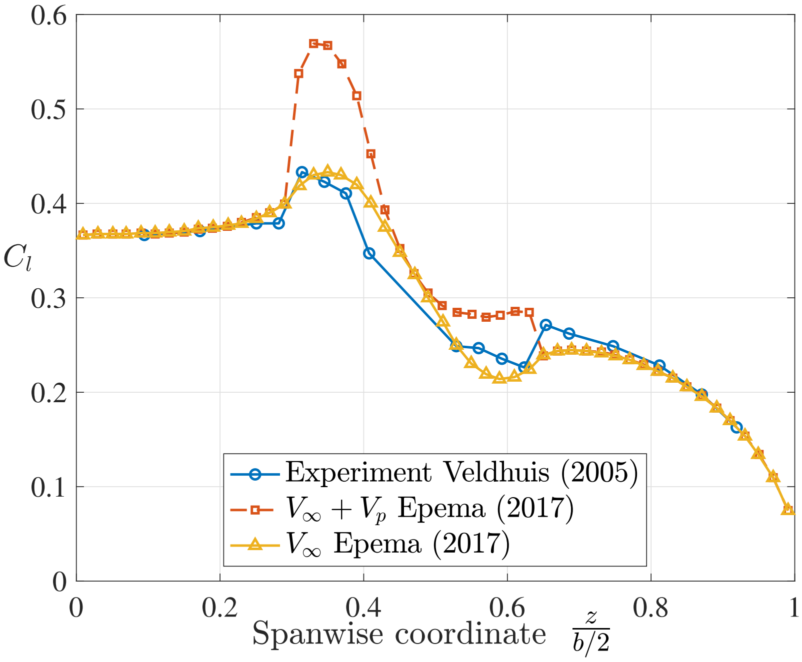

Figure 3.7: Visualization of the over-prediction of local lift coefficient using the VLM potential flow tool compared to wind tunnel results [2, 6]

The second correction factor was defined for the axial velocity inflow of the wing. Alba and Epema noticed that the analysis results of the different flow analysis tools were still over-estimating the slipstream effects, even after application of the SRF [6, 7]. Both deemed the use of the axial propeller velocity in the KJ theorem to calculate the local lift 'unphysical', since their analysis results were not matching experimental data. On the contrary, the initial calculation of the circulation, either from the LL method or VLM is a function of the local velocity and hence including the addition of the propeller axial velocity (V_a), see Equation 3.9. Removing the propeller influence of the calculation of the circulation would yield an unaltered lift distribution after all.

$$\Gamma_l = f\left(V_l\right) \qquad (3.9) \qquad\qquad l \neq \rho_\infty V_l \Gamma_l \qquad (3.10)$$

Although the local velocity is needed for the circulation, it is not used to calculate the local lift, see Equation 3.10. By also using the local velocity, it is thought that the increased dynamic pressure is included twice and therefore, V_∞ is used in the KJ theorem. This is physically not correct, but it seemed the only explanation which could certify the large discrepancies. An example of the change in local C_l by changing the KJ-theorem is shown in Figure 3.7. The blue line represents the data from the wind tunnel experiment [2], while the red and yellow line are from the potential flow analysis tool [6]. The difference between the red and yellow line is in the definition of the KJ-theorem. The former uses the total local velocity to calculate the local lift, while the latter only takes the axial freestream conditions into account. Both lines include the swirl component of the propeller as a vertical velocity component, which is corrected by the SRF.

By using V_∞ for the calculation of the C_l, the results seemed to be close to the wind tunnel data. However, locally the wing experiences this increased dynamic pressure and hence this should be included in the KJ-theorem. More discussion about the right use of velocity in the definition of the local lift is presented in Section 7.3. If for example, a wing would be fully submerged in a rectangular jet, which has a very small height along the complete span, the circulation that would be calculated using V_l would be highly over-estimated. All of the potential flow methods mentioned so far simply add the propeller induced velocities to the freestream, assuming the flow in each 2D airfoil analysis is extending from and towards infinity. So the spanwise dimensions of the propeller are taken into account, but the height of the slipstream is not. This neglect of the propeller slipstream height can be possibly the reason for the over-prediction of the propeller effects on the wing. Therefore, the aim of this thesis is to find a potential flow approach which can be used to correct for the finite propeller slipstream dimensions.

3.4. Reference CFD Analysis of the Finite Slipstream Height

One of the research studies that looked into the effect of finite slipstream height on the airfoil lift augmentation was about NASA's distributed electric propulsion concept in their SCEPTOR project [32, 33]. This research investigated the aerodynamics of an aircraft using multiple small propellers upstream of the wing. Only the tip propellers are used during cruise and for take-off and landing, where more lift is required due to the lower airspeed, all propellers along the wing are used. The conceptual model can be seen in Figure 3.8. It turned out that the height of the slipstream does influence the local lift perceived by a 2D airfoil section, confirming the need of a correction method.

Figure 3.8: NASA Leading Edge Asynchronous Propellers Technology (LEAPTech) distributed electric propulsion concept (X-57 Maxwell) [32]

The small propellers have diameters of around the order of the chord. In the SECPTOR research project, the effect of the finite slipstream height was expressed through a correction factor for the jet velocity, since the finite slipstream changes the predicted lift. It was therefore assumed that the 2D lift coefficient was unaltered and instead an effective velocity was calculated. By applying this correction, the 2D airfoil analysis can be done using an infinitely high but slower jet [33]. This correction factor (β) was only applied to the axial induced velocity of the propeller (V_p). The corrected jet velocity can be expressed using Equation 3.11. The produced sectional lift of the airfoil submerged in the jet is presented by l_j, while the sectional lift of that same airfoil without the jet is presented by l_∞. The ratio of the two sectional lift values is defined by K_l, see Equation 3.12. This lift ratio will be different depending on the slipstream height to chord ratio and the velocity ratio.

The definition of β can be seen in Equation 3.13, meaning that β will range from 0 to 1. $\beta = 1$, when $h/c = \infty$, since for the infinitely large jet, the regular potential flow solution is valid and hence $K_l = V_j^2/V_\infty^2$. For infinitesimal slipstreams, $\beta = 0$ since the slipstream will not influence the local lift and hence $K_l = 1$. The lift ratio for different slipstream heights was determined by the use of CFD simulations in the program OVERFLOW and can be seen in Figure 3.9. The values are shown for $V_j = 2V_\infty$ and differ for different upstream propeller locations (u_p/c). The NACA 0012 airfoil was chosen for the analysis and it included the propeller, which was modeled using an actuator disk. A large rectangular domain of 200 chord lengths was chosen.

$$V_{j_{corr}} = V_\infty + \beta V_p \qquad (3.11) \qquad\qquad K_l = \frac{l_j}{l_\infty} \qquad (3.12) \qquad\qquad \beta = \frac{\sqrt{K_l} - 1}{V_j/V_\infty - 1} \qquad (3.13)$$

It was concluded that if the h/c value was less than 3, the lift augmentation due to the increased dynamic pressure would be reduced significantly compared to the simple case using an infinite slipstream height. For the research mentioned, the effect of the finite slipstream height caused an increase in the propeller power required to produce the specifically desired high lift configuration. This is because the lift augmentation is over-predicted and hence the necessary lift is reached at higher values of V_j, which corresponds to a higher power setting of the propeller [32]. The results from the OVERFLOW analysis were used to generate a surrogate model for the velocity correction factor. This was done so this correction factor could be used in design processes that needed fast evaluations, such as optimization routines.

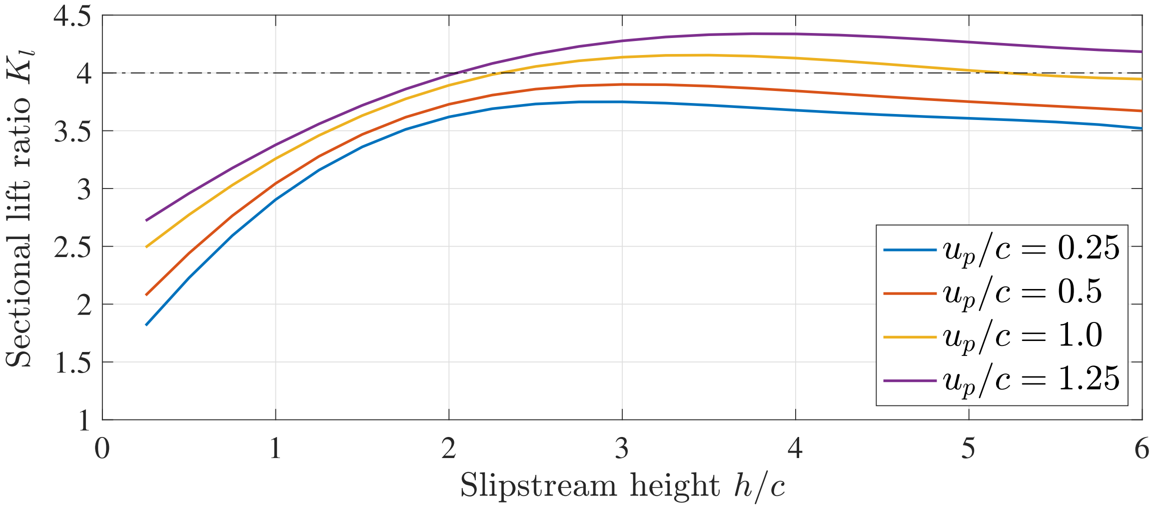

Figure 3.9: Sectional lift ratio (K_l) for the NACA 0012 airfoil and $V_j = 2V_\infty$ as function of slipstream height and upstream distance of the propeller [33]

The simulations were performed using an AD and hence the slipstream contracts further away from the disk. The results showed that the maximum values of the lift ratio were actually higher than $(V_j/V_\infty)^2$, which is not possible for the potential flow analysis. This is due to the fact that for the OVERFLOW simulations, the energy equation was added, meaning the density and temperature were not held constant. The variation of these two flow properties was caused by the increase in pressure across the disk [32]. After $h/c = 4$, depending on the upstream location, the values of the lift ratio decrease slightly, which is caused by the fact that for larger propellers, the jet must contract over a large absolute distance and hence the final jet velocity is reached further downstream [33].

Increasing the streamwise location of the propeller by placing the airfoil further downstream, increased the value of K_l, due to the contraction of the slipstream. The values of K_l can unfortunately not directly be used as generalization in a potential flow method. The CFD simulation used more variables, such as the change of air properties, resulting in theoretical impossible lift ratios compared to simple potential flow analysis. In the case of $V_j = 2V_\infty$, values for K_l above 4 were obtained, while 4 is the upper limit using potential flow theory. The question remains if a surrogate model of high-order method is better or worse than a low-fidelity tool, in which each data point can be calculated very quickly. However, this thesis tries to find a physics-based model, such that the correction method will work for arbitrary geometries and propeller conditions. This is not the case when using a surrogate model. In Chapter 4, a potential flow method to capture the finite slipstream height is discussed and the results of this method including CFD data are presented in Chapter 6.

Part II
2D Analysis

The second part of this thesis will be focused on the 2D analysis of an airfoil, submerged in a jet. This models the case of a wing segment influenced by a propeller slipstream, where only the axial component is taken into account. Firstly, the setup and theory of the used approaches will be presented. The finite height of the jet will influence the lift augmentation and a potential flow method is discussed which includes this effect. The physical background and the equations are discussed in Chapter 4. Secondly, to validate this correction model, CFD simulations were performed, simulating the potential flow analyses. The setup of the CFD simulations is discussed in Chapter 5. Finally, the results of both the potential flow tool and the CFD simulations are discussed and compared in Chapter 6.

4

Modeling the Effects of the Finite Slipstream Height

The potential flow tools mentioned in the previous chapter are used to analyze propeller-wing interaction in an initial stage. Unfortunately, the results from the tools are not close to the data of CFD analyses and wind tunnel experiment results. A possible cause for the error is the effect of the finite extent of the propeller slipstream on the 2D airfoil analysis. In this chapter, a numerical potential flow method is discussed, which can model the effect of the finite slipstream height on the lift of a 2D airfoil. In Section 4.1, information regarding the finite slipstream height is given. In Section 4.2, the problems regarding the modeling of this finite slipstream height are discussed, after which the general approach is given in Section 4.3. The sensitivity analysis of the numerical method is presented in Section 4.4. The numerical method also has its limitations and these are discussed in Section 4.5. Finally, some remarks regarding the modeling of the swirl component are given in Section 4.6.

4.1. Finite Slipstream Height

As discussed in the previous chapter, the propeller-wing interaction can be modeled using any potential flow vortex method. For evaluating each slice of the wing, a 2D analysis of that particular airfoil section is done. In the currently existing tools, the inflow characteristics are taken as being uniform, as described in Figure 3.6. In other words, this specific section inflow is modeled to extend from and towards infinity, but in reality, this is not the case, due to the finite slipstream radius. To further simplify the analysis, it is assumed that the slipstream is modeled using the AD theory, meaning there is no variation of axial velocity in the radial direction. The flow field around each section will look more like the representation in Figure 4.1.

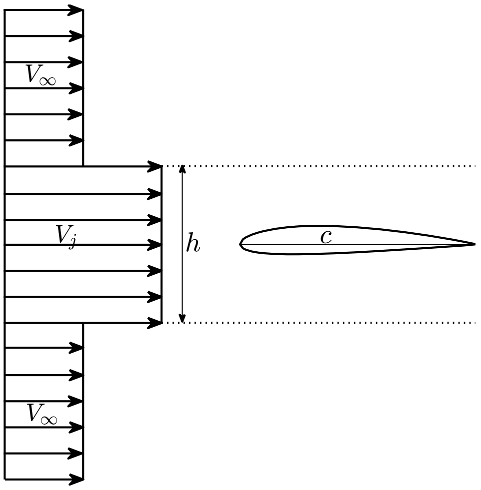

Figure 4.1: Schematic representation of finite slipstream height in the 2D airfoil analysis assuming a constant velocity jet

By neglecting the finite extent of the slipstream, the lift coefficient is over-predicted [10]. For an infinite slipstream height, the ratio of sectional lift compared to the no slipstream case will be $(V_j/V_\infty)^2$. So in the case of $V_j = 2V_\infty$, the sectional lift will be $2^2 = 4$ times as large as the original case. Very little research projects take the slipstream height into account since the effect is often assumed to be small. However, this is only true for propellers, which are large compared to the chord and where the wing is located in the middle of the slipstream [10, 34]. However, the effects start to become dominant in the region close to the propeller tips. Here the slipstream height to chord ratio (h/c) becomes small and the lift ratio for the airfoil becomes lower compared to the undisturbed infinite inflow case [10]. More and more research nowadays is into distributed propulsion aircraft and these feature multiple small propellers of which the diameter is in order of the chord or even smaller. So for these multi-propeller problems, including the effects of the finite slipstream height becomes important [32–34].

4.2. Modeling of Vorticity in the Flow

The problem encountered with an airfoil in a general propeller slipstream is that the flow is no longer irrotational. This is due to the shear created between the regions of different velocity. This means the flow can no longer be modeled exactly using a potential function. For a potential flow to exist, the flow must be irrotational [11]. However, the stream function does exist for rotational flows and hence can be used to define the flow field. In Equation 4.1, the governing equation is shown, which is a Poisson equation. The vorticity is defined by the curl of the velocity field. In the slipstream height analysis, only the V_a is included, as shown in Figure 4.1 and hence the total velocity field only has a variation of velocity in the vertical (y-)direction. After the use of these assumptions, the vorticity can be defined as the y-derivative of the velocity, see Equation 4.2.

$$\nabla^2\psi = -\omega\left(\psi\right) = -\nabla\times V \tag{4.1}$$

$$\omega = -dU(y)\big/dy \tag{4.2}$$

$$\frac{\partial\psi}{\partial s} = 0 \tag{4.3}$$

Equation 4.1 is a nonlinear differential equation due to the nonlinear vorticity term. Normally, the flow field around an airfoil can be calculated by the fact that the stream function is constant along a streamline and hence along the airfoil surface, see Equation 4.3. However, the constant value of the stream function at the surface is unknown a priori, so for every value of the constant, a solution can be obtained. The correct value of the constant can be obtained by enforcing the Kutta condition at the trailing edge [35]. Since the Poisson equation is a nonlinear Partial Differential Equation (PDE), the equation must be solved in a numerical way using a finite difference technique on grid points in a finite domain. The numerical approach was done in a previous study using an iterative schema at each grid point [35]. The results from this study demonstrated strong interaction between the vorticity in the non-uniform stream and the vorticity of the airfoil.

The method previously mentioned of discretizing the domain is more or less a basic form of a CFD implementation. The benefit of using such numerical method is that it can handle any airfoil shape and any given upstream velocity profile [35]. For a linear and exponential velocity profile, the non-linear Equation 4.1 even reduces to a linear equation. However, there are also quite some disadvantages of using such a numerical method. The meshing of the domain is always a difficult and time-consuming process. Furthermore, the smaller the grid size, the higher the computational cost of the program. Especially for low-fidelity optimization tools, the computational cost should be as low as possible without compromising the accuracy too much, so small changes can be calculated quickly.

Other problems are encountered while defining the boundaries of the domain and the associated boundary conditions. To remove all the velocity disturbances at the boundaries, the domain should be infinitely large, which is not possible. By reducing the domain size, the solution starts to deviate from the exact solution. The discretization errors and the relatively high computational cost are the main reasons to search for an analytical solution. If the propeller slipstream is replaced by a uniform jet, the nonlinear problem can be simplified and the flow can be modeled using potential flow. This is equivalent to modeling the slipstream using vortex sheets as shown in Figure 3.5. However, the main assumption for this is that the vortex sheets are streamlines of the flow and hence the boundary conditions along these sheets must be satisfied. An often used potential flow method to account for straight boundaries is by the use of image vortices [36]. This method of images will be used to model the finite slipstream effects on the lift augmentation.

4.3. Application and Modeling of Image Vortex Correction Techniques

A well-known technique for potential flow in the proximity of the discontinuities, such as walls, is modeling the flow using an image of the singularity, placed on the other side of the discontinuity. In this section, all the theoretical aspects of this approach are presented in Section 4.3.1 along with all the equations required to solve these problems. After that, a practical example of this method used in wind tunnel experiments is given in Section 4.3.2. Finally, the method is generalized by making use of successive reflections as a way of modeling the problem of a 2D airfoil submerged in an axial jet. This is discussed in Section 4.3.3.

4.3.1. Thin Airfoil in Parallel Streams

The flow field of an airfoil submerged into a propeller slipstream, as was shown in Figure 4.1, can be seen as an expended case of an airfoil in the vicinity of a single boundary between non-uniform parallel streams. This is schematically shown for a single boundary in Figure 4.2. The airfoil is located in the lower stream (index 0) and it can be represented by a single vortex. The boundary is a free surface and hence no forces should be present at it. However, the vortex will introduce some disturbance on the boundary and hence an image vortex in domain 1 should account for that. For each domain, there exists a different potential function. It is assumed that the disturbance created by the vortex will be small, meaning the problem can be solved by making use of the small disturbance theory. The use of this assumption makes it is possible to satisfy the boundary conditions at the undisturbed surface instead of at the true disturbed surface [36].

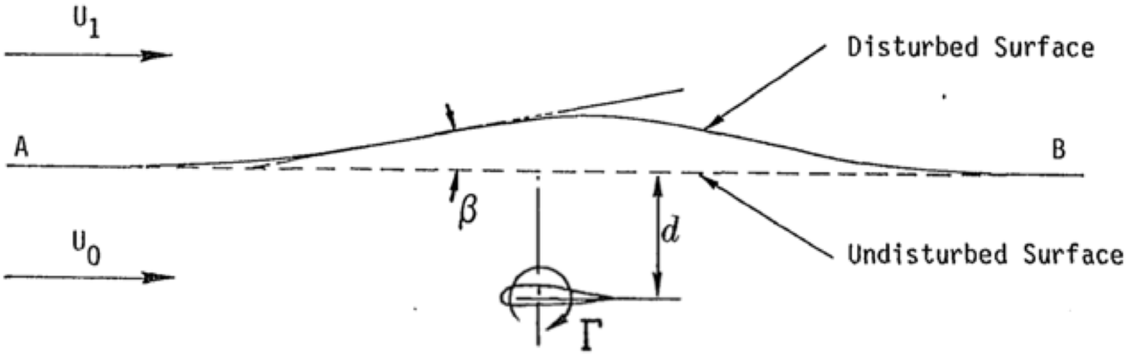

Figure 4.2: Visualization of a vortex in the proximity of a velocity discontinuity [31]

The two boundary conditions at the streamline are that the pressure on both sides must be equal and that the slope of the disturbance must be equal. The former condition can be presented by Equation 4.4, where u denotes the disturbance velocity in (horizontal) x-direction. The latter condition can be represented by Equation 4.5, where v denotes the disturbance velocity in (vertical) y-direction. The disturbance velocities are the induced velocities by the original vortex and its image. The disturbances created by a single vortex, expressed in Cartesian coordinates, can be seen in Equation 4.6 and 4.7 for the horizontal and vertical direction respectively. For this case, the original vortex is distance $-d$ from the streamline ($y = 0$) and therefore, the image is at distance $+d$ from the boundary. Since the velocity in domain 1 is not zero, the image strength must be scaled compared to the circulation of the original vortex. By satisfying the boundary conditions on the streamline, the strength of the image can be determined.

$$u_0 U_0 = u_1 U_1 \qquad (4.4) \qquad \frac{v_0}{U_0} = \frac{v_1}{U_1} \qquad (4.5) \qquad u = \frac{\Gamma}{2\pi}\frac{y}{x^2+y^2} \qquad (4.6) \qquad v = -\frac{\Gamma}{2\pi}\frac{x}{x^2+y^2} \qquad (4.7)$$

However, the determination of the induced velocities in the upper domain, where no real vortex is present, is not the same as for the lower domain. Due to the velocity discontinuity, every domain has a different representative vortex system. To further elaborate on that, Figure 4.3 is used. Firstly, to calculate the induced velocity components in the lower domain ($y < 0$), there are two vortices that should be taken into account. There is the influence of the original vortex plus that of the image vortex located in the upper stream. The strength of this image vortex is scaled by λ_0 compared to the original one. This means that there are two components for the disturbance velocities in the lower domain. The flow for domain 0 can be visualized using a representative vortex system as shown in Figure 4.3a [31].

For the upper stream ($y > 0$), the representative system is different. In this domain, there is only the influence of the original vortex, since there is no actual singularity at the image point ($+d$). This means that the image vortex is only experienced by the lower domain. However, the influence of the original vortex experienced in the upper domain is also not equal to that in the lower domain. Since the velocity in the upper region is different than that in the lower domain, the influence of the original vortex must be scaled to account for the velocity jump. Therefore, the influence is scaled by λ_1 compared to the original value of the vortex. The representative flow field for domain 1 can be seen in Figure 4.3b [31].

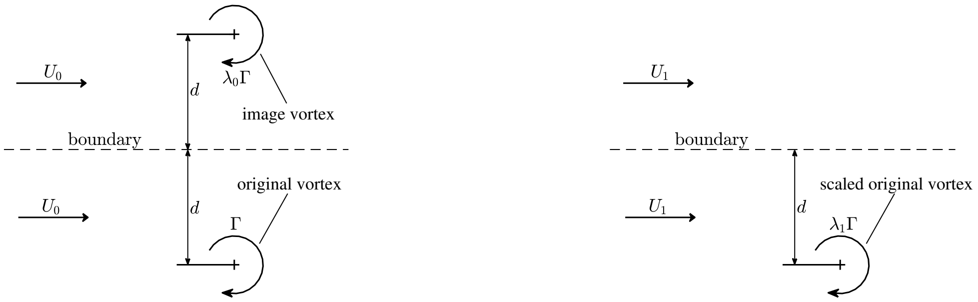

(a) Situation for domain 0

(b) Situation for domain 1

Figure 4.3: Representative vortex system for both domains to determine the induced velocity components [31]

As mentioned above, the strengths λ_0 and λ_1 can be determined by satisfying the boundary conditions at the jet boundary. The induced velocities in both domains can be determined using the two representative flow systems and by filling in Equations 4.6 and 4.7. For the lower domain, the disturbance velocity in x-direction is defined in Equation 4.8. For the upper domain, the horizontal induced velocity component can be defined using Equation 4.9.

$$u_0 = \frac{\Gamma}{2\pi}\left\{\frac{d}{x^2+d^2} + \lambda_0 \frac{-d}{x^2+(-d)^2}\right\} \tag{4.8}$$

$$u_1 = \lambda_1 \frac{\Gamma}{2\pi}\frac{d}{x^2+d^2} \tag{4.9}$$

Similarly, for the disturbance velocities in the y-direction, Equation 4.10 and 4.11 are the result for the lower and upper domain respectively.

$$v_0 = -\frac{\Gamma}{2\pi}\left\{\frac{x}{x^2+d^2} + \lambda_0 \frac{x}{x^2+(-d)^2}\right\} \tag{4.10}$$

$$v_1 = -\lambda_1 \frac{\Gamma}{2\pi}\frac{x}{x^2+d^2} \tag{4.11}$$

Now the disturbance velocities are determined for the two domains, the boundary conditions can be checked and the proper values of λ_0 and λ_1 can be determined. By filling in the disturbance velocities in Equation 4.4 and 4.5, the two scaling factors can be written as a function of the velocity jump. The definitions of λ_0 and λ_1 can be seen in Equation 4.12 and 4.13 respectively.

$$\lambda_0 = \frac{U_0^2 - U_1^2}{U_0^2 + U_1^2} \tag{4.12}$$

$$\lambda_1 = \frac{U_0}{U_1}(1-\lambda_0) = \frac{2U_1U_0}{U_0^2+U_1^2} \tag{4.13}$$

The idea of image vortices is a powerful technique in aerodynamics and is used in different correction methods. For example, in the case of an airfoil in ground effect, image vortices are used to simulate the effect of the ground plane. Furthermore, in wind tunnel experiments, the walls of tunnel can influence the aerodynamics. Similarly, the corrections are needed when experiments are performed in an open-jet wind tunnel.

4.3.2. Similarity with Wind Tunnel Boundary Corrections

The case of an airfoil close to a velocity discontinuity is also encountered in wind tunnels. Firstly, for closed test sections, the interference of the walls influence the aerodynamic characteristics of the model in the tunnel [37, 38]. The presence of boundaries in the wind tunnel can be modeled by using the method of images [38]. This means that the vortex system presented in Figure 4.2 has a solid wall on the boundary. The presence of the wall means that there is no vertical flow at the boundary and this can be modeled by assuming that U_1 is infinity large. If $U_1 >> U_0$, the value of λ_0 approaches -1, resulting in an image vortex of equal strength but of opposite sign. By doing this, the vertical velocity components of both the real vortex and the image vortex cancel each other at the surface, while the velocity components in the streamwise direction are added. This results in the zero normal flow condition at the wall, which is required [11]. This case is shown in Figure 4.4a. Now it also becomes clear why the original images must be scaled to be able to calculate its induced velocity components in the upper domain. Inside the wall, there are no velocity components and hence the influence of the original vortex must disappear. Using $U_1 >> U_0$ in Equation 4.13, the value of λ_1 goes to zero satisfying the above-mentioned condition.

For the open-jet wind tunnel, the boundary condition requires satisfying the linearized constant pressure at both sides of the streamline [38], since the air outside of the test section is stagnant. This requires the opposite case as for the closed wall situation, so where the horizontal components are canceled and the vertical ones are added to each other. This can be modeled by assuming that $U_1 \approx 0$ and hence λ_0 is equal to 1, indicating that the image vortex is of the same strength and equal in sign compared to the original one, which is shown in Figure 4.4b. The method of images is not limited to single singularities, but can be used for any distribution or collection of singularities or for multiple boundaries. Similar to the closed wind tunnel wall correction, the value of λ_1 goes towards zero, meaning there are no induced velocity components in the stagnant air.

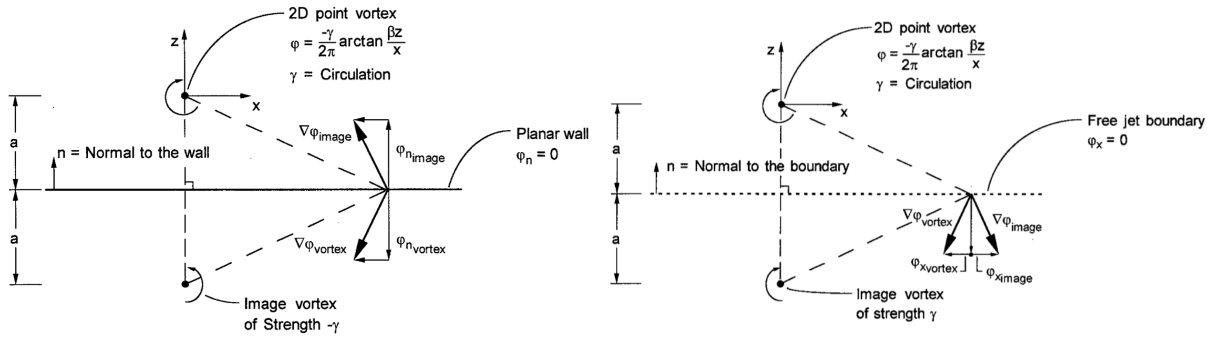

(a) Solid wall boundaries

(b) Free jet boundaries

Figure 4.4: Correction method for wind tunnel walls [38]

When the airfoil is represented by a vortex sheet, the same equations can be found, but then using the distributed circulation. In this section, only one boundary was considered at a time. However, this method can also be used for multiple boundaries and hence for a singularity within two jet boundaries, modeling the propeller slipstream with finite height. This will be discussed in the next section.

4.3.3. Method of Successive Reflections

The use of image vortices can also be applied to a case of an airfoil in a stream surrounded by not one but two different streams. This theory was developed in the research of Ting [10]. The problem is visualized in Figure 4.5 [10] and the setup is the following: a thin airfoil, presented by a distributed circulation ($\gamma(x)$), is located in a stream with velocity U_1. Above this middle region, there is another domain with a different velocity, namely U_2. Also below the airfoil domain, there is a region with a different velocity U_3. The thin airfoil is presented with a distributed vortex line placed at the chord line. By defining the camber line as a streamline, the required circulation of the airfoil is found by requiring zero normal velocity at the camber line [11]. The middle domain, including the airfoil, has height h and the upper region and the lower region are located at distance a and b from the airfoil respectively. For the case of a jet in a freestream, $U_1 = V_j$ and $U_2 = U_3 = V_\infty$.

Similarly, as for the case of a single jet boundary, the boundary conditions of equal pressure and slope at each dividing streamline must be satisfied. This is done using images in both the upper and lower domain. To start with the upper streamline, there must be an image at distance $2a$ from the airfoil, such that the boundary conditions are satisfied. The strength of this image is scaled with respect to the original vortex sheet. The scaling factor is α_v, of which the definition can be seen in Equation 4.14. This scaling factor is equal to the λ_0 for the case of a single discontinuity. For the lower streamline, the same is done at distance $2b$ from the airfoil. The total strength of this reflected image compared to the original vortex sheet is equal to β_v, of which the definition can be seen in Equation 4.15. Again, this is equal to the value of λ_0 and hence for a jet, where $U_2 = U_3$, the two coefficients are equal.

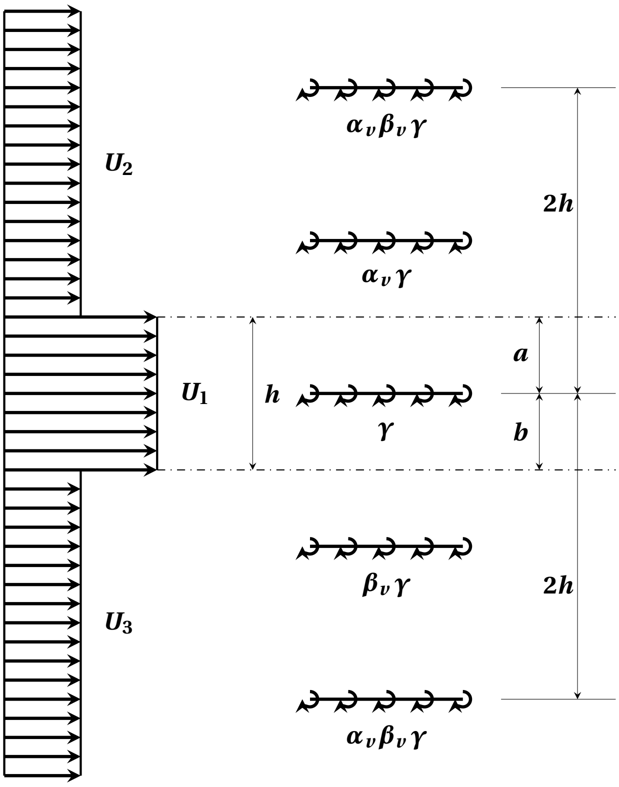

Figure 4.5: Schematic representation of the reflection vortex system [10]

However, due to the influence of the lower image, the boundary conditions on the upper streamline are not satisfied anymore. Likewise, the upper image has an influence on the lower dividing streamline. Therefore more images must be introduced. The two reflected vortex sheets will also have a reflection in the opposite dividing streamline. So, at a distance of $\pm 2h$ from the airfoil, two other images are presented, both of strength $\alpha_v\beta_v$ compared to the original. The two new images require again two more images and these can be reflected again and again. In this way, the boundary conditions at the two dividing streamlines are satisfied. Using this successive method, the influence of both the velocity increment, as well as the slipstream height, can be taken into account when finding the airfoil aerodynamic characteristics. The boundary condition at the airfoil vortex sheet is that of zero normal velocity, mathematically shown in Equation 4.16, where $m(x)$ is the camber line slope and α the angle of attack [10].

$$\alpha_v = \frac{U_1^2 - U_2^2}{U_1^2 + U_2^2} \tag{4.14}$$

$$\beta_v = \frac{U_1^2 - U_3^2}{U_1^2 + U_3^2} \tag{4.15}$$

$$\frac{v(x)}{U_1} = m(x) - \alpha \tag{4.16}$$

Figure 4.5 only shows the first set of images, meaning each set contains four images. The second set contains the images of the first set, so at a distance $2h$ further away than the initial one and scaled by another factor of $\alpha\beta$. The third set of images is based on the second set and this process is theoretically continued with an infinite amount of sets. The disturbance velocity in y-direction along the airfoil vortex sheet ($v(x)$) is represented by Equation 4.17. In this equation, ξ is the running variable for the integrals. The first term before the summation is the original influence of the airfoil vortex sheet. The particular set of images is denoted with j and the index 0 corresponds to the first set of images. This means that the circulation created by the airfoil now is influenced by an additional term of all the images.

$$\begin{aligned} v(x) = -\frac{1}{2\pi}\int_0^c \Bigg\{ \frac{1}{x-\xi} + \sum_{j=0,1,2,\ldots}^{\infty} (\alpha\beta)^j \Bigg[& \frac{\alpha(x-\xi)}{(x-\xi)^2 + 4\big(jh+a\big)^2} + \frac{\beta(x-\xi)}{(x-\xi)^2 + 4\big(jh+b\big)^2} + \\ & \frac{2\alpha\beta(x-\xi)}{(x-\xi)^2 + 4h^2\big(j+1\big)^2} \Bigg] \Bigg\} \gamma(\xi)\, d\xi \end{aligned} \tag{4.17}$$

The system of images is solved in a similar way as in the classical approach of the thin airfoil theory [11]. The circulation distribution must be discretized into a finite number of points. To get an analytical expression, the usual coordinate transformation is done. The variables θ (running variable) and φ (fixed position) are introduced to express the horizontal coordinate on the airfoil in an angular manner, as opposed to the linear expression using ξ and x respectively. The expression for the distributed vorticity along the airfoil chord line is also the same as for the normal thin airfoil case. This is done using a cosine Fourier series, as can be seen in Equation 4.18, where M denotes the total number of Fourier coefficients. The Fourier coefficients themselves are presented by A_m and what is important to note is that the circulation is a function of U_1 and not of V_∞.

$$\gamma(\varphi) = 2U_1 \left\{ A_0 \cot\left(\frac{\varphi}{2}\right) + \sum_{m=1,2,...}^{M} A_m \sin\left(m\varphi\right) \right\} \tag{4.18}$$

By filling in the expression for the distributed circulation and by using the boundary condition at the camber line, a set of linear equations is created. This can be seen in Equation 4.19, where the first part in the curly brackets is the term of the classical thin airfoil problem. The second term is the influence of the system of images. The term on the right-hand side, including the coefficients d_m, is a Fourier series representation of $m(x) - \alpha$, which is known for a specific airfoil. The camber line is divided into a total of I segments, at each of which the zero normal flow condition must be satisfied. By making the number of I large, the continuous circulation distribution is approached. Note that the number of segments is taken into account by the term φ, meaning Equation 4.19 must be satisfied at each segment.

$$\left\{ -A_0 + \sum_{m=1,2,...}^{M} A_m \cos m\varphi \right\} - \sum_{m=0,1,2,...}^{M} \sum_{j=0,1,2,...}^{N} \sum_{k=1}^{3} \left[A_m J_m \left(\alpha_v \beta_v\right)^j F_k \right] = d_0 + \sum_{m=1,2,...}^{M} d_m \cos m\varphi \tag{4.19}$$

In the image term, also the Fourier coefficients are shown. The effect of the images is influenced by the term J_x, which is basically a correction for the vertical displacement of the images and thus only a function of the geometrical properties of the system. The expression of these J_x terms can be seen in Equation 4.20 and 4.21. The total number of image reflection sets is given by N. As discussed before, $N = 0$ represents the most basic case, which means there are 4 image vortex sheets as shown in Figure 4.5. Theoretical, both the number of Fourier coefficients and the number of reflections should approach infinity to get the exact solution. This is not possible for calculations and both will be cut-off at values where the solution has converged [10].

$$J_0 = \frac{1}{\pi} \int_0^{\pi} \frac{\left(\cos\theta - \cos\varphi\right)\sin\theta}{\left(\cos\theta - \cos\varphi\right)^2 + Y_{jk}^2} \cot\frac{\varphi}{2}\, d\theta \tag{4.20}$$

$$J_m = \frac{1}{\pi} \int_0^{\pi} \frac{\left(\cos\theta - \cos\varphi\right)\sin\theta}{\left(\cos\theta - \cos\varphi\right)^2 + Y_{jk}^2} \sin m\theta\, d\theta \tag{4.21}$$

Equation 4.20 is used for the A_0 coefficient, while Equation 4.21 is used for the Fourier coefficients of index 1 or higher. The integrals are similar to the integrals solved in the classical thin airfoil problem, but in the denominator, an additional term is added (Y_{jk}). This is a matrix containing the corrections of image k from reflection set j, which can be seen in Equation 4.22. The term e_k is a vector containing the geometrical values of the middle region, given by Equation 4.23. Referring to figure 4.5, $k = 1$ is for the image of strength α_v, $k = 2$ is for the image of strength β_v and $k = 3$ is for the two images of strength $\alpha_v\beta_v$. The strength of particular image k from reflection set j is given by the term $\left(\alpha_v\beta_v\right)^j F_k$, where the vector F_k can be seen in Equation 4.24.

The integrals for J_0 and J_m are difficult to express analytically, due to the very lengthy expression obtained and no standard integrals exist for these terms. In the literature discussed [10], these integrals were evaluated by the use of contour integration and analytic formulas are given. However, it turned out that these formulas were incorrect. The system can also be solved in a numerical way using for example the trapezoidal method, given that the discretization is fine enough. It turned out that the values of the numerical approach were different than the values of the analytical formulas. More information regarding this discrepancy can be found in Appendix A. The trapezoidal method was used in this thesis to produce the discussed integrals.

$$Y_{jk} = 4\left(jh + e_k\right)/c \tag{4.22}$$

$$e_k = [a, b, h] \tag{4.23}$$

$$F_k = \left[\alpha_v, \beta_v, 2\alpha_v\beta_v\right] \tag{4.24}$$

Equation 4.19 can be solved for the unknown Fourier coefficients by rewriting the equation in the form of Equation 4.25. In this way, the column vector of Fourier coefficients A_m can be calculated by simply taking the inverse of matrix B and multiplying it with column vector D. D is a single value for each evaluation at position

φ and hence the vector elements are simply the values for the different points along the airfoil camber line. The first and third term of Equation 4.19, including the cosine Fourier coefficients, can be written differently. The A_0 and d_0 coefficients can be easily put into the summation, since the cosine of 0 is 1. This operation can be seen in Equation 4.26. The only thing that needs to be noted is that for A_0, the value should be multiplied with -1, since there is a minus sign in front of the term in Equation 4.19. The next thing to do is to isolate the Fourier coefficients A_m from the second term. This is done using the summation rule, which tells that the summations of products can be written as products of summations.

$$[\![B]\!]\,[A_m] = [D] \tag{4.25}$$

$$A_0 + \sum_{m=1,2,...}^{M} A_m \cos m\varphi = \sum_{m=0,1,2,...}^{M} A_m \cos m\varphi \tag{4.26}$$

Now the Fourier coefficients A_m are isolated, the general equation can be written in the form of a system of linear equations. The final form can be seen in Equation 4.27. The B matrix is an $I \times m$ matrix for the different Fourier coefficients and the different evaluation points. For $m = 0$, the first part of matrix B should be -1, as discussed above. The vector containing A_m has dimensions $M \times 1$ and vector D, containing the Fourier values of the airfoil geometry, has dimensions $I \times 1$. The integrals for J_m are evaluated numerically using the trapezoidal method. Filling in the values of A_m in Equation 4.18, and integrating the results over the airfoil gives the circulation of the airfoil. Using this circulation, the new sectional lift can be calculated, which will be different than for the case of an infinitely high jet. The system of equations is much simplified for the case where the airfoil is located in the middle of a jet surrounded by the freestream. In this case, $\alpha_v = \beta_v$, $a = b = h/2$, $U_2 = U_3 = V_\infty$ and $U_1 = V_j$.

$$\underbrace{\left[\!\!\left[\cos m\varphi - \sum_{j=0,1,2,...}^{N} \sum_{k=1}^{3} J_m\left(\alpha_v \beta_v\right)^j F_k\right]\!\!\right]}_{B=I\times M} \circ \underbrace{[A_m]}_{M\times 1} = \underbrace{\left[\sum_{m=0,1,2,...}^{M} d_m \cos m\varphi\right]}_{D=I\times 1} \tag{4.27}$$

To get a more visual idea of the influence of the images, a close-up of the airfoil with the first two images is presented in Figure 4.6. Most of the circulation is concentrated at the LE of the airfoil due to the suction peak [30]. In the figure, Γ_1 represents the circulation of the LE part of the airfoil and this induces a downwash on the rest of the airfoil. At a specific point along the chord, the induced velocity is denoted by V_{Γ_1}. The main circulation of the images is denoted by Γ_2 and Γ_3 for the upper and lower image respectively. The two images will also introduce induced velocities on the airfoil sheet and these are denoted by V_{Γ_2} and V_{Γ_3}.

Since the vertical position of the images differs, the direction of the total induced velocity is not the same for the two images. For the case of an airfoil in the middle of the jet, the horizontal components cancel and the resultant downwash is only directed in the vertical direction. This is in the same direction as the original downwash and hence the circulation strength of the airfoil must become less, to satisfy the boundary condition at the chord line. This reduced circulation means that the total sectional lift will be lower, as is expected when the jet is small. The first two images will have the biggest influence, since the distance increases for the other images. The larger the distance, the smaller the influence of a vortex, see Equation 4.6 and 4.7. A convergence study was done to determine the required amount of image sets, see Section 4.4.

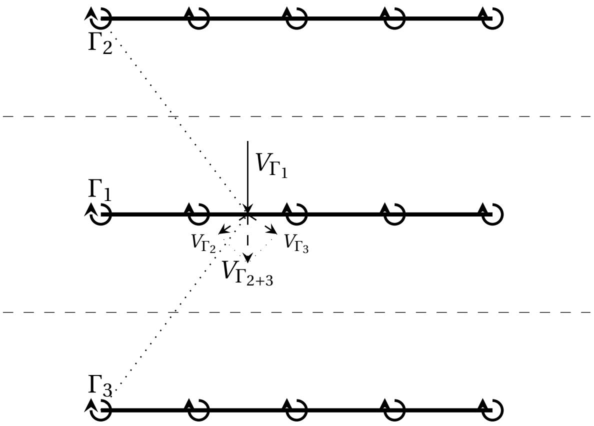

Figure 4.6: Schematic representation of the reflection vortex system

The extra downwash of the images results in a decrease in required airfoil circulation and hence a reduction in total sectional circulation. Using the Kutta-Joukowski theorem (Equation 3.8) and the local velocity (V_j), the sectional lift is calculated. This sectional lift will be lower than that of the case in which an infinitely high jet is assumed. This means that the finite slipstream height can be modeled in the form of a correction factor for the local lift. The previously defined K_l was based on l_∞, but the correction factor should be applied to the lift coefficient. When the local lift is non-dimensionalized using the jet velocity, the sectional lift coefficient (C_{l_j}) will be lower than for the airfoil with no jet (C_{l_∞}). For an infinitely high slipstream, the lift can be simply calculated by the same C_l as for the no jet case, but using the jet velocity. So for this limiting case $C_{l_j} = C_{l_\infty}$, since there is no correction due to the images and $K_l = V_j^2/V_\infty^2$. The ratio of C_{l_j} to C_{l_∞} is defined as the correction factor and is presented by K_{C_l}. Its definition and relation to the lift ratio K_l can be seen in Equation 4.28. K_{C_l} will have an upper limit of 1, in the case of an infinitely high jet, while the lower limit is V_∞^2/V_j^2 for the case of an infinitesimal slipstream height.

$$K_{C_l} = \frac{C_{l_j}}{C_{l_\infty}} = \frac{\frac{l_j}{\left(0.5\rho V_j^2 c\right)}}{\frac{l_\infty}{\left(0.5\rho V_\infty^2 c\right)}} = K_l \frac{V_\infty^2}{V_j^2} \tag{4.28}$$

4.3.4. Vortex Sheets

Using the method of successive reflections, the flow field for an airfoil submerged in a jet contains two different incoming velocities, since $U_2 = U_3$. In this approach, the different domains will have different potential functions. However in Section 3.1.3, a different model was presented to model the influence of the propeller slipstream in 2D. This was done using two infinitely long vortex sheets at the boundaries of the jet and was visualized for a small domain in Figure 3.5a. This method is similar, but is based on only a single potential function, which includes the vortices from the boundaries. However, by modeling the jet boundaries as vortex sheets, the boundary conditions of constant pressure and slope must also be satisfied on these sheets. Hence images are also needed in this method to account for the perturbations along the jet boundaries and the result will be similar to the method presented.

4.4. Convergence Study

In this section, a convergence study of the successive reflection method is given. To check the convergence of the numerical method discussed in Section 4.3.3, the three main parameters which are used in the system of equations, are varied. The first one is the total number of control points on the airfoil vortex sheet (I) to estimate the continuous vortex circulation distribution. To check the convergence, the relative discretization error (ϵ_{rel}) is used. The definition of this error can be seen in Equation 4.29.

$$\epsilon_{rel} = \frac{\frac{f(x_{n+1}) - f(x_n)}{f(x_n)}}{\frac{x_{n+1} - x_n}{x_n}} \tag{4.29}$$

The difference in lift using two different number of control points is normalized by the relative increase in the number of control points, such that the error is independent on the increase. It turned out that the convergence trend of the number of control points is dependent on the height of the slipstream, however, the rate of convergence (slope of the logarithm of the relative error) was equal for all height values. If the relative error is equal to zero, the solution is fully converged since an increase in the number of panels will not result in a different solution. In Figure 4.7, the convergence trend for 8 different slipstream heights is shown. All shown trends have the relative error smaller than 1% for $I > 100$ and for a total of 200 panels, the largest relative error is at around 0.5%. Even for the smaller slipstream heights, the relative error was less than 1% for 200 points. On a personal computer, the method solves for 200 points within a couple of seconds to indicate the order of magnitude for the computational time, while using 1000 points takes up to around a minute.

For the larger slipstream heights, where the lift value of the airfoil is almost unchanged compared to the infinitely high slipstream, the relative error is smaller than 0.5%, already for a lower number of panels (< 50). This is since the images are far away from the airfoil and hence their influence on the vortex sheet is small. For an infinitely high slipstream, the convergence trend is equal to that of the thin airfoil theory. It turned out that for the variation of the number of control points, the convergence rate was linear, meaning that doubling the number of panels will result in half of the error. To have a compromise between accuracy and computational time, 200 panels were used for the analyses in this thesis.

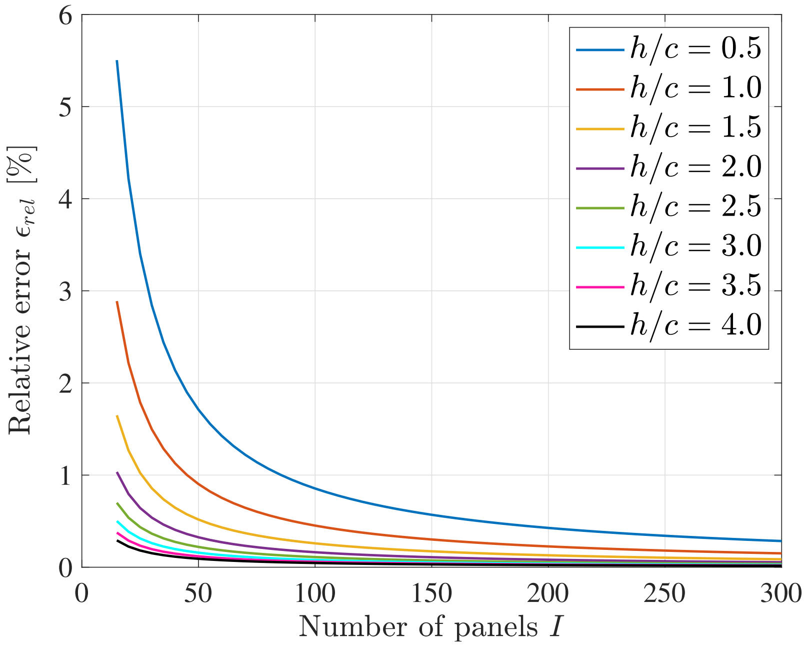

Figure 4.7: Convergence trends for the discretization of the vortex panel for different slipstream height ratios (h/c)

The convergence study of the number of Fourier coefficients and the number of image sets showed quicker convergence. The result can be seen in Figure 4.8a and 4.8b respectively. Especially, the number of Fourier coefficients converges really fast and 3 of them is already enough for the analysis. For the number of images, 6 sets seem to be the lowest number for which the solution converges. For a larger number of image sets, the vertical position of the image is so far away from the airfoil, that the influence of them is negligible. When the slipstream height is reduced, the images are closer to the airfoil and hence have more influence. However, the strength of the images is still reduced in each set so also when the slipstream is very small, the system converges for a maximum of 10 sets. Since the number of Fourier coefficients and image sets is quite small, the computational time is mainly determined by the number of points along the airfoil camber line.

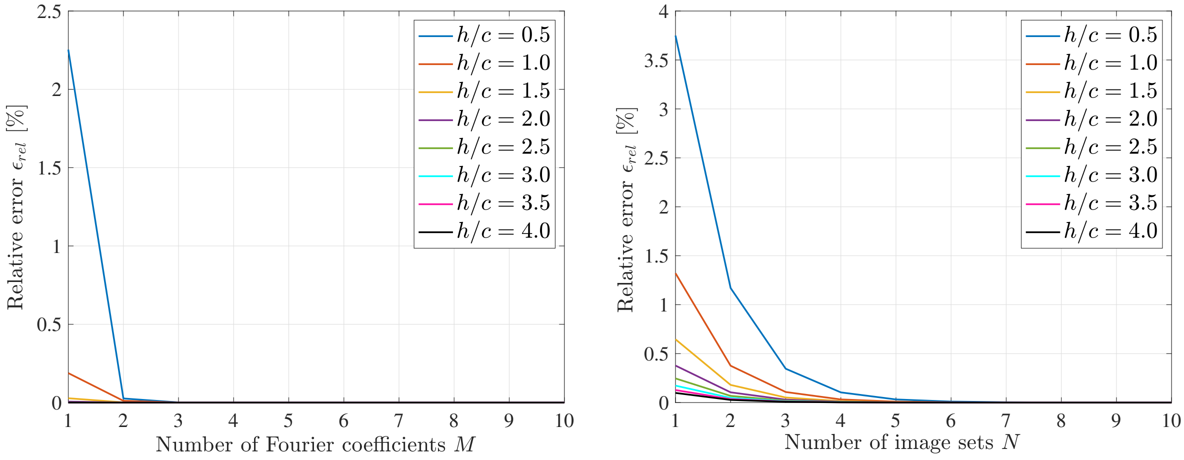

(a) Number of Fourier coefficients

(b) Number of image sets

Figure 4.8: Convergence trends for the number Fourier coefficients and the number of image sets for different slipstream height ratios (h/c)

It seems mathematically incorrect to have a very small number of Fourier coefficients, while having a large number of discretization points. This would mean that the system of Equation 4.27 is heavily over-determined and no exact solution for the Fourier coefficients can be found. The system would be determined if there were the same number of Fourier coefficients as control points. However, using a least-squares method, only a very small error is encountered and a converged solution is found already with a small number of Fourier coefficients. This means that the flow boundary condition is probably not met at any of the control points, but the resultant aerodynamic parameters, such as the circulation and the C_l are approximated very well compared to the determined system of equations, which is computationally much more expensive. So to conclude, using 200 panels, 5 Fourier coefficients, and 10 image sets, the analysis is close to the exact value, while still having a low computational cost. The analyses in this thesis were performed with the values mentioned above, and the results of these analyses are presented in Chapter 6.

4.5. Limitations of Method

The numerical method also has some limitations. The method does not converge when the slipstream height is equal to zero or the airfoil is located exactly at the boundary, due to the numerical nature of the image approach. One other limitation of the method is the behaviour when very small slipstream heights are modeled. As discussed in Section 4.3.3, the lower bound of K_{C_l} is V_∞^2/V_j^2. For most of the presented data, $V_j = 2V_\infty$ is used and hence the lower bound is 0.25. In Figure 4.9, a close-up of the results for small slipstream ratios is presented. The theoretical lower bound is presented with the black dashed line and for $h/c < 0.01$, the values are lower than would be theoretically possible. This means that the absolute sectional lift would be reduced compared to the no jet case, which is not possible. This is probably due to the close proximity of the images in combination with the numerical nature of the method. The method assumes linearity of the flow, hence the singularities at the boundary are producing small perturbations to the flow field. In the limiting case of $h/c \to 0$, the perturbations are not small and the problem cannot be linearized. These small heights are only encountered at wing segments at the very edge of the slipstream. In the analysis tool, the lift correction is limited to the theoretical lower limit, such that sectional lift can not be lower than for an airfoil without jet.

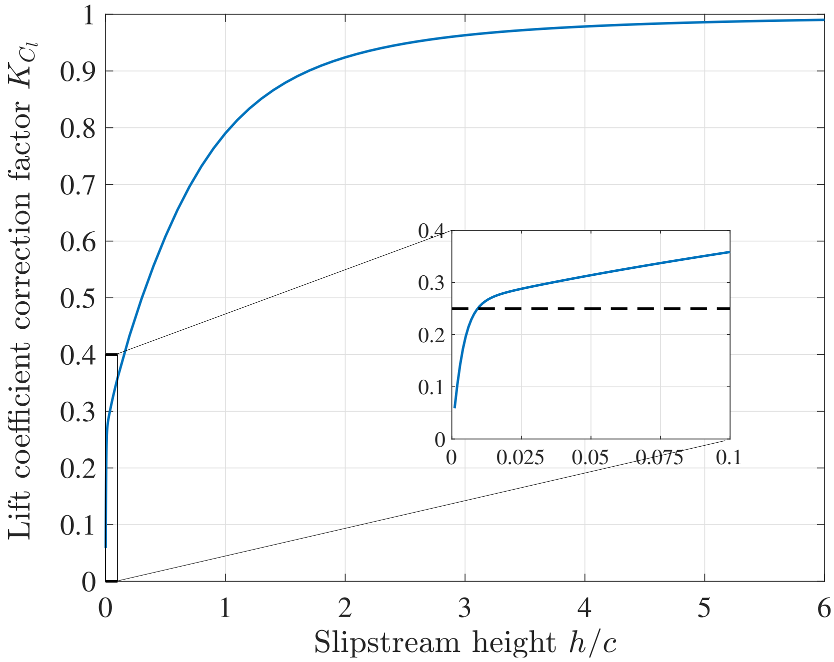

Figure 4.9: Lift coefficient correction factor (K_{C_l}) variation at small values of h/c

Another limitation originates from the used assumptions. The method is based on the simplification that the jet has a constant induced velocity throughout the jet, like the AD theory. No vertical velocity variations are modeled as is done in the BEM, and at the jet boundary, there is an instantaneous jump in velocity. These assumptions are physically not possible due to the 3D blade loading and the fluid viscosity, which would diffuse the velocity jump in the shear layer. Furthermore, the method assumes that the airfoil is placed infinitely far from the actuator disk and hence no slipstream contraction is present. The method only takes the axial velocity component into account and the swirl is not modeled. This method is further limited to the airfoil located in the middle domain, so inside the jet. When the airfoil is located in the upper or lower domain, with the jet surpassing the airfoil, the image method is changed since the images are now either located inside the jet or in the other freestream domain, depending on the airfoil location. The used literature gave insufficient knowledge to set up a system of equations for these other cases and hence more in-depth calculations, using the different potential functions, should be performed to define a vortex image system for the flows with the airfoil not located in the jet. Since the method makes use of the thin airfoil theory, the thickness of the airfoil is not taken into account and the separate effect of the jet on the upper and lower surface and therefore the pressure distribution can not be investigated. The 2D panel method could be extended towards a method using successive reflections, but the method would be very lengthy and probably an iterative method would be needed to solve the problem.

Finally, the assumption that the two boundaries of the jet, modeled as streamlines in this approach, are straight and rigid surfaces that come from and extend towards infinity is not valid throughout the whole flow domain. Firstly, the streamlines close to the airfoil are curving around it and are not straight. So for small slipstreams, the jet would be distorted and hence the relative position of the airfoil inside the jet as seen from infinitely far away is different than seen locally. Thus the airfoil location should either be specified based on the local orientation inside the jet, but then the solution is not valid far away from the body, or as seen from far away, but then the local solution is not valid anymore, meaning the calculated sectional lift is incorrect. The former case is needed to calculate the correct sectional lift and hence the local position of the airfoil is used. Finally, the fact that the images are scaled with respect to the original vortex means that at the boundary, both an axial and vertical resultant velocity component is present and the displacement of the dividing streamlines far downstream would be infinite [10].

4.6. Swirl Component of the Flow

The remaining problem is the modeling of the swirl in the slipstream. In most of the LL or VLM propeller-wing analyses, the propeller and wing aerodynamics are calculated separately. The tangential velocity component in the slipstream is modeled as a vertical velocity component at the wing and this will change the local angle of attack. However, by assuming this as 'simply' a change in angle of attack, the rotating motion of the flow is neglected. So by modeling the tangential flow as vertical velocity, it is assumed that the flow is not rotating in the third dimension and hence after the airfoil, the flow will continue in a straight line, which is not the case in 3D. Unfortunately, no research was found which includes this swirling aspect in the low-fidelity propeller-wing interaction using potential flow methods and hence no correction method for the tangential velocity component is applied in this thesis.

To start off with, the effect of the swirling motion can be investigated by the use of CFD simulations. The effects of the swirl flow can be investigated separately from the finite slipstream height effect and it could be that the effect of the swirl itself is small. If it turns out that the effect of the swirl is large, a method must be thought of to include this effect in the potential flow analysis. Perhaps a similar method as done by [39], could be applied to this problem. In the swirl recovery vane optimization tool from [39], the potential flow lifting-line analysis is corrected for the influence of the slipstream deformation by the wing. A surrogate-based optimization technique is used to reduce the computational time of the high-fidelity correction method. By using this surrogate technique, the optimization is primarily done using the low-cost surrogate model. Only for verification purposes, the high-fidelity tool is used occasionally [39].

To conclude this chapter, the method of image vortices is applied to find a solution for the circulation of a 2D airfoil in a slipstream of finite height, as is explained in Section 4.3.3. The dividing streamlines are used as planes of reflection and by using some basic algebraic operations, the system can be solved for the unknown Fourier coefficients of the distributed vorticity [10]. To validate the calculation method fully, CFD analyses should be performed. Since no potential flow correction method is found for the swirl velocity in the slipstream, the swirl will be modeled as a vertical velocity component as is done in existing tools. The relative magnitude of the error introduced by using this approach will be investigated by performing CFD simulations including propeller swirl.

5

2D CFD Simulation Setup

The potential flow approach discussed in the previous chapter provides a model to compute the lift of an airfoil immersed in a jet of finite height. This model is applied to the case of an airfoil in a propeller slipstream with uniform velocity distribution. The method needs to be validated. The validation is done using CFD and in this chapter, the setup of the simulations is explained. Firstly, the theory of modeling potential flow in a numerical way is discussed in Section 5.1. The layout of the computational domain and the used boundary conditions for the CFD simulations are defined in Section 5.2. An important factor to take into account when modeling potential flow is the numerical viscosity, which is elaborated on in Section 5.3. Here it is checked if it is possible to approximate a potential flow analysis in the first place. For the specific problem of an airfoil submerged in a jet, the grid convergence is discussed in Sections 5.2 and 5.4 respectively.

5.1. CFD Simulations of Potential Flow

The CFD simulations discussed in Section 3.4 used an actuator disk model to get the propeller induced velocity. However, the slipstream velocities in this approach are dependent on the horizontal distance between the actuator surface and the airfoil [33]. Furthermore, taken into account the compressibility of the air, the correction factor β had values larger than unity, which is not possible for the incompressible potential flow analysis. As discussed in Section 4.2, the vorticity in the shear layer between the freestream and the jet can not be modeled using potential flow techniques. By using the Euler equations, the irrotational conditions can be removed, and hence the problem can be modeled without the need for image vortices.

Every fluid problem can, in theory, be solved using the Navier-Stokes (NS) equations, the continuity equation and the energy equation. These equations are the PDEs describing the motion of fluid in the three spatial directions and how the velocity, pressure, temperature, and density are related. Due to the non-linear advection terms in the equations, no general analytical formulas exist. The equations can be solved numerically by using a finite volume or finite element discretization of the flow domain. In order to perform a fair comparison with the potential-flow method, it was decided to perform the validation CFD simulations for an incompressible and inviscid flow. This means that the Euler equations were solved.

If the flow field is modeled as being steady, incompressible and inviscid, the NS equations are much simplified and they are reduced to the so-called Euler equations. The incompressible and constant density assumption means the energy equation can be omitted and the continuity equation is reduced to Equation 5.1. The steady flow assumption results in the removal of all the time derivatives. Finally, the inviscid assumption gets rid of the viscosity terms and the momentum equation in vector form is reduced to Equation 5.2. Using the Euler equations, the potential flow can be approximated and in theory, all potential flow solutions should be solutions of the Euler equations.

$$\nabla \cdot \vec{V} = 0 \tag{5.1}$$

$$\vec{V} \cdot \nabla \vec{V} = -\frac{\nabla p}{\rho} \tag{5.2}$$

To solve the Euler equations, the flow domain must be discretized using a grid. The result of the flow problem depends greatly on the quality of the grid. The spatial discretization ensures that the PDEs are reduced to a set of ordinary differential equations. There are different types of spatial discretization and most CFD codes use finite volume methods. The conservation laws are integrated on the surface of the control volume and this is done numerically. However, the use of numerical schemes introduces errors, of which one is the introduction of the so-called numerical viscosity. More information regarding this subject is given in Section 5.3. Ansys was used to solve the Euler equations and both Fluent and CFX were compared. The difference is that the former is based on a cell-centered method, while the latter is a vertex-centered method. Fluent can solve for pure 2D grids, while CFX needs at least one cell in the third dimension. Finally, Fluent has the option to set the solver to inviscid, as is required for the potential flow approximation. CFX does not have this option, but turbulence can be switched off and the viscosity can be manually adapted to very small values.

5.2. Computational Domain of the 2D CFD Simulations

The modeling of the domain of the airfoil submerged in a propeller slipstream for the CFD analysis is discussed in this section. For the potential flow theory, the boundary conditions of zero disturbances are placed infinitely far away from the airfoil, as discussed in Section 3.2.1. This is impossible for the CFD computational domain, but to minimize the influence of the boundaries, the domain is taken to be a square with lengths of $100c$. The computational domain can be seen in Figure 5.1. The effect of the domain size on the lift value is further discussed in Appendix B. For all the simulations performed, it was assumed that the airfoil was in the middle of the jet.

The slipstream was introduced into the simulations by specifying a velocity increment compared to freestream conditions at the inlet of the domain to avoid the problems encountered with the actuator disk modeling, as discussed in Section 3.4. In this way, it is assumed that the propeller slipstream is fully developed. The vertical position of the airfoil in the jet should be defined locally as was done in the small disturbance theory. However, in the CFD simulation, this is not possible since the inlet plane is far away from the airfoil and the disturbances of the jet are initially unknown. Since the disturbances are assumed to be small, the local vertical position of the airfoil in the jet does not differ much compared to the theoretical upstream position. This means that the position of the jet inlet plane is centered around the vertical coordinate of the airfoil. The airfoil is positioned in the middle of the domain and hence, the boundaries of the inlet plane are positioned at $\pm h/2$.

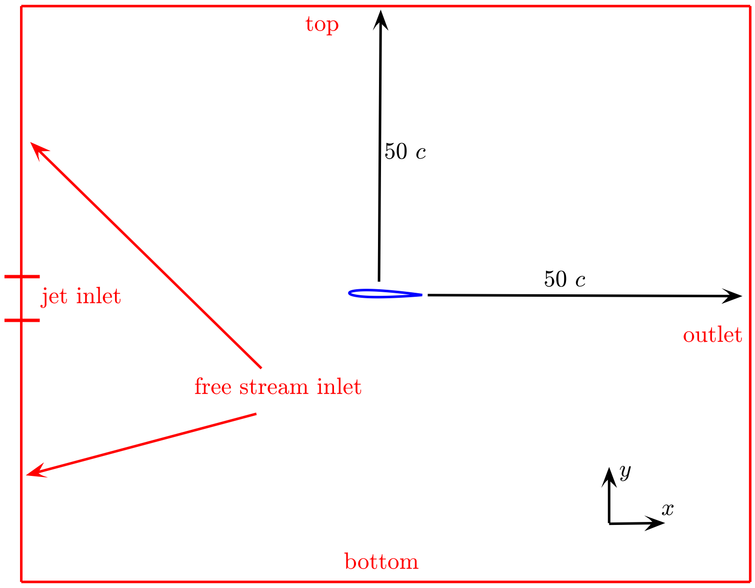

Figure 5.1: 2D computational domain for the CFD simulations

The inlet planes are modeled to have a velocity inlet condition, while the outlet is modeled to have a freestream static pressure outlet. The top and bottom are modeled using free slip surfaces. In this way, no viscous effects are modeled while maintaining the zero normal velocity condition at these surfaces. The same is done for the airfoil surface and the used airfoil for all the simulations is the NACA 0012. Since CFX needs one cell in the z-direction, the sides are modeled with the symmetry condition and therefore no 3D effects are simulated.

5.3. Impact of Numerical Viscosity

The potential flow models the flow field to have no viscous effect and hence the flow stays irrotational. However, the inherent shortcoming of numerical schemes is the creation of numerical viscosity, which results in viscosity effects. This is basically the error obtained due to the truncation of the Taylor series expansion. The truncation error has the character of an additional diffusion term, and hence the name numerical viscosity [40]. The value of the error is dependent on the scheme chosen. The central difference scheme, having a second order accuracy, has a dissipative error of order 4, while first order accuracy of the upwind scheme yields an error of order 2. However, the central difference scheme could lead to oscillating behaviour and problems with convergence [40, 41]. Most CFD codes automatically choose between the different schemes depending on the values of the gradient.

Any spatial gradient is smoothed due to the finiteness of the cells, especially if the grid cells are not aligned with the gradient. That is the reason that inflation layers are often implemented close to the surface of an object. Numerical viscosity can be minimized by making the grid very fine, but this will increase the computational time of the solver. To check the effect of numerical viscosity on the solution of the CFD solver, a simple cylinder flow could be analyzed and the obtained pressure distribution can be compared to the analytical one of the potential flow analysis. Next to that, the effect of numerical viscosity on the airfoil analysis is presented after which this section is concluded with the importance of mesh density on the jet boundary.

Note that the results of this section are somewhat arbitrary, since the chosen meshes were more or less random. No systematic approach was done at this stage to refine the mesh, but the difference between the coarse and fine meshes was used to get a more qualitative representation of the effect of the numerical viscosity. It seems intuitive to use a low number of mesh cells, since no turbulence or other phenomena have to be modeled, but this is not true since the potential flow does not allow for any viscosity effects. More information regarding the precise mesh size used for the actual CFD simulations of the validation and the accompanying mesh dependency study is presented in Section 5.4.

5.3.1. Flow around a Cylinder

The case of a flow around a cylinder (or circle in 2D) can be simply modeled using potential flow and this results in an analytical equation for the pressure distribution over the surface, given by Equation 5.3. The potential flow analysis uses a doublet singularity to model the cylinder in a freestream and the strength determines the diameter of the circle in 2D. In this equation, C_p is the pressure coefficient and θ is the circumferential location on the cylinder.

$$C_p = 1 - 4\sin^2\theta \tag{5.3}$$

In the 2D analysis of the cylinder, a large domain was used and different meshes were created using ICEM CFD. Both Fluent and CFX simulations were performed to determine the difference between the two methods. To start off with the coarse mesh, the simulation results can be seen in Figure 5.2. In Figure 5.2a, the mesh around the cylinder can be seen and the number of elements at the surface is around 60. The large gradients close to the boundary will result in a significant amount of numerical viscosity. The velocity flow field around the cylinder is visualized in Figure 5.2b, where the absolute velocity is plotted. The numerical viscosity results in a viscous effect, normally encountered only for low Re flow. The formation of these wavy vortices is called a Kármán vortex street and is unsteady. This was confirmed by the fact that the steady state approach did not show any convergence. Continuing the simulation would yield a different state of the flow field. The formation of these vortices and corresponding flow separation is not modeled by potential flow. The obtained asymmetric flow field will result in a net force on the cylinder, while there is no net force on the cylinder in the potential flow analysis.

By increasing the mesh density of the mesh around the cylinder, the numerical viscosity is reduced. The results of this analysis is shown in Figure 5.3. The mesh close to the cylinder is shown in Figure 5.3a and a total number of 3140 mesh points were created along the cylinder. The gradients can now be better resolved and hence the solution should converge towards the potential flow solution. The resulting velocity flow field is shown in Figure 5.3b. The Kármán vortex street had disappeared and the simulation converged to a steady state solution. This flow field looks more similar to the expected result for an inviscid flow and the pressure forces are symmetric.

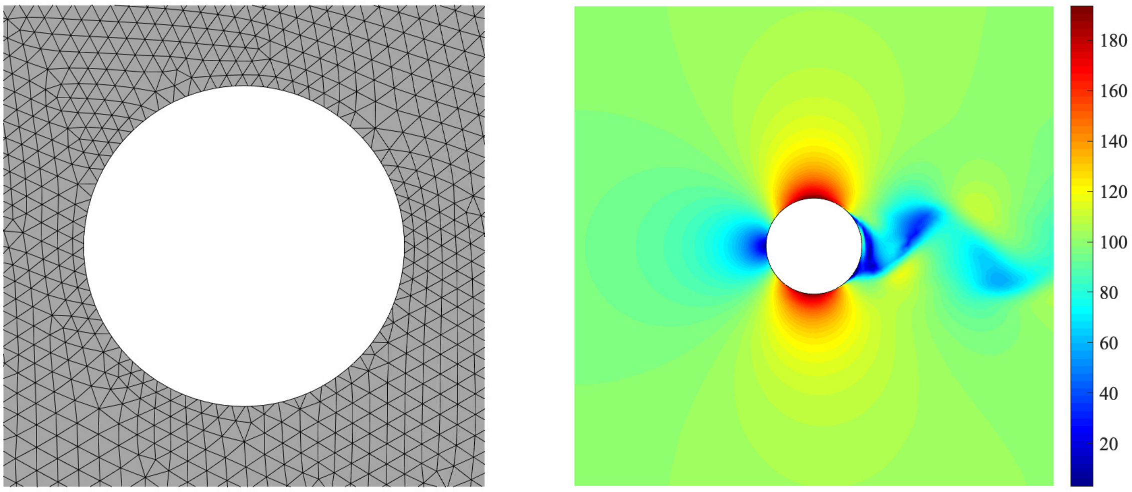

(a) Close-up of cylinder mesh

(b) Flow field of absolute velocity

Figure 5.2: Euler analysis of flow around cylinder using a coarse mesh

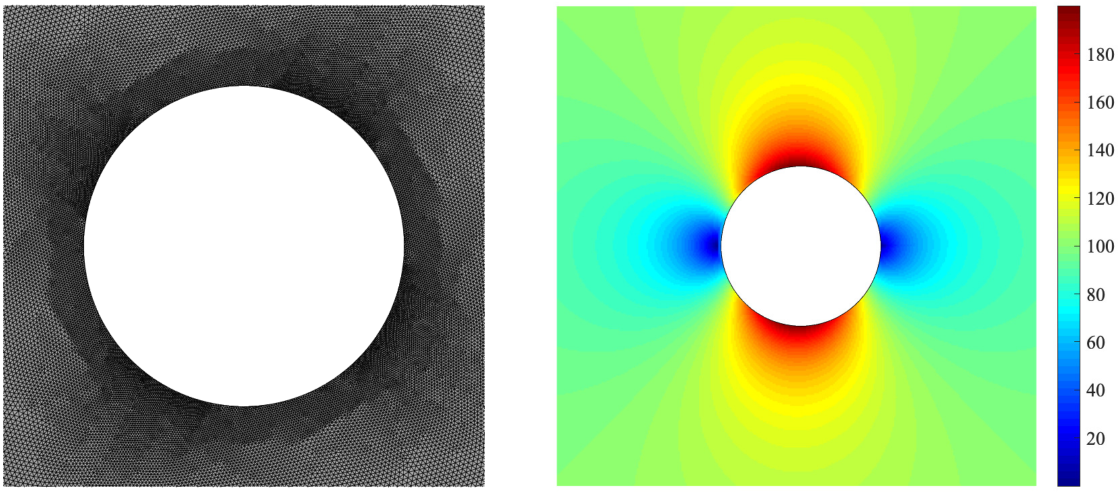

(a) Close-up of cylinder mesh

(b) Flow field of absolute velocity

Figure 5.3: Euler analysis of flow around cylinder using a fine mesh

Finally, the pressure distribution around the cylinder is checked. In Figure 5.4, the pressure coefficient distribution along the cylinder surface is plotted. For the CFD simulation, the C_p is calculated using Equation 5.4. The potential flow solution using Equation 5.3, shows a symmetric distribution. The data of the fine mesh shows agreement with the potential flow, but the pressure of the coarse mesh shows a totally different trend. This confirms the need for a very fine mesh to avoid any numerical viscosity and hence to approximate the inviscid potential flow.

$$C_p = \frac{p - p_\infty}{\frac{1}{2}\rho V_\infty^2} \tag{5.4}$$

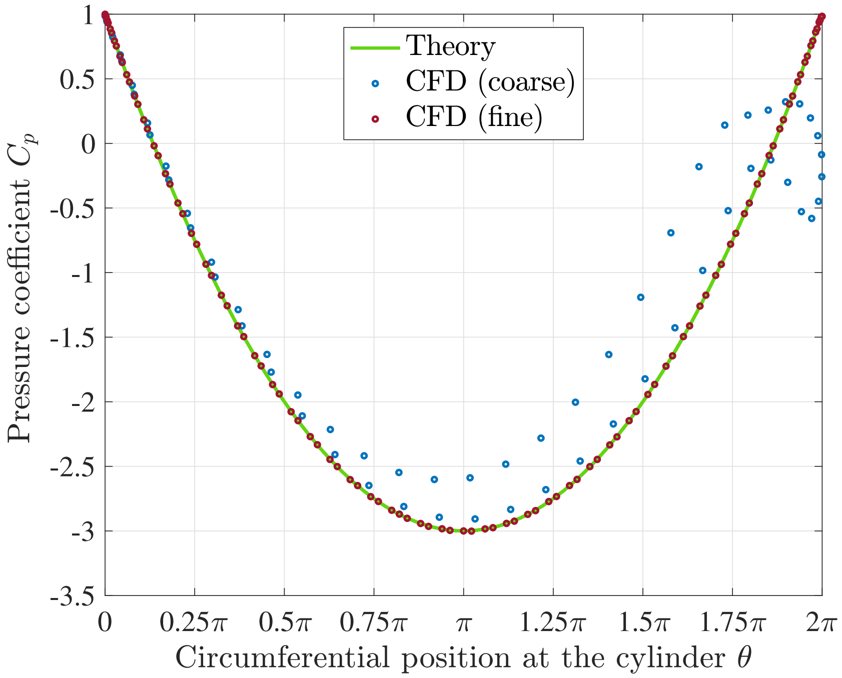

Figure 5.4: C_p distribution around the cylinder for both the potential flow and CFD approach

5.3.2. Flow Around an Airfoil

For the pressure distribution over the cylinder, an analytical expression exists, but for the airfoil (panel) method, numerical methods are needed. Hence such method is needed to define the accuracy of the CFD simulation. To check the influence of numerical viscosity on the simulation of an airfoil, the same approach is taken as for the cylinder. The airfoil analyzed is the NACA 0012 at $\alpha = 2°$. In Figure 5.5, the analysis of the coarse mesh is shown, while the results of the finer mesh are presented in Figure 5.6. The coarse mesh resulted in 40 control points at the airfoil surface. This is a low number, but it clearly shows the effect of the numerical viscosity. Similarly to the cylinder, the analysis of the coarse mesh had difficulties in converging to the steady state solution. The flow results show the viscous dissipation along the airfoil surface and a large wake is formed, see Figure 5.5b. This wake is not present in the potential flow solution and hence the grid should be refined to get a better similarity between the two methods.

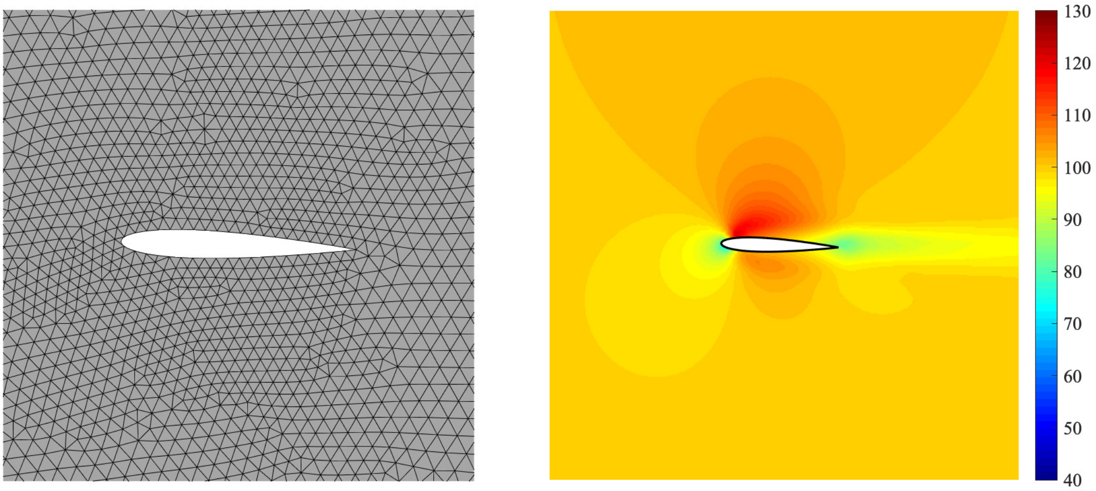

(a) Coarse airfoil mesh

(b) Flow field of absolute velocity

Figure 5.5: Euler analysis of flow around airfoil using a coarse mesh

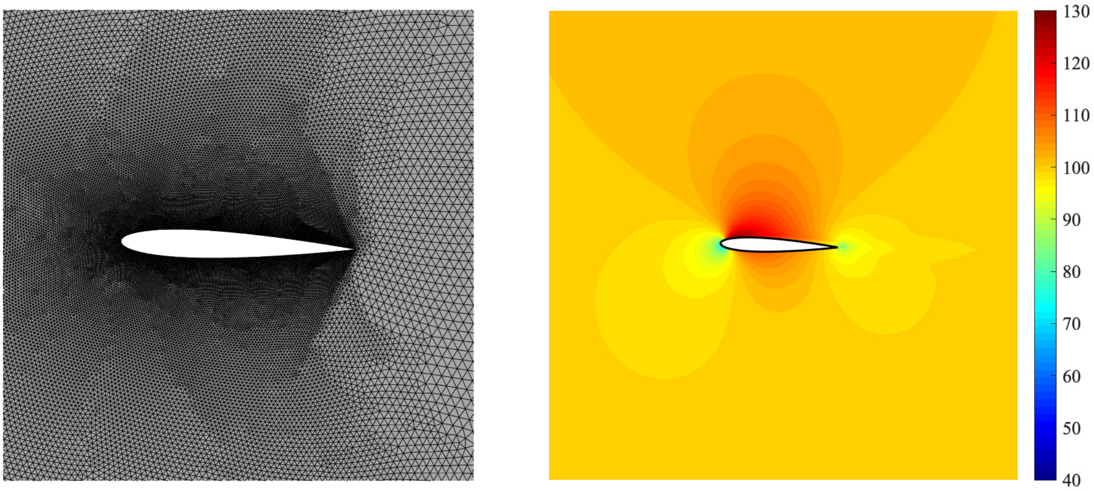

(a) Fine airfoil mesh

(b) Flow field of absolute velocity

Figure 5.6: Euler analysis of flow around airfoil using a fine mesh

The wake has almost disappeared once a finer mesh is used for the analysis, see Figure 5.6, confirming the reduction in numerical viscosity. The refined mesh resulted in around 2000 control points around the airfoil surface. For simplicity reasons, these analyses were done using a triangular and hence unstructured grid. The refined mesh comes with an increase in computational time, but did show acceptable convergence to a steady state solution. To see if the CFD analysis approximates the potential flow results, a comparison with an existing potential flow method was performed. The flow field is still not completely wake free, but the error of the lift value compared to the potential flow solution is less than 0.1%. The pressure distribution around the airfoil using the coarse and fine mesh is shown in Figure 5.7. The C_p distribution from the CFD simulations is compared to the results coming from a 2D linear varying vortex panel method, named XFOIL [42]. This method was set to the inviscid solver option, to obtain the potential flow results. As can be seen, the pressure distribution of the fine mesh shows good agreement and it can therefore be concluded that the potential flow can be modeled using CFD simulations.

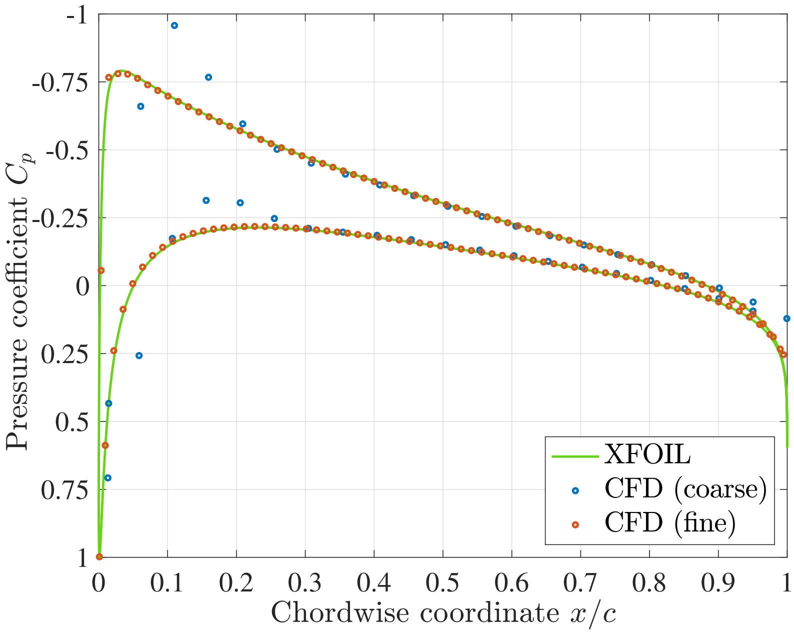

Figure 5.7: Pressure distributions of the NACA 0012 airfoil at $\alpha = 2°$ using different methods

5.3.3. Propeller Slipstream

For the propeller slipstream modeling, the inflow velocity on the jet inlet plane was set to V_j. So it is modeled that the jet enters the domain perfectly horizontal. Numerical viscosity can have a large influence on the jet, since an instantaneous jump in velocity is present. This instantaneous jump means an infinitely large gradient and hence the boundary of the jet will be smoothed and spread out [36]. The amount of smoothing and spreading is a function of the grid size. The influence of the mesh size on the jet boundary is shown in Figure 5.8. The results of the analysis using the coarse mesh at the boundaries are shown in Figure 5.8a. The jet is modeled to have a height which is a tenth of the domain size and there is no object in the domain. The shear layer between the jet and the freestream shows large mixing of the flow and this layer even reduces the effective velocity in the middle of the jet. However, in Figure 5.8b, the results for a finer mesh simulation are shown and compared to the coarse mesh, the shear layers are very small and only a marginal increase in thickness is observed throughout the domain.

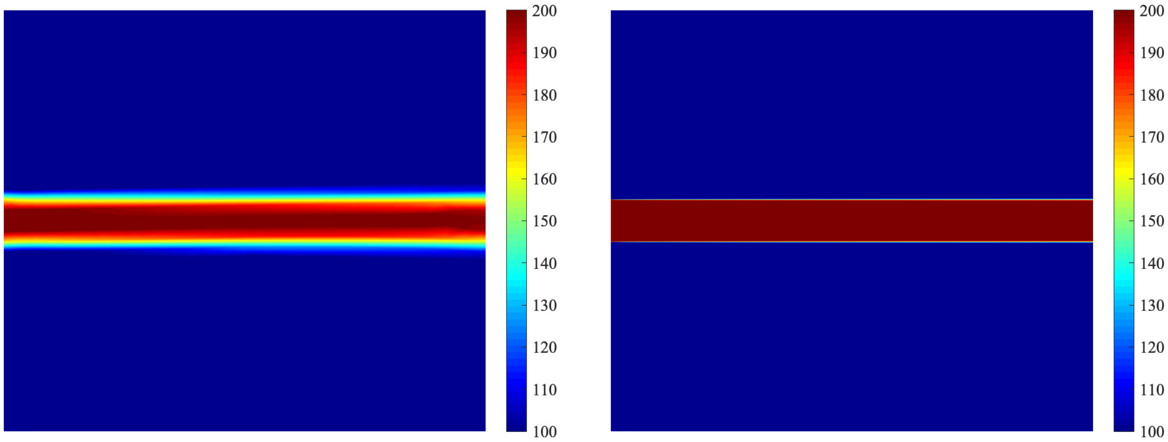

(a) Flow field using a coarse mesh

(b) Flow field using a fine mesh

Figure 5.8: Difference in slipstream development depending on the jet mesh size

The domain for the two is exactly the same and the comparison emphasizes the size of the shear layer in the case of a coarse mesh and it is clear that this would have an even larger effect on the jet development when the jet height is smaller. If an airfoil is present close to the boundaries, the influence of the jet on it is greatly affected and incorrect results are obtained since the local velocity would be different than the theoretical value of V_j. The effect of the numerical viscosity on the velocity profile can be seen in Figure 5.9.

For the coarse mesh, the momentum is diffused resulting in a parabolic velocity profile while for the finer mesh, the axial velocity is more or less constant throughout the jet and the velocity jump is preserved. For this type of simulations, a structured grid would be preferred. However, in the case where an airfoil is present in the computational domain, the jet will exhibit some small perturbations and hence a structured grid can worsen the numerical viscosity effects. The option to use CFX with free slip walls and a very low viscosity gave similar results to the analysis using the inviscid option of Fluent. However, the simulations for the jet in Fluent were not reaching the steady-state convergence criteria and the flow field showed a wavy pattern at the jet boundary. This is due to the numerical viscosity at the boundary and the fact that the solver was set to the inviscid option. The inviscid model has problems converging when large velocity jumps are present. Therefore, it was decided to use CFX for all the validation simulations.

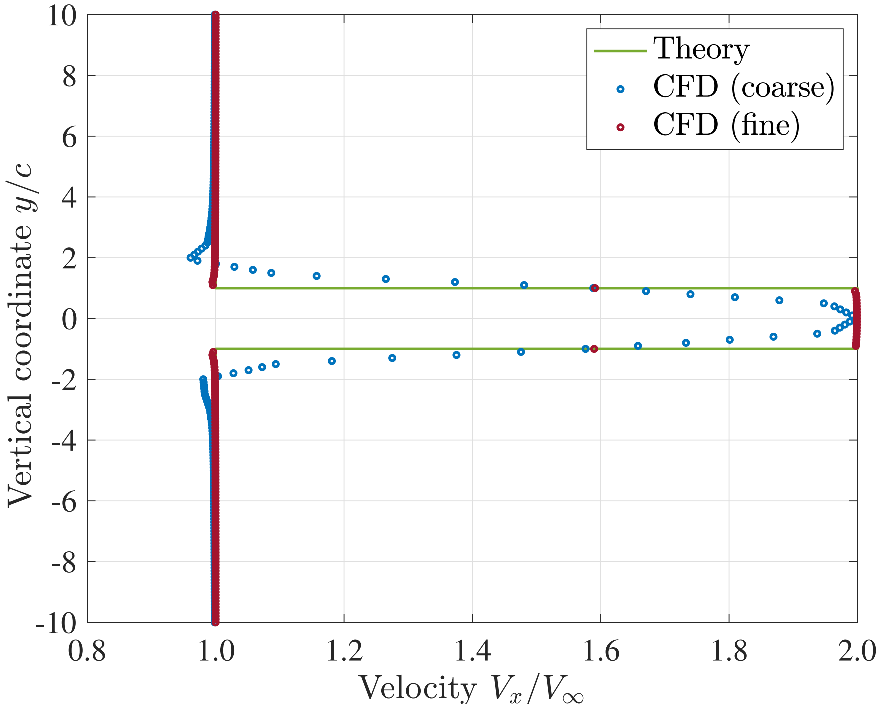

Figure 5.9: $V_x(y)$ distribution of the jet at the outlet for both the potential flow and the CFD approach

5.4. Grid Convergence

To prevent unwanted numerical viscosity influencing the result of the simulation, the mesh must be very fine close to the airfoil, but also throughout the jet region. The grid used was generated using ANSYS ICEM CFD and consists of an unstructured triangular mesh. In the end, no inflation layer was used for the airfoil but the maximum mesh size on the surface was set to a very small value. For the jet refinement, a density region from inlet to outlet was defined, with a constant height of $10c$ for all the simulations. This ensures that the number of cells is consistent for all different slipstream heights. The convergence criteria for the steady-state solution was set to 10^{-6}.

The solver was set the high resolution advection scheme, which means that the specific blend factor is chosen using a special nonlinear recipe [43]. This results in a second order accuracy of the equations. A grid dependency study was performed to investigate the discretization error and the grid was refined in a systematic manner, resulting in six different grids. The properties of the different meshes are presented in Table 5.1. Note that the given grid sizes were normalized with the chord length. h_i is the average grid size of grid i and h_1 is the average grid size of the finest grid [44, 45]. Richardson extrapolation of the lift coefficient on the different grids was performed by means of a weighted least-squares approach to determine the observed order of convergence (p). The weights were added, such that refined meshes have more value and they are determined by the typical cell size [46]. The results of the grid convergence study can be seen in Figure 5.10. The observed convergence rate ($p = 1.9771$) is slightly lower than the theoretical value, but is close to it, confirming the correctness of mesh refinement.

Table 5.1: Properties of the different grids used in the convergence study

grid	airfoil grid size	number of cells	h_i/h_1	C_l	weight	ϵ [%]
6	0.1	63428	9.62	0.201	0.045	16.02
5	0.05	75807	8.05	0.216	0.054	9.67
4	0.01	135578	4.50	0.231	0.097	3.40
3	0.005	173894	3.51	0.234	0.124	2.19
2	0.001	346501	1.76	0.238	0.247	0.56
1	0.0005	610149	1	0.239	0.434	0.27

Using the Richardson extrapolation of the lift coefficient values, the solution of a grid with infinitesimal cells can be determined ($h_i/h_1 = 0$). This theoretical grid produces the exact solution and the C_l was calculated to be 0.2393. In Table 5.1, the discretization error (ϵ_h) of each grid with respect to this theoretical exact solution is given. As can be seen, the discretization error of grid 1 and 2 is less than 1%. In the end, grid 2 was chosen to be used in the validation simulations since it is the best compromise between accuracy and computational cost.

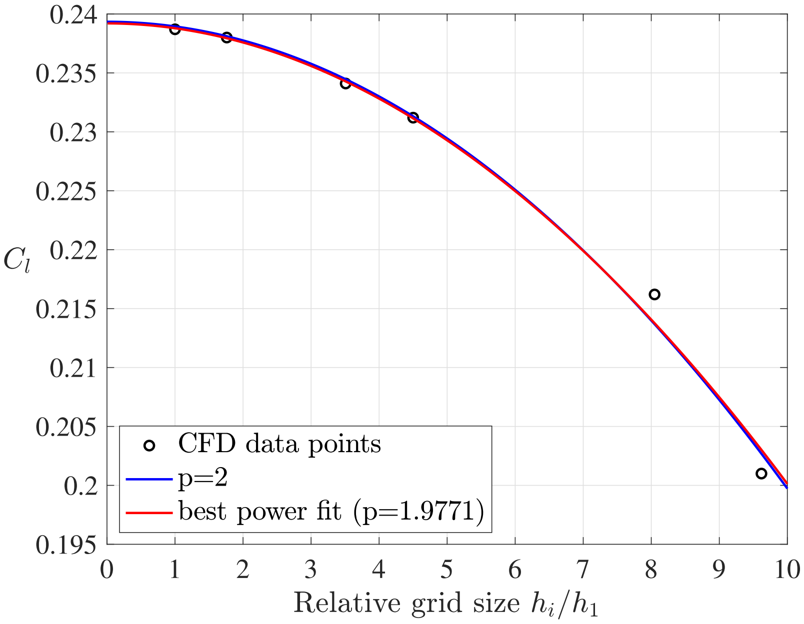

Figure 5.10: Grid convergence of C_l

So to conclude, the modeling of potential flow using a numerical solver imposes numerous problems such as the influence of the boundaries and the creation of numerical viscosity. The grid size must be very small and this means that the computational time of the CFD simulations is substantial, in the order of hours on a personal computer. Next to the computational time of the solver, the generation of the mesh, which has a large number of cells, also takes up to an hour. Now the setup of the 2D CFD analysis is defined, the actual results of the simulations can be discussed, which is done in Chapter 6. The results of the CFD simulations are then compared to that of the 2D potential flow model, defined in Chapter 4.

6

Results of the 2D Airfoil Analysis

This chapter discusses the results of the 2D analysis of the airfoil submerged in a jet of finite height. The proximity of the slipstream boundaries will lower the sectional lift as compared to the case of an infinitely high jet. Firstly, the analysis data of the 2D potential flow numerical tool, which accounts for the finite slipstream height, will be discussed in Section 6.1. After that, a parametric study of the numerical tool's inputs is presented in Section 6.2. Secondly, the data of the CFD simulations is discussed and is used to validate the potential flow tool. In Section 6.3 the results of the CFD analysis are presented, while the limitations of the CFD simulations are discussed in Section 6.4.

6.1. Potential Flow Analysis Results

Firstly, the results of the 2D potential flow numerical method are presented. The calculated data is compared to the results given by Ting [34], such that the analysis tool can be verified and that possible discrepancies can be determined for the use of a different integration methods, as discussed in Section 4.3.3 and Appendix A. The case that was analyzed is that of a symmetric thin airfoil, located in the middle of the jet. The data presented by Ting were based on two different jet velocity ratios, namely $V_j = 2V_\infty$ and $V_j = 1.5V_\infty$. Therefore, the same values were used to generate the data of the numerical tool. The local sectional lift can be calculated by using Equation 6.1, where the circulation is the outcome of the numerical method.

$$l_j = {}^1\!/_2\rho_\infty V_j^2 C_{l_j} = \rho_\infty V_j \int_0^c \gamma(x)dx \tag{6.1}$$

The local lift of an airfoil submerged in a jet with finite height will be lower than the lift value of an airfoil with an infinitely high jet up front, due to the influence of the jet boundaries. The sectional lift can be compared to the lift of an airfoil without jet using the lift correction factor, see Equation 3.12. As discussed in Section 3.4, K_l is a function of the velocity ratio, ranging between 1 and V_j^2/V_∞ for an infinitesimal and infinitely large slipstream respectively. For the case of an infinitely high jet, the local lift coefficient will be equal to the case of no jet, meaning $C_{l_j} = C_{l_\infty}$. By non-dimensionalizing the lower sectional lift for an finite slipstream height using V_j, there will be a reduction of C_{l_j}, as was discussed in Section 4.3.3. The reduction in local lift coefficient can be seen as a correction of C_{l_∞} , which is based on the slipstream height. This is correction factor is presented by the ratio K_{C_l}, see Equation 4.28. K_{C_l} will range from V_∞^2/V_j^2 to unity and hence the lower bound is now dependent on the velocity ratio.

An airfoil with no camber and chord c is evaluated at a small angle of attack (α=2°), in a jet of height h. The airfoil was discretized with 200 control points along the camber line. The points were distributed using a half cosine spacing, which is usually done so the LE and TE are better resolved [11]. For the Fourier coefficients and the number of image sets, a total number of 5 and 10 was used respectively. These proved to be an appropriate number for obtaining a converged solution and at the same time having low computational cost as was discussed in Section 4.4. The data are shown in figure 6.1. The data points computed with the numerical method (Equation 4.27) are presented by the solid lines and the results from Ting are presented by the circle markers [34].

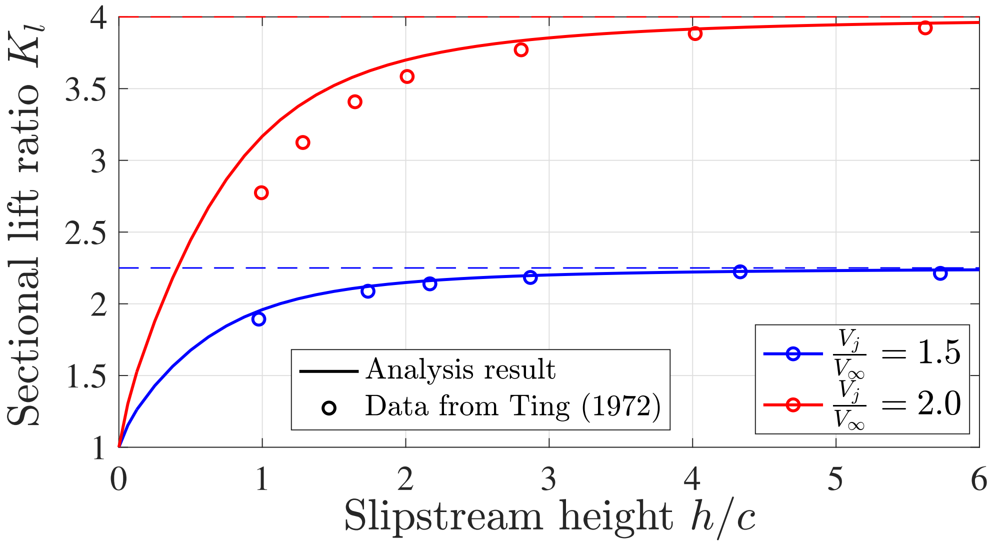

Figure 6.1: Comparison between data presented in literature [10, 34] and calculated data using the numerical method presented in Chapter 4

As can be seen, the sectional lift of the airfoil is almost not influenced by the slipstream height from $h/c = 5$ on. However, for smaller values of h/c, the lift is lowered significantly compared to the theoretical value for an infinite slipstream height. When the h/c value approaches 0, the slipstream disappears and the value of the lift goes towards the value of the uniform case. The reduction in lift at small slipstream heights is similar to that found in the NASA SECPTOR research discussed [33], see Figure 3.9. Unfortunately, the calculated data points do not overlap with the presented data points from the paper [34]. The discrepancy is in particular large at small h/c-values, which is the domain where the lift ratio is heavily influenced by the slipstream height. Part of these differences originates probably from the wrong use of the evaluated contour integrals by the author [10]. Furthermore, Ting presents two equations which should provide the fit for his data points. However, the resulting lines of these equations do not end up on his own given data points [34], which is another mistake made. A different study performed previously [31], confirmed the incorrectness of the presented data and also observed a small increase of the lift correction factor compared to the given data by Ting, similarly to the analysis results presented in this thesis.

6.2. Variation of Input Parameters

The numerical method should, in theory, work for all the different thin airfoils and jet combinations. To check the consistency of the analysis results, the inputs of the tool were varied. The jet velocity to freestream velocity ratio is an important parameter, since this will determine the lift augmentation in the first place. The three main (geometrical) inputs next to the slipstream height are the geometry of the airfoil itself, the vertical position of the airfoil within the jet and the angle of attack. The variation of these four inputs is discussed in this section. The influence of the velocity ratio is discussed in Section 6.2.1, while the geometrical input variations are discussed in Sections 6.2.2, 6.2.3 and 6.2.4 for the airfoil camber, angle of attack and vertical position respectively.

6.2.1. Variation of Velocity Ratio

To further investigate the influence of the slipstream height on the lift augmentation, more velocity ratios are investigated and they are compared using K_{C_l}, which is shown in Figure 6.2. By using the lift coefficient ratio, which has an upper limit of 1, the impact of the velocity ratio on the sensitivity of the decrease in lift due to the finiteness of the slipstream height is emphasized. In the figure, also the lower bound values are presented in the case where the slipstream height becomes infinitely small. As can be seen at low values of h/c, the velocity ratio is an important factor for the determination of the actual lift. For a fixed slipstream height, the lift increase due to the jet is less effective for larger velocity jumps. For small distributed propellers, this could mean that it can be more advantageous to use a slightly larger diameter with lower disk loading than more smaller propellers with higher disk loading.

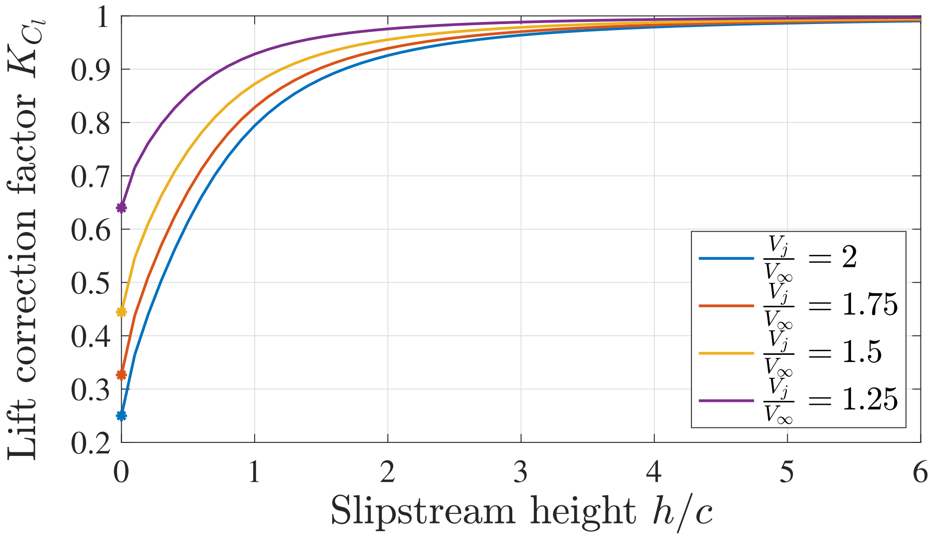

Figure 6.2: Sectional lift coefficient correction factor for different velocity ratios as function of slipstream height

6.2.2. Variation of Camber

In the previously performed analyses, a symmetric thin airfoil was chosen. For simplicity, this will be referred to as the NACA 0012, although the thickness is not taken into account. By using the NACA airfoil series, the camber can be simply varied. In Figure 6.3, the analysis results of cambered airfoils are shown and compared to that of the symmetric one. The analyses of the different NACA airfoils were performed at the same α. Furthermore, $V_j = 2V_\infty$ was used for the velocity ratio.

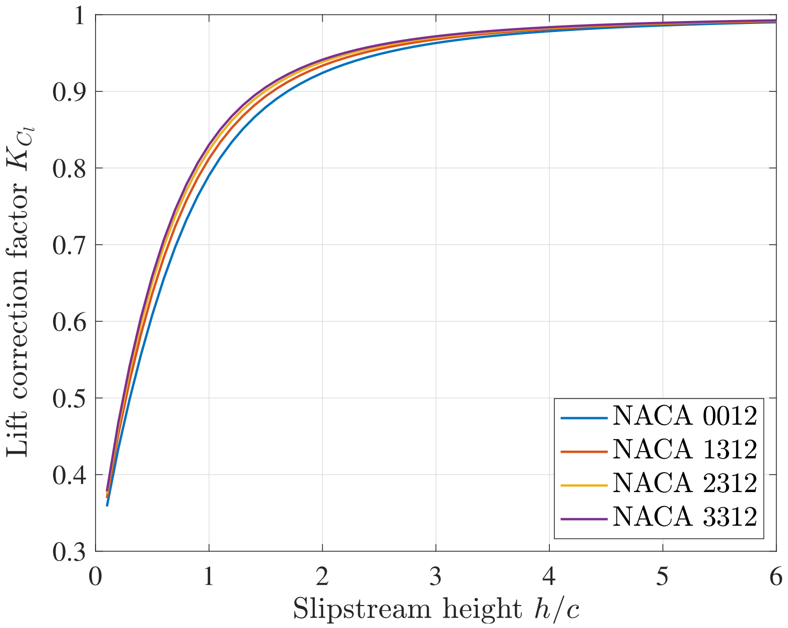

Figure 6.3: Lift correction factor for different cambered airfoils at $\alpha = 2°$

As can be seen, the correction factor is not the same for airfoils with different camber and this is due to the thin airfoil approach taken. The correction factor at a specific slipstream height can also be assigned to the lift curve slope. The change in C_{l_α} for the cambered airfoils turned out to be equal to the symmetric airfoil. However, the resulting new circulation distribution, due to the successive images, results also in a different zero lift angle (α_{0_L}) for the 'new' cambered airfoil. This new airfoil refers to an airfoil that theoretically would have the same lift coefficient without jet as that of the airfoil submerged in the jet. To calculate the C_{l_j} using the original α_{0_L}, the correction factor (f_{cam}) is slightly larger than f_{sym}, since the new α_{0_L} is slightly more negative. This is presented by Equation 6.3, where the original zero lift angle is used. The change of α_{0_L} is different for varying slipstream heights. Furthermore, since the correction factor f_{cam} in Equation 6.3 applies to the whole term inside the curly brackets, the value of f_{cam} differs with varying α.

$$c_{l_{sym,jet}} = f_{sym} \cdot c_{l_\alpha} \cdot \alpha \qquad (6.2) \qquad\qquad c_{l_{cam,jet}} = f_{cam} \cdot c_{l_\alpha} \cdot \{\alpha - \alpha_{0_L}\} \qquad (6.3)$$

In Figure 6.4, different $C_l - \alpha$ curves are shown for the NACA 2312 for different slipstream heights. Indeed it can be seen that, since for each slipstream height the correction factor differs, the C_{l_α} is changed with respect to the infinite slipstream case. The change in lift curve slope and α_{0_L} was also observed by Ting [34]. The change in slope at a specific h/c is equal to the K_{C_l} correction value of the symmetric airfoil in Figure 6.3 at the same h/c. At each slipstream height, indeed the change in α_{0_L} is different. For the symmetric airfoil, the correction factor is independent of α, as can be seen in the next section

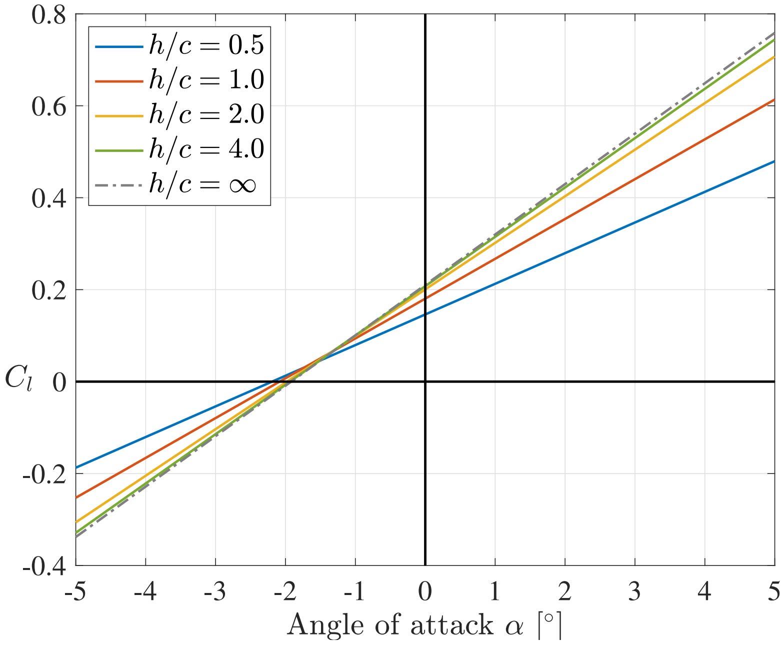

Figure 6.4: $C_l - \alpha$ curves for the NACA 2312 at different h/c

6.2.3. Variation of Angle of Attack

As is discussed in the previous section, varying the camber results in a slightly different K_{C_l} and this variation is also dependent on the angle of attack. This is because the correction factor for cambered airfoils is applied both on α and α_{0_L} and hence the difference is biggest for $\alpha \approx \alpha_{0_L}$. Figure 6.4 can also be presented in the usual $h/c - K_{C_l}$ manner, as can be seen in Figure 6.5. On first glance, it looks like the line of $\alpha = -2°$ is very off compared to the rest. This is due to the change of α_{0_L}, which was shown in Figure 6.4, where the lines all have different intersection points with the x-axis.

The α_{0_L} of the NACA 2312 is close to the $-2°$ and hence close to this angle, the 'new' airfoil will generate a small amount of lift. Hence the term in the curly brackets in Equation 6.3 is small and the correction factors are either small or very large. Since the absolute amount of lift is small in these cases, the effect of this asymptotic behaviour in for example 3D sectional analysis is also small. When α is large compared to the α_{0_L}, the influence of the shift in the latter on the f_{cam} gets small and the value convergence towards the f_{sym}. For the symmetric airfoil, there is no dependency on α and this is presented by the black dashed line.

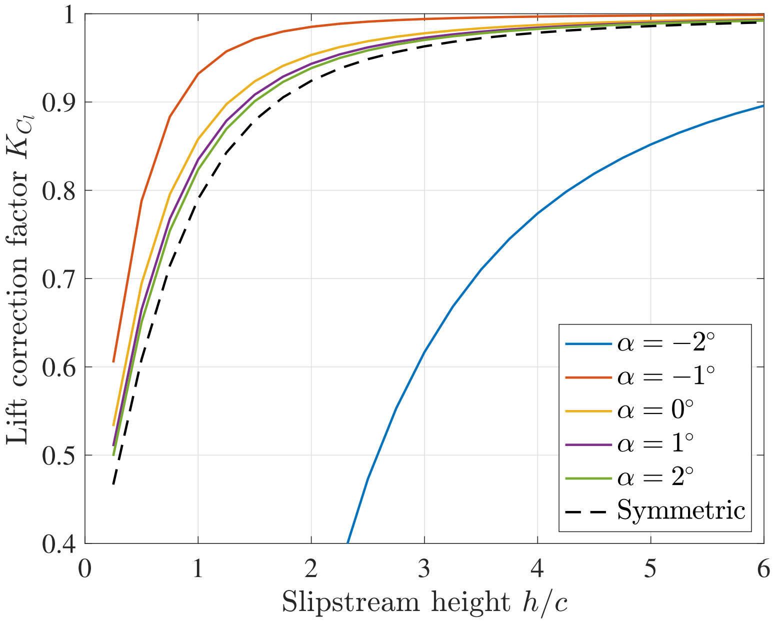

Figure 6.5: $K_{C_l} - h/c$ curves for different α using the NACA 2312

6.2.4. Variation of Vertical Airfoil Position

For all the previously discussed cases, it was assumed that the airfoil is located in the center of the jet, where $a = b = h/2$. However, the lift augmentation changes when the airfoil is shifted up or down in the middle domain. The change of vertical position and the effect on K_{C_l} is shown in Figure 6.6. This was done using a symmetric airfoil and $V_j = 2V_\infty$. When the airfoil is closer to the boundaries, the distance to one of the images gets smaller and since the influence follows a rational function, the lowest combined value is in the middle of the two functions. This means the induced downwash is larger towards the boundaries and hence the K_{C_l} gets smaller. The slipstream height influences the rate of change, following the same principle. The further away the two singularities are, the flatter the middle region and the steeper the edges of the combined influence.

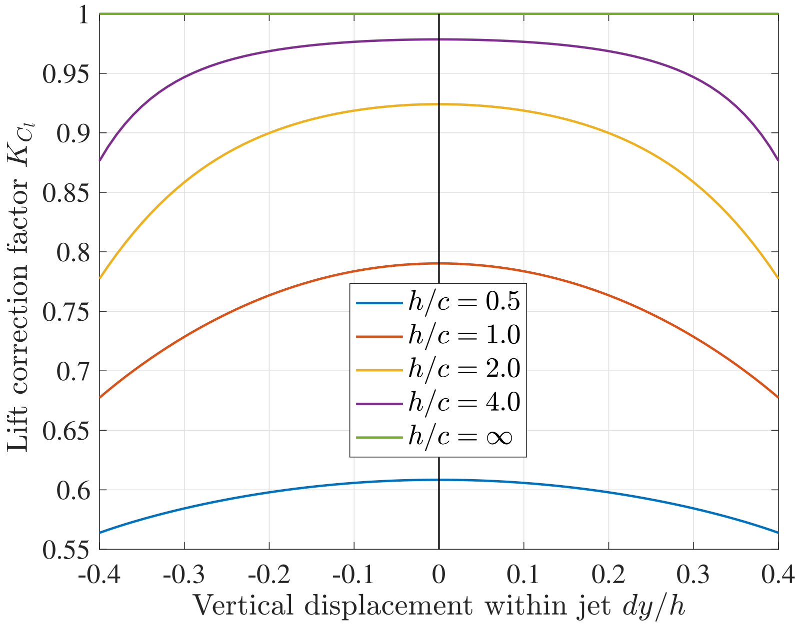

Figure 6.6: K_{C_l} variation as function of vertical airfoil position for the NACA 0012

As can be seen, the results are independent of the direction of displacement. So displacing the airfoil down has the same effect as shifting it up and this is due to the potential flow approach taken. This is also true for the cambered airfoil, since the thin airfoil theory assumes small angles and hence the boundary condition of no normal velocity is placed from the camber line to the chord line [30]. As shown in Figure 4.6, the effect of the upper and lower images are equal when the airfoil is located in the middle, since the strength and direction of the images are equal to each other. The induced velocity vectors of both images are both pointing downwards and the axial components are canceled. Shifting the airfoil will increase one vector, while the other is decreased. Since they are both pointing downwards, the displacement direction only influences the resultant axial component, which does not result in a difference in lift. The numerical method does not converge for the case where the airfoil is located precisely at one of the boundaries, since the induced velocities of the images will be infinitely large.

6.3. Two-Dimensional CFD Data

In this section, the results of the 2D CFD simulations are presented. To validate the potential flow tool as described in Chapter 4, the CFD data is compared with its results in Section 6.3.1. To further analyze the effect of the finite slipstream height on the airfoil lift, the pressure distribution over the airfoil for different slipstream heights is discussed in Section 6.3.2. Finally, an investigation in the observed circulation in the CFD simulations is presented in Section 6.3.3, where also the validity of the KJ theorem is discussed.

6.3.1. Validation of Numerical Tool

The CFD simulations were performed for the same configurations as discussed for the analysis tool. So the used airfoil is NACA 0012 at an angle of attack of 2°. Furthermore, the airfoil is located in the middle of the jet, defined from the inlet plane of the domain. The data points are shown again for the case of the airfoil being in the middle of the jet and having $V_j = 1.5V_\infty$ and $V_j = 2V_\infty$. For an infinite slipstream, the lift ratio would be equal to the velocity ratio squared and hence the value would be 2.25 and 4 respectively. The data presented by Ting are also shown in the figure. The lift value of the 2D airfoil in the case of the CFD simulation is calculated by extracting the pressure distribution around the airfoil. After the pressure is known, the lift was determined by integrating the pressure in the chordwise direction.

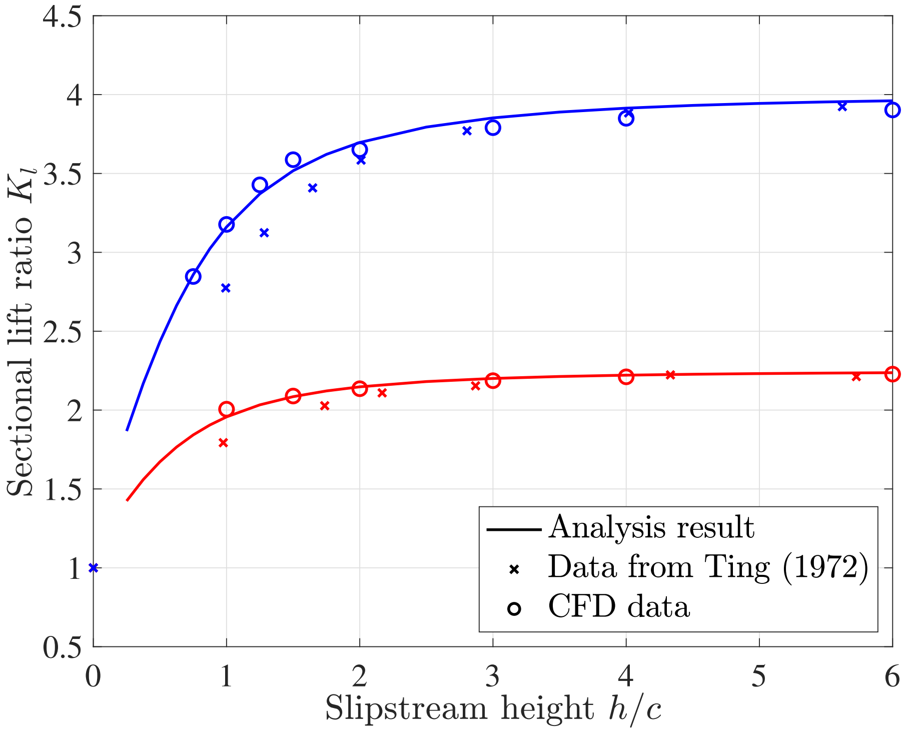

Figure 6.7: Lift ratio at different slipstream heights for two different V_j values

The CFD data shows reasonable agreement with the data obtained from the numerical analysis and seems to confirm a right implementation of the mathematical method of successive reflections. The changed sectional C_{l_α} can be used in the lifting-line method. This correction is shown in Equation 6.2, where f_{sym} is the correction factor for the symmetric airfoil. The discussion of the implementation of this correction value in the LL is presented in Chapter 7. Furthermore, it confirms the incorrectness of the used contour integrals by Ting [34], since the influence of the finite slipstream height seems to be over-predicted for small slipstream height. Unfortunately, not the whole range of slipstream heights could be simulated accurately using CFD. One of the reasons was the number of cells and the required refinement for the very small slipstreams. Other problems encountered during the simulations of small slipstreams were similar in nature as the limitations of the potential flow method as discussed in Section 4.5.

6.3.2. Pressure Distribution over the Airfoil

To further investigate the influence of the slipstream boundary on the airfoil lift, the pressure distribution over the airfoil from the CFD simulations is shown for different slipstream heights. The presented data in this section is from the simulations of $V_j = 2V_\infty$. The pressure coefficient is used as non-dimensionalized coefficient, see Equation 5.3. For the pressure distribution of the airfoil without jet, V_∞ is used while for the airfoils submerged in a jet, V_j is used. The C_p distribution of an airfoil in an infinitely high jet should be equal to that of the airfoil without jet. The pressure distribution of an airfoil with jet is compared to that of an airfoil without jet, referred to as the freestream airfoil. In Figure 6.8a and 6.8b, the C_p is shown for $h/c = 4$ and $h/c = 2$ respectively.

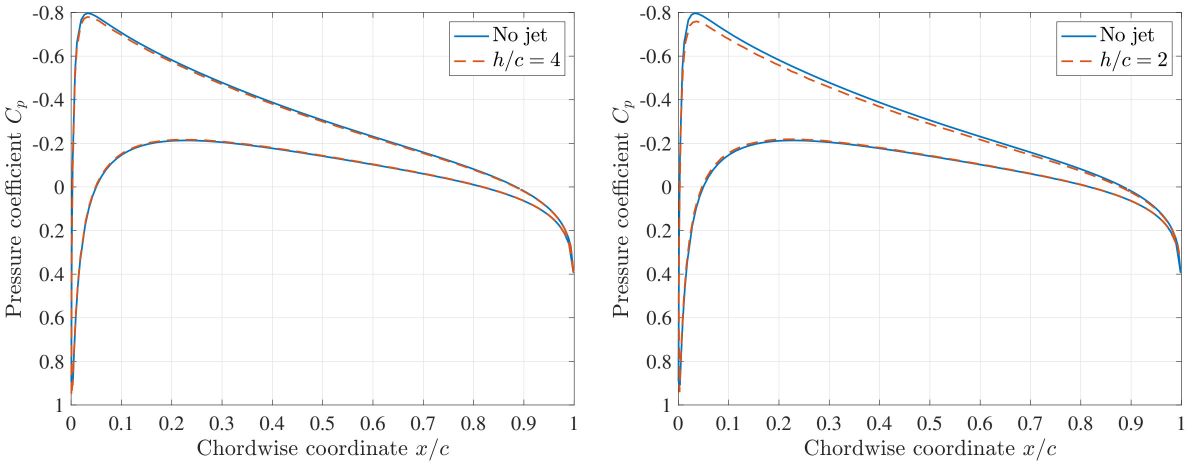

(a) $h/c = 4$ (b) $h/c = 2$

Figure 6.8: Comparison of the pressure distribution of the NACA 0012 without jet and the airfoil submerged in a jet of finite height

The pressure distribution for $h/c = 4$, shows almost complete agreement with the freestream airfoil. This is as expected, since the influence of the slipstream boundaries is small for this slipstream height. For the simulation with $h/c = 2$, the decrease in sectional lift becomes more apparent, since the pressure distributions are less overlapping. It seems that most of the lift reduction is achieved on the upper side of the airfoil. This is due to the fact that the suction peak at the LE is reduced due to the influence of the boundaries.

In Figure 6.9, more results are shown for even smaller slipstream heights. The two slipstream heights presented are that of $h/c = 1$ and $h/c = 0.5$ in Figure 6.9a and 6.9b respectively. The reduction in sectional lift is even more distinctive as is expected for these smaller slipstreams. The simulation of $h/c = 1$ shows that also the relative velocity on the lower side is reduced, increasing the pressure. However, the distributions still look similar in shape and no significant change in chordwise position of the center of pressure is observed. For the smallest slipstream height analyzed, the suction peak is reduced significantly compared to the freestream airfoil and also the pressure on the lower side shows a large discrepancy compared to the freestream airfoil.

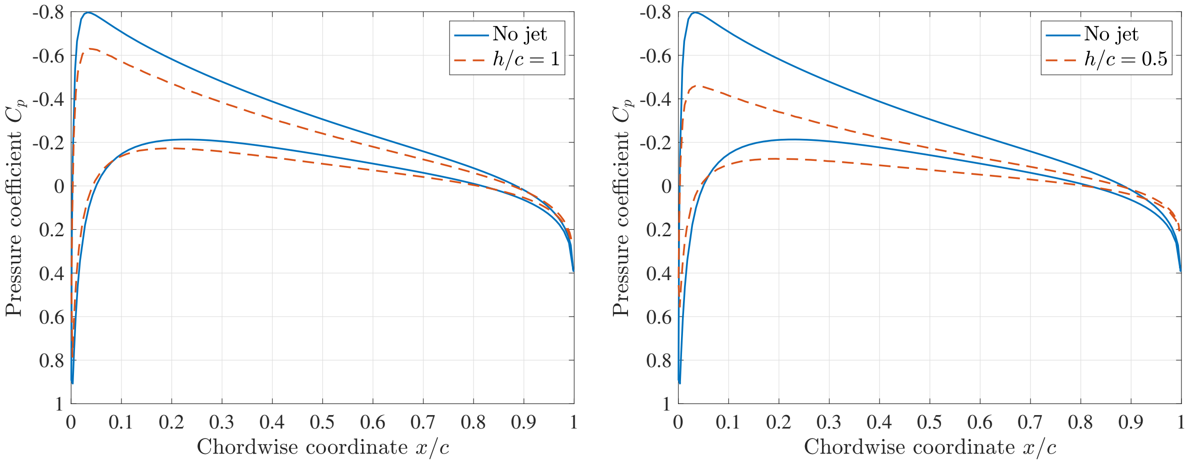

(a) $h/c = 1$ (b) $h/c = 0.5$

Figure 6.9: Comparison of the pressure distribution of the NACA 0012 without jet and the airfoil submerged in a jet of finite height

The effect of the proximity of the slipstream boundaries results in an increase in pressure on both sides of the airfoil. This can be thought of as a reduction of effective velocity due to the finite slipstream height. This is similar to the interpretation of the velocity scaling factor β in the NASA SCEPTOR research [32, 33]. The author mentioned that the influence of the finite slipstream on the airfoil lift, effectively can be modeled by a reduction in jet velocity. The larger the pressure peak, the larger the effect of the finite slipstream height and hence the effect of the slipstream boundary is greatest on the upper side of the airfoil. The suction peak is lowered and this is the main contribution of the reduction in lift. This reduction of sectional lift is therefore similar to the modeled effect of the images, which reduces the required circulation to satisfy the boundary conditions at the chord line.

6.3.3. Circulation Calculation of the Airfoil

The calculated output of the 2D potential flow tool is the sectional circulation and not the sectional lift. Similarly in 3D, the output of the LL and VLM techniques is the circulation distribution of all wing segments. To calculate the actual sectional lift in these vortex based tools, the KJ theorem is used, see Equation 3.8. Normally, V_∞ is used in this calculation, but when the jet is present, the local velocity should be used instead. However, previous studies contradicted the use of the local velocity to calculate the sectional lift, since they deemed the use of V_j nonphysical, as discussed in Section 3.3, and mentioned that V_∞ should always be used instead [6, 7]. The question arises if the KJ formulation is still valid for the case of non-uniform inflow. The main reasoning behind the choice for V_∞ instead of V_j was based on the fact that the observed lift distribution was largely over-predicted, even after applying the SRF.

To check the correctness of the KJ theorem for a non-uniform inflow field, the circulation around the airfoil in the 2D CFD simulations is determined. The circulation in a 2D plane can be determined by taking the line integral along a closed contour, see Equation 3.7. This is done with the velocity field from the CFD simulations and circular contours were defined. The lines were defined by taking at least 1000 control points along the circle and the velocity data were interpolated to get the values at these contour control points. To determine the circulation value at multiple radial distances from the airfoil, numerous contours were defined in the domain. Depending on the radius of the contour, the number of control points was increased, such that the same relative distance between two control points was maintained. This process for circular lines is shown in Figure 6.10. A total number of 400 contours was defined in the computational domain, each with an increase in diameter of $0.1c$.

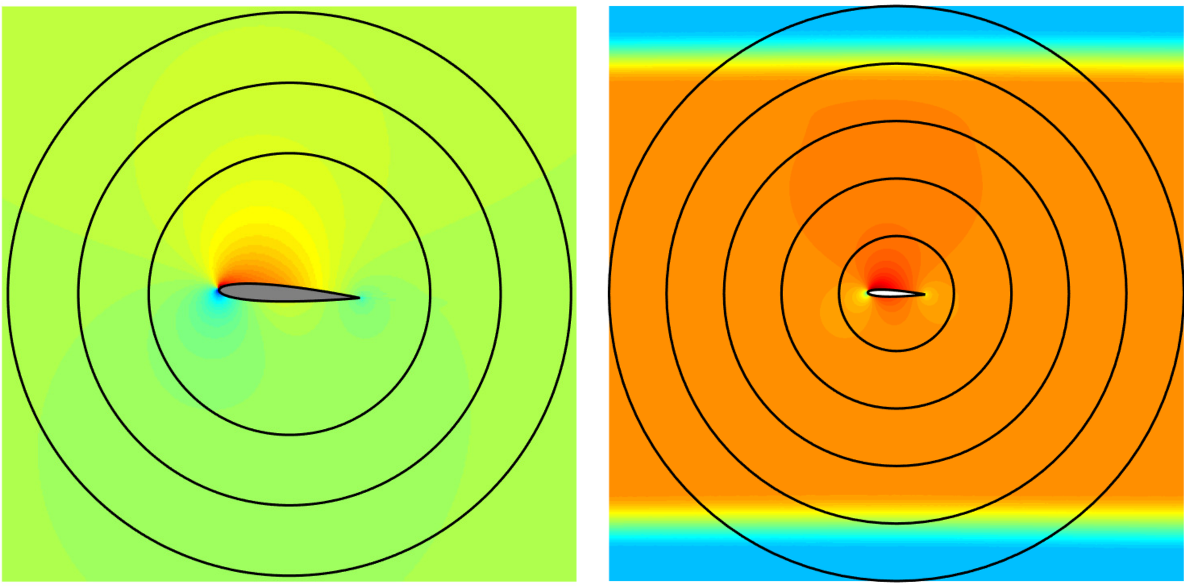

(a) Velocity flow field without jet

(b) Velocity flow field including jet using $V_j = 2V_\infty$

Figure 6.10: Visualization of the determination of the circulation in the CFD flow field

Actually, the circulation values for a 2D airfoil in the potential flow theory should be constant independent on the chosen contour, as long as the line does not cross any singularity. This is because there is no viscous dissipation and hence Kelvin's circulation theorem cannot be violated. This theorem states that the change of circulation must be zero [11]. The theoretical value of circulation for the NACA 0012 airfoil, $\alpha = 2°$ without jet is compared to the value from the CFD analysis and this is shown in Figure 6.11a. As is shown, the circulation close to the airfoil is similar to the predicted theoretical value. However, further away from the airfoil, the value of the circulation drops and this is not happening in the potential flow analysis. Unfortunately, the CFD domain is not infinitely large and also not infinitely discretized and hence the proximity of the boundaries together with the generation of numerical viscosity results in the reduction of the circulation further away from the airfoil. The mesh size far away from the airfoil is larger and hence this region is more influenced by numerical viscosity. Close to the airfoil, the circulation observed in the CFD simulations shows good agreement with the theoretical value and this confirms to confirm the correctness of the KJ theorem for the case without jet.

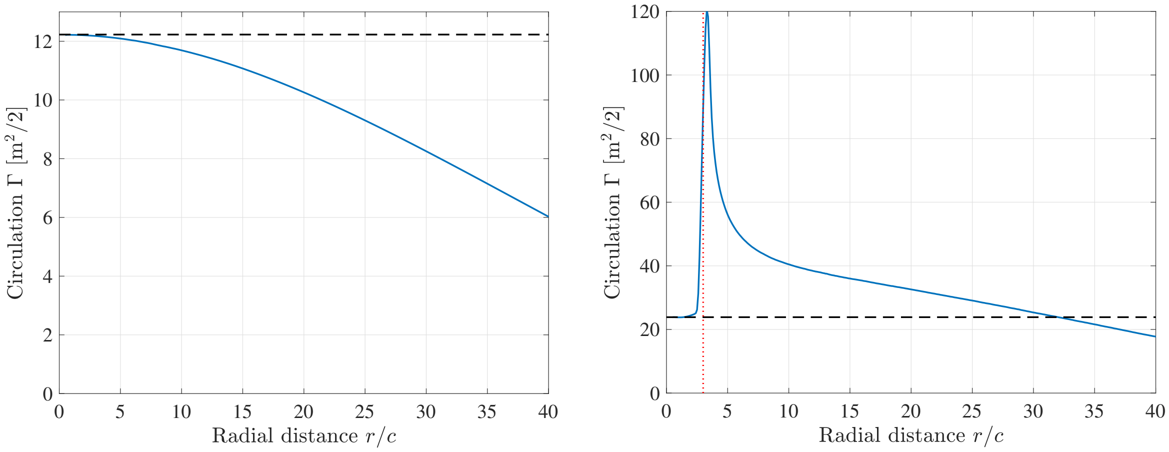

(a) Without jet

(b) Including jet using $V_j = 2V_\infty$

Figure 6.11: Circulation values for the 2D airfoil case as function of the radial distance to the airfoil

Similarly, the circulation can be determined for the 2D CFD analysis of the airfoil submerged in the jet. This was done for the case of $h/c = 4$ and is presented in Figure 6.11b. The circulation close to the airfoil seems reasonable constant but then suddenly, a very large spike is presented. The large peak is due to the vorticity inside the boundary of the jet. This vorticity in combination with a small vertical deflection of the slipstream results in different flow fields at equal vertical distances from the airfoil and the contour exactly passes this region. This can be seen in Figure 6.10b, where the fourth contour gives the large spike. The small upward deflection of the slipstream results in lower velocities at the lower side compared to the upper side. This is, probably, the reason for the large discrepancy at this particular radial location. However, the value of the circulation close to the airfoil seems to be the same as that predicted by the potential flow theory. For the chosen slipstream height, K_{C_l} is close to 1 and hence the circulation for the case of $V_j = 2V_\infty$ results in a circulation two times bigger than the value in the case of no jet. The agreement with the theoretical value confirms the correctness of the KJ theorem, but with the side note that it is only valid for contours that are located completely inside the jet.

6.4. Deflection of the Propeller Slipstream

For slipstreams with a small height, the disturbance of the circulation of the airfoil on the jet boundaries is large since the distance to the airfoil surface is small. Furthermore, when the slipstreams are becoming smaller than the airfoil thickness, the jet will bend around the airfoil and is thickened compared to far upstream. All these problems are due to the fact that the disturbances of the airfoil are no longer small and hence the small perturbation theory can no longer be used. Defining the position of the slipstream on the inlet plane, far away from the airfoil, means that the position of the airfoil in the jet locally is different. This deflection of the slipstream can result in lift values which are far off compared to the potential flow value.

An example of this is visualized in Figure 6.12. This simulation was similar to the ones described above, namely the NACA 0012 at $\alpha = 2°$. The value of the h/c was 0.25 and V_j was twice the freestream velocity. As can be seen, the jet completely deviates from its upstream trajectory and goes over the top of the airfoil. This means that the lower side of the airfoil sees the lower dynamic pressure of the freestream, while the upper side sees the increased dynamic pressure. This blowing like effect results in large lift values, close to the maximum theoretical value of an infinitely large slipstream.

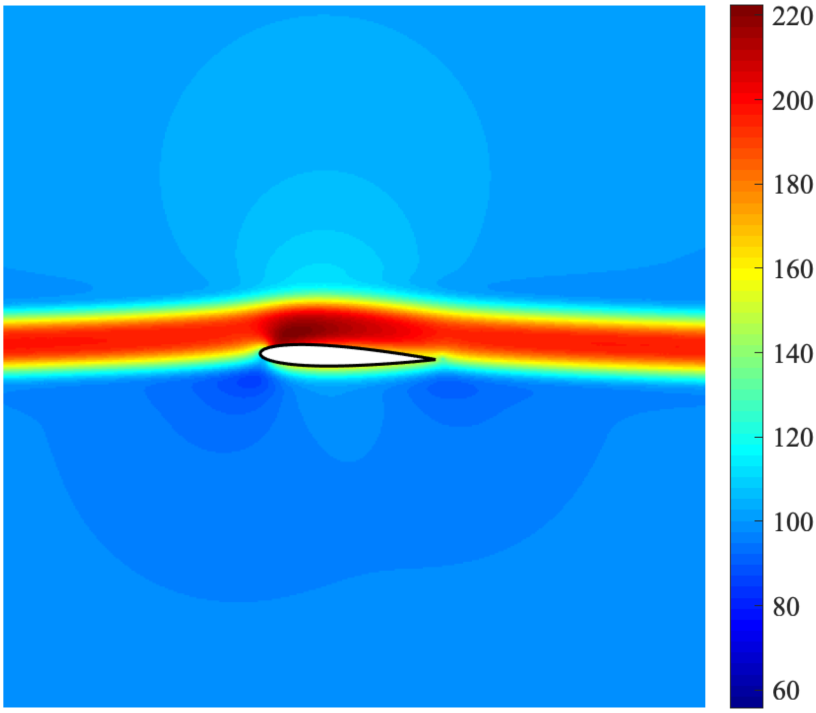

Figure 6.12: Velocity field indicating the slipstream deflection when the slipstream height is small ($h = 0.25c$)

To conclude this chapter: For slipstreams where the height is finite, the lift is reduced compared to the case where the slipstream is infinitely high, and this was modeled using the potential flow approach using consecutive images on either side of the boundaries. This method was validated using CFD simulations in CFX and also confirmed the incorrectness of the given data in the paper of Ting [34]. The reduction in sectional lift is visible in the pressure distribution of the airfoil and the suction peak is lowered significantly for small slipstream heights. The use of the Kutta-Joukowski theorem in a non-uniform inflow field was validated, as long as the chosen contour remains inside the jet. The limitations of the small disturbance theory are confirmed by the simulation of very small jets. Fortunately, the use of the potential flow tool for very small heights converged to the correct theoretical value, as was seen in Section 4.5, and hence can be used to predict these cases, even though they might deviate from the real physical phenomena. In Chapter 7, the 3D LL method is explained in detail in which the 2D correction method is applied to alter the local circulation, depending on the slipstream height.

Part III

3D Analysis

In this third part of the thesis, the analysis is focused on the 3D problem of a wing influenced by a propeller slipstream of finite dimensions. To simplify the analysis, the focus is put on the axial velocity added by the propeller and therefore, the propeller swirl is ignored. In this part, first the used methods are described, including the mathematics which are involved, after which the setup of the validation CFD simulation is discussed. The 2D correction method described in Part 2 is implemented into a lifting-line tool to correct for the slipstream height at each 2D wing strip, which is discussed in Chapter 7. Furthermore, the method of image vortices is applied in 3D, increasing the accuracy compared to the adjusted lifting-line approach. Two methods are introduced of which the first uses a similar image strategy as was done in 2D, further referred to as the intermediate 3D image method. The second method involves the introduction of the bound vortex influence and is called the full 3D image method. The two 3D image methods are discussed in Chapter 8, together with the introduction of the single panel vortex lattice approach. Finally, 3D CFD simulations were performed to validate the different methods. The setup of the simulations is discussed in Chapter 9. The results of the different methods and the CFD simulations are presented and discussed in Chapter 10.

7

Lifting-Line Approach Including 2D Corrections

In Part 2, the 2D analysis of an airfoil submerged in a jet of finite height is discussed. By using a system of successive images, located on both sides of the jet boundaries, a potential flow method is found which can correct for the influence of the jet boundary on the airfoil lift augmentation. This method was validated using CFD simulations and it was found that the results of the potential flow tool match the CFD data accurately. For the 3D analysis of a wing, which is partially submerged in the propeller slipstream, a lifting-line or vortex lattice method can be used, as is discussed in Section 5.1. Unfortunately, existing tools over-estimate the influence of the slipstream on the wing lift distribution. A possible reason is the disregard of the sectional slipstream height in the strip-wise approach. To model the propeller-wing interaction more accurately, a 3D potential flow model is needed which includes the effect of the finite slipstream height. The LL method is computationally the least expensive one and hence this method is adapted to take the 2D correction method into account. The theoretical background and governing equations are discussed in Section 7.1, after which the analysis results of this method are presented in Section 7.2. The correction method can also be applied to the local velocity instead of the local lift curve slope. This velocity correction was also done in the study of NASA SCEPTOR project [32, 33] and the application is discussed in Section 7.3.

7.1. Theoretical Background

For straight and slender wings, an initial low-fidelity approach is the LL method. The main assumption of the LL is that the wing has a large aspect ratio (AR), which means that locally at the wing, the response to the resultant inflow can be computed assuming 2D section characteristics. As explained in Section 3.2, the lifting-line analysis is a strip analysis, where the wing is modeled as one single lifting-line, which is located at the quarter chord location. Any change in bound circulation between the strips is associated with a shed vortex, trailing downstream from the wing. This trailing vortex influences all neighboring strips, due to its induced downwash. The trailing vortices from all the strips together form a complete vortex sheet behind the wing. This can be seen for a discretized wing in Figure 7.1. The spanwise position is denoted by the z-coordinate, while the other two dimensions are consistent with previous use, namely, the x-axis is pointing in the freestream direction, while y denotes the vertical direction. The created downwash reduces the local 2D angle of attack and hence the circulation at each section. This reduction results again in a different trailing vortex sheet and hence a different downwash field. The LL method solves the problem by finding the circulation distribution for which the downwash field creates this 2D sectional circulation at each panel.

The wing is modeled to be on the x-z plane and the method does not take the thickness of the wing into account. Furthermore, the bound vortex line must be on a straight line, since a vortex filament cannot just end in mid-air [11], and hence no sweep or dihedral of the wing can be modeled. So the method is limited to straight wings, but the wings can have a varying chord distribution as long as the quarter chord line is kept straight. In theory, the wing can have a varying airfoil geometry and aerodynamic angle of attack along the span, due to a possible twist angle. Due to the linearization assumptions, only small wing loadings can be modeled, meaning no large α. Furthermore, the span (b) must be large compared to the chord and this limits the method to large AR wings. From experiments, it is shown that the LL method shows reasonably accurate result for $AR > 4$ [11]. For more general shapes, the VLM should be used, and to take into account the thickness of the wing, a 3D panel method should be used.

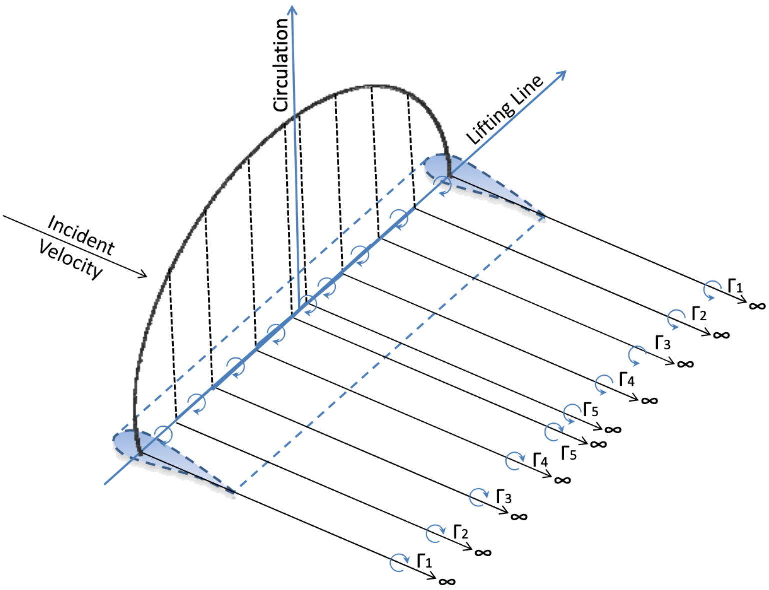

Figure 7.1: Visualization of the lifting-line method including the circulation distribution [47]

The sectional lift coefficient is given by Equation 7.1, where C_{l_α} is the sectional lift coefficient slope. Often, the thin airfoil slope (2π) is used, but the effect of wing thickness can also be accounted for by varying this value. The effective angle of attack (α_{eff}) is given by Equation 7.2, which is influenced by the variation in circulation. As discussed in Section 3.2, the swirl component of the propeller (w_p) is modeled as an extra vertical component and hence also a change in angle of attack (α_p), see Equation 7.3. Note that this equation, just as the lifting-line method, assumes small angles, and α_g is the geometric angle of attack, α_t is the twist angle and α_i is the induced angle of attack, generated by the downwash.

$$C_l = C_{l_\alpha}\left(\alpha_{eff} - \alpha_{0_L}\right) \quad (7.1) \qquad \alpha_{eff} = \alpha_g - \alpha_{0_L} + \alpha_t - \alpha_i + \alpha_p \quad (7.2) \qquad \alpha_p = \arctan\left(\frac{-w_p}{V}\right) \approx \frac{-w_p}{V} \quad (7.3)$$

It is important to note that C_l is the normalized sectional lift using the local velocity ($V(z)$) and not V_∞ as is the case in the conventional lifting-line method. This means that the axial induced velocity of the propeller slipstream can be added ($V(z) = V_j$ for strips inside the slipstream) [48]. As mentioned above, the local lift can also be calculated using the local circulation. Using the KJ theorem, the circulation can be related to the local sectional lift. Both methods to calculate the local lift must give the same result, see Equation 6.1 and hence, the local lift force can be expressed as a function of the circulation, resulting in Equation 7.4. The circulation can be calculated by finding the correct downwash and hence the correct α_{eff}. However, the downwash is also a function of the circulation itself, resulting in a integro-differential equation, which can be seen in Equation 7.5. The first term in the square brackets is the induced velocity due to the wing itself (downwash).

$$C_l(z) = \frac{2\Gamma(z)}{V(z)c(z)} \quad (7.4) \qquad \frac{2\Gamma(z)}{V(z)c(z)C_{l_\alpha}(z)} = \alpha_g(z) - \alpha_{0_L}(z) + \alpha_t(z) - \frac{1}{V(z)}\left[\frac{1}{4\pi}\int_{-b/2}^{b/2}\frac{d\Gamma/d\hat{z}}{z-\hat{z}}d\hat{z} - w_p(z)\right] \quad (7.5)$$

Only for an elliptical lift distribution, Equation 7.5 can be solved directly in an analytical manner, but for all other shapes, the problem must be solved numerically. As is done for the conventional lifting-line, the circulation distribution can be represented by a Fourier sine series, similar to the thin airfoil approach for the cambered airfoils. This series representation can be seen in Equation 7.6, where M is the total number of Fourier coefficients. To emphasize the distinction between $V(z)$ and V_∞, the latter is dropped from the series representation. Note, the θ is the transformed spanwise coordinate, as is done to simplify the equations. This is the same coordinate transformation as for the thin airfoil theory, which was discussed in Section 4.3.3. In this way, the integral of the circulation derivative can be solved directly, instead of an iterative approach. The derivative with respect to the transformed coordinate can be seen in Equation 7.7.

$$\Gamma(\theta) = \sum_{m=1}^{M} A_m \sin(m\theta) \tag{7.6}$$

$$\frac{d\Gamma}{dz} = \frac{d\Gamma}{d\theta}\frac{d\theta}{dz} = \sum_{m=1}^{M} m A_m \cos(m\theta)\frac{d\theta}{dz} \tag{7.7}$$

Once the integral is resolved, Equation 7.5 can be rewritten such that the unknown Fourier coefficients (A_m) can be determined, as can be seen in Equation 7.8. The Fourier coefficients can be used to obtain the circulation distribution over the wing and therefore also the sectional lift distribution and induced drag values.

$$\frac{2}{V(\theta)c(\theta)C_{l_\alpha}(\theta)}\sum_{m=1}^{M} A_m \sin(m\theta) = \alpha_g(\theta) - \alpha_{0_L}(\theta) + \alpha_t(\theta) - \frac{1}{2bV(\theta)}\sum_{m=1}^{M} m A_m \frac{\sin(m\theta)}{\sin(\theta)} + \frac{w_p(\theta)}{V(\theta)} \tag{7.8}$$

This equation can be solved in a numerical way, similar as for the thin airfoil theory, as was done in Equation 4.27. A system of linear equations can be set up to determine the Fourier coefficients. This is shown in Equation 7.9. By discretizing the wing in a large number of sections (I), the system can be solved to approximate the continuous circulation distribution. In theory, all the sections can have a different incident velocity, chord, twist angle and airfoil characteristics.

$$\underbrace{\left[\left[\sin(m\theta)\left\{\frac{2}{V(\theta)c(\theta)C_{l_\alpha}(\theta)} + \frac{m}{2bV(\theta)\sin(\theta)}\right\}\right]\right]}_{I\times M} \circ \underbrace{[A_m]}_{M\times 1} = \underbrace{\left[\alpha_g(\theta) - \alpha_{0_L}(\theta) + \alpha_t(\theta) + \frac{w_p(\theta)}{V(\theta)}\right]}_{I\times 1} \tag{7.9}$$

Using this method, the C_l-distribution is adjusted for both the axial and tangential velocities in the propeller slipstream compared to the regular LL. The former is added to the freestream velocity, while the latter is added to the effective angle of attack. However, at each strip where the propeller slipstream exists, the slipstream is assumed to be infinitely high. To model the effects of the slipstream height, the 2D sectional lift analysis could be adjusted. To focus on the propeller slipstream correction due to the finite jet height, the swirl is neglected for now. The strip analysis of the LL method allows to look at each 2D section individually and thus to apply the slipstream height correction method, discussed in Chapter 4.

For the LL including a propeller jet, some sections are outside the jet, having V_∞, while the sections inside the slipstream have V_j as input velocity. The sections inside the jet will be modeled having a rectangular piece of jet, where the height is the average value of that section. This is schematically shown in Figure 7.2 and by making the number of sections large, a continuous jet is approximated. As is discussed in Section 6.2.2, the K_{C_l} can be written as correction factor for the thin airfoil formulation. In Equations 6.2 and 6.3, the correction factor is written as f_{sym} and f_{cam} for the symmetric and cambered airfoils respectively. Using this approach, the lift coefficient slope can be adjusted in the LL formula, see Equation 7.10. Note that the axial induced slipstream velocity is already included in the $V(\theta)$ term.

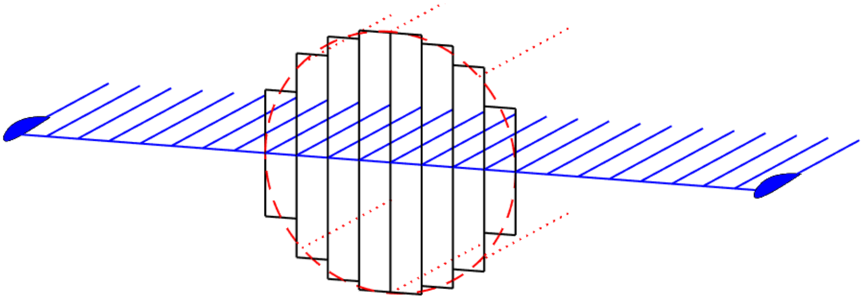

Figure 7.2: Schematic representation of the LL model including a propeller jet

This method is not limited to constant velocity propeller slipstreams, since every section can have a different velocity input. However, the vertical variation in velocity for each spanwise station cannot be taken into account. Perhaps by using an effective or average velocity, this variation can be modeled. For solving the linear system of equations (see Equation 7.9), the number of Fourier coefficients should be sufficient to describe the circulation distribution accurately. Similarly as for the 2D successive image method, the number of Fourier coefficients should be theoretically equal to the number of spanwise stations, but a lower number of coefficients can be solved using a least-squares method. In the next section, results from this adjusted lifting-line method are presented and differences between applying the 2D height correction and the conventional solution without corrections are discussed. The influence of the slipstream induced velocities on the wing aerodynamics is discussed in Section 2.3.

$$\sin(m\theta)\left\{\frac{2}{V(\theta)c(\theta)\ C_{l_\alpha}(\theta)\cdot f_{cor}(\theta)}+\frac{m}{2bV(\theta)\sin(\theta)}\right\}\circ A_m=\alpha_{eff} \tag{7.10}$$

7.2. Verification and Sensitivity Studies

In this section, the verification and sensitivity study of the adapted LL method are presented and discussed. In the previous section, it is explained that the equations are adjusted to take the local slipstream height of each section into account. The correction method is applied to the local lift coefficient slope and the circulation distribution is described using a Fourier series representation. Firstly, the method should be checked using a different source. The verification is done using XFLR5 [49] and afterwards, the difference in lift distribution with and without 2D correction factor is discussed. The adjusted LL method was programmed using Matlab. A generic result of a wing lift distribution with the influence of both the axial and swirl component of a circular slipstream can be seen in Figure 2.7a.

7.2.1. Verification of the LL Method

The LL method was verified using XFLR5, to check if the method was implemented correctly. XFLR5 is an aerodynamic flow solver, which uses the 2D XFOIL program in the 3D analysis [49]. XFOIL is a potential flow solver which uses 1D boundary layer integral equations to account for viscous effects. Using both empirical and theoretical turbulence and transition models, XFOIL tries to predict more complex flow phenomena, such as the transition from laminar to turbulent or laminar separation bubbles and stall at high angles of attack [42]. For the 3D analysis in XFLR5, the wing geometry can be defined and the user can choose between LL, VLM or a 3D panel method.

For the verification of the adjusted LL method, a simple wing is chosen to be analyzed. The wing was modeled as a straight wing with $AR = 5$, no taper and a symmetric profile everywhere. Furthermore, no twist was introduced and α was set to 2°. XFLR5 cannot handle the case with jet, so no propeller induced velocities are taken into account. Furthermore, the inviscid option is used, since the lift distribution can also be calculated using the viscous boundary layer models from XFOIL. In Figure 7.3a, the results of the verification process are shown. For the adjusted lifting line method, a total number of 1000 sections were used. For the XFLR5 analyses, 50 spanwise were used to calculate the lift distribution. As can be seen in Figure 7.3a, the data of LL analysis from XFLR5 matches that of the adjusted LL model programmed and hence it verifies the correct implementation of the numerical code.

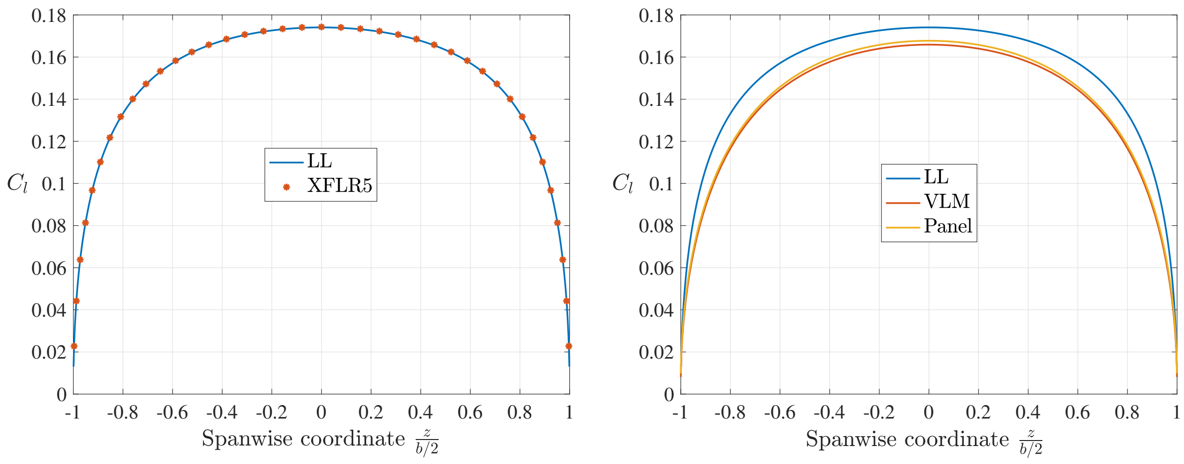

(a) Comparison between the described LL method and XFLR5's LL

(b) Comparison between the three different methods of XFLR5

Figure 7.3: Spanwise C_l distribution along the straight NACA 0012 wing having $AR = 5$ and $\alpha = 2°$

XFLR5 was also used to evaluate the potential modeling error by using the lifting-line approach instead of the vortex-lattice or panel methods. Using the inviscid VLM and panel options of XFLR5, the difference between the three methods can directly be visualized. For these additional analyses in XFLR5, 20 chordwise panels were used in combination with the 50 spanwise panels. For a straight and slender wing, the difference between LL and VLM are expected to be small, since most of the circulation of each segment is created close to the LE, as explained in Section 4.3.3. The comparison is shown in Figure 7.3b, for the same aerodynamic problem as discussed above. It is clear that the LL method is over-estimating the lift compared to the VLM and even the panel method. It is expected that the panel method produces a larger lift compared to the LL and VLM results, since the thickness is taken into account. This is confirmed by the fact that the panel method shows an increase in lift compared to the VLM. The reason that the LL method is not close to the VLM is that the AR of the modeled wing is close to the lower bound of 4. For small AR wings, the influence of the downwash on the chordwise lift distribution becomes important, and in particular the effect of the tip vortices. Apparently, for the smaller AR wings, the better chordwise discretization of the VLM and panel method results in a reduced lift compared to the LL method. In the next section, more results regarding the effect of the AR are presented.

7.2.2. Influence of Aspect Ratio

To investigate the effect of AR on the results of the LL method, more wings are modeled and analyzed with XFLR5. In Figure 7.4, the C_l distribution is shown for the same NACA 0012 wing, but with $AR = 10$ and $AR = 20$. For the former, see Figure 7.4a, the difference between the LL method and VLM becomes less, as is expected, but the LL method still over-predicts the lift. The panel method's maximum C_l is higher than that of the LL method, but near the tips, the values are still lower. Finally, for the $AR = 20$ wing, see Figure 7.4b, the LL shows an even better agreement with the more advanced VLM. Still, at the tip regions, the lift is slightly higher for the LL method than the VLM or panel method.

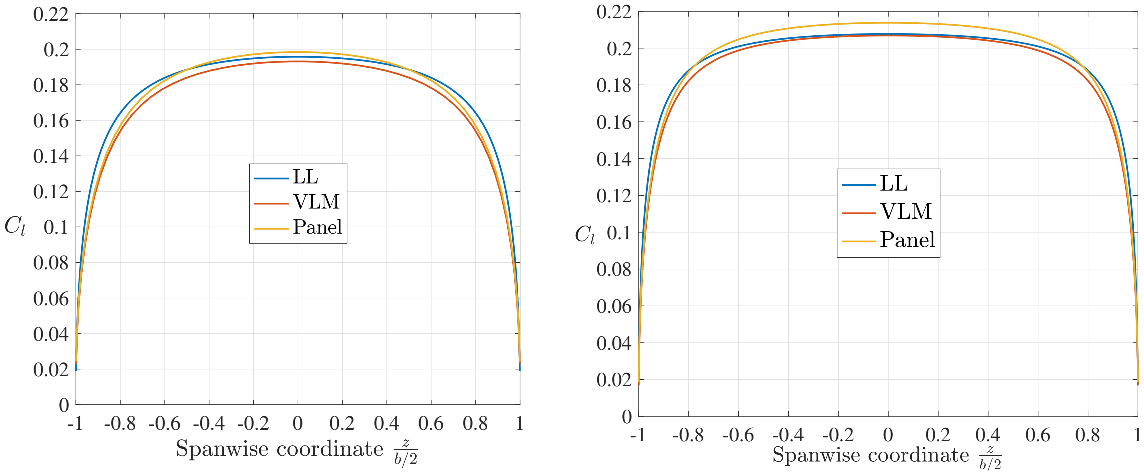

(a) $AR = 10$ (b) $AR = 20$

Figure 7.4: Comparison of the LL method, VLM and 3D panel method using XFLR5

The verification of the LL method showed that the code was correctly implemented for the case of a wing in normal freestream. To have a similar accuracy compared to more advanced models, the aspect ratio of the wing should not be too small. Modeling less slender wings does not work well with the LL method due to the assumptions made. The spanwise circulation is described by the Fourier coefficients. However, the use of the Fourier series expansion is not as straight forward as it was for the thin airfoil case. More discussion about this is found in the next section.

7.2.3. Sensitivity to Number of Fourier Coefficients

In the 2D thin airfoil theory, the results for the C_l, integral of the circulation distribution, converged quickly with an increasing number of Fourier coefficients. As explained in Section 4.4, the least-square method using a small number of Fourier coefficients resulted in a situation in which the boundary conditions were not met at most or even all control points, but this was of lesser importance in this approach. However, for the 3D analysis of the wing, the distribution of lift is of more importance than in 2D. Especially, when calculating the influence of the jet on the wing, a high accuracy of the sectional values is required. The accuracy of the circulation distribution is on one hand determined by the spanwise discretization of the wing. The more panels are used, the better the accuracy, as the continuous circulation distribution is approached. However, one important factor which comes into play is the discretization of the propeller slipstream. For the proper addition and correction of an axial jet, the number of sections inside the slipstream should be sufficiently high. The distribution in Figure 7.3a was made using 1000 panels and it turned out to be in the asymptotic range of the convergence. However, it is difficult to set up a convergence study, since this also depends on the number and position of possible propeller slipstreams.

On the other hand, the accuracy of the lift distribution is determined by the number of Fourier coefficients (M). For a generic distribution, as shown in the previous section, the number of Fourier coefficients can be low as the results quickly converge to a smooth distribution. However, when some propeller slipstream is added, the shape of the lift distribution is affected and it becomes more difficult to describe this shape with a low number of Fourier coefficients. Increasing the number of Fourier coefficients is not always beneficial for the accuracy. In Figure 7.5, the analysis results are shown for a wing including the propeller slipstream influence. The wing was the same as described above, having $AR = 10$. The jet was modeled as a circular slipstream having $R = 0.1b$ and the jet velocity, which was assumed constant throughout the jet, was set to 1.5 times that of the V_∞.

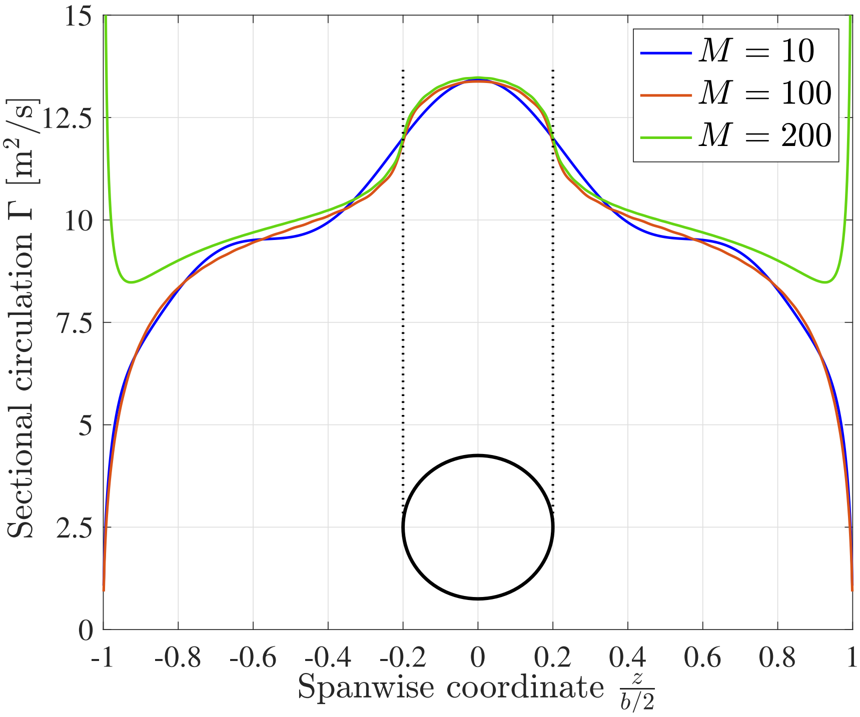

Figure 7.5: Distributed circulation distribution of the straight NACA 0012 wing including an axial jet in the middle of the wing

All lines were plotted using 1000 spanwise stations. The blue line represents the case of using 10 Fourier coefficients and as can be seen, the distribution is wavy, but seems to capture the increase in dynamic pressure due to the jet. If the number of coefficients is increased to 100, see the red line, the circulation distribution is much smoother and the influence of the jet is captured with better accuracy. Unfortunately, increasing the number of Fourier coefficients makes the result worse. The green line presents the solution using 200 Fourier coefficients. The circulation distribution near the tips diverges and this gets worse when the number of coefficients is increased even further. This looks like a similar phenomenon seen in the series expansion of discontinuous functions, the so-called Gibbs phenomenon. So the number of required Fourier coefficients to get a converged solution is linked to the number of sections chosen and the convergence must be checked for each individual case.

7.2.4. Applying the Height Correction Factor

In Figure 7.6, the result of the lifting-line analysis is shown. For the straight, $AR = 10$ wing without twist or taper, the Γ distribution along the span is shown including the influence of a propeller slipstream. A propeller is added at the center, of which only the axial velocity is taken into account, to demonstrate the effect of the slipstream height correction. The propeller radius was the same value as the chord, resulting in a maximum h/c of 2. The blue line shows the resulting sectional circulation without the correction factor and the red line shows the same parameter including the 2D slipstream height correction factor. It indeed shows a decrease in local lift and therefore better approximation of the real propeller induced effects in the slipstream.

The applied 2D correction method at each station seems to result in the desired effect, namely a decrease of local lift inside the slipstream due to the finite height of the propeller slipstream. Since the induced velocities of the sections inside the jet have an effect on the neighboring sections, the distribution is affected over a larger part than the jet actually spans. The adjusted LL method is solved within seconds if there is no correction factor applied. However, if the correction method is used, for each panel inside the propeller slipstream the successive image method must be performed. Therefore, it is needed that this correction method is also executed very fast. The convergence study of the 2D method, as is discussed in Section 4.4, showed that is possible and hence the corrected LL method is computationally wise not much more expensive than the original method. The question remains if this method can be validated and hence can be applied to all sorts of cases of propeller-wing interaction. This validation step is done in Chapter 10.

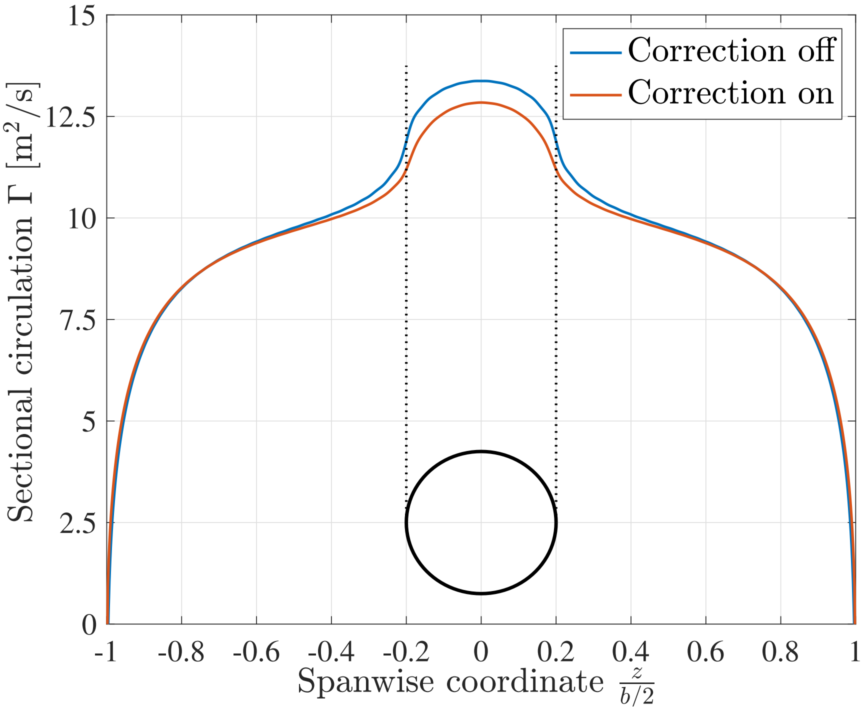

Figure 7.6: Distributed circulation distribution including propeller axial velocity

7.3. Sectional Velocity Correction

For the results of Figure 7.5 and 7.6, the value of the dimensionless C_l was intentionally replaced by the dimensional value of the sectional circulation. The circulation is the parameter that is determined in the lifting-line method by the Fourier coefficients. The value of C_l can be determined by using Equation 7.4 or 6.1. However, the problem that now arises is that of the use of the KJ theorem, as discussed in Section 3.3 and 6.3.3. Normally, the lift of the wing is normalized by V_∞. Using this value instead of the $V(z)$, the C_l distribution remains smooth and the shape is unaltered. This is shown in Figure 7.7 with the blue line. However, by using the local velocity as is prescribed for the adapted LL method, the C_l distribution will exhibit a downward jump once the jet is reached, since the local velocity here is suddenly higher. This is shown by the red line in Figure 7.7, where the propeller slipstream is located at the same positions as before.

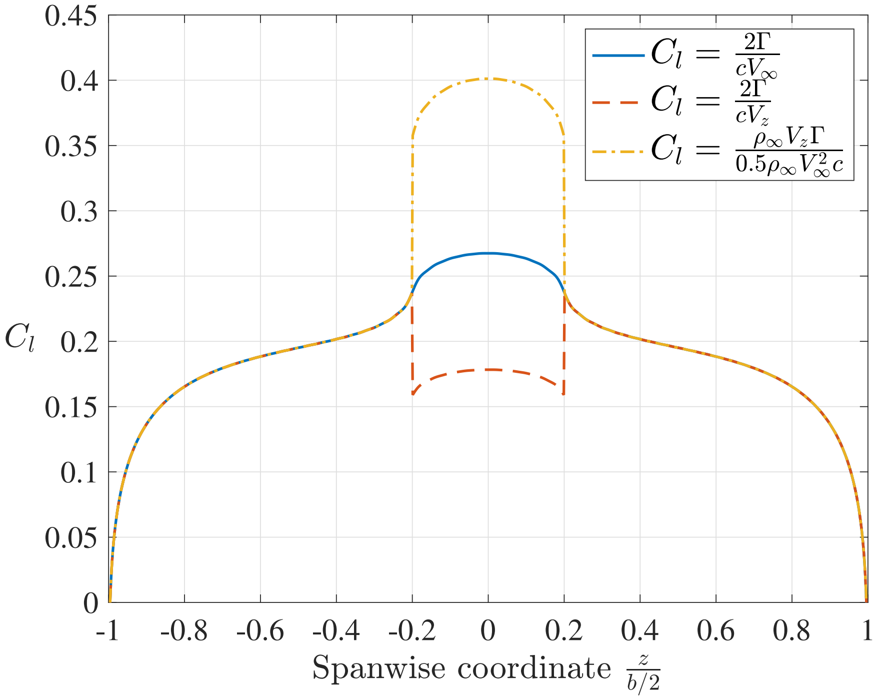

Figure 7.7: Difference in the definition of C_l

The instantaneous jump feels counter intuitive and the fact that the C_l gets smaller in the jet region, strikes against the general propeller-wing behaviour as discussed in Section 2.3. However, strictly speaking and by sticking to the definition written in Equation 7.4, the red line is the correct distribution. There is also a third possibility for the definition. By using $V(z)$ and ρ_∞ in the KJ theorem, the local sectional lift can be determined, which will also consist of instantaneous jumps at the slipstream boundary. If this sectional lift is then normalized using V_∞, which is normally the case, the C_l distribution will exhibit an instantaneous jump upwards inside the jet, since the lift does the same. This is shown by the yellow line in Figure 7.7. This definition will be used in the Chapter 10, where the CFD analyses are discussed. This is because the output of these analyses is the sectional lift and hence it is convenient to normalize this by using the freestream conditions.

One approach to get at least rid of the instantaneous jump in local lift and hence lift coefficient is by using a different 2D correction factor. In the current approach, the lift correction factor (K_{C_l}) is applied to the lift coefficient of an airfoil including an infinitely high jet (C_{l_∞}). Similarly as was done in the NASA SCEPTOR research [33], the local velocity can be corrected for the finite slipstream height instead of directly the lift coefficient. This means that the lift coefficient is assumed to be unaltered, while the velocity is lowered to end up with the same lift correction. In Equation 7.11, the formula for the local sectional lift (l_j) of the segments in the slipstream, including the correction factor, is rewritten, such that the velocity term contains this correction factor. So each section in the jet stream is corrected and an effective velocity is calculated.

$$l_j = {}^1\!/\!_2\rho_\infty V_j^2 \; c \; C_{l_\infty} \; K_{C_l} = {}^1\!/\!_2\rho_\infty \left(V_j\sqrt{K_{C_l}}\right)^2 c \; C_{l_\infty} \qquad (7.11) \qquad\qquad \left(V_j\sqrt{K_{C_l}}\right) = V_l \qquad (7.12)$$

Since the correction factor is only applied for sections inside the slipstream and it is assumed that the velocity throughout the slipstream is constant, the local corrected or effective velocity (V_l) can be written as Equation 7.12. This effective velocity can now be substituted into Equation 7.9, instead of $V(z)$. Using V_l instead of V_j for the sections inside the slipstream, the spanwise circulation distribution is altered marginally. When this newly defined velocity is used to calculate the sectional lift using the KJ theorem, the normalized coefficient is also slightly different compared to the case where the correction was only applied to the C_{l_α}. This can be seen in Figure 7.8, where the yellow line shows the new corrected C_l distribution. As can be seen, the yellow and the red line almost overlap, but the instantaneous jumps are removed from the method.

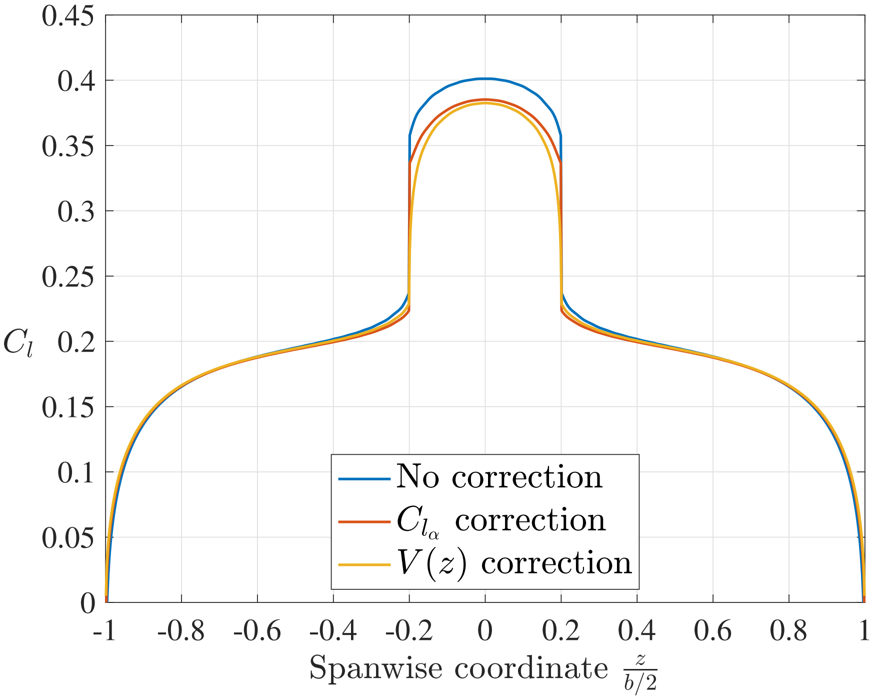

Figure 7.8: Difference in slipstream height correction on the C_l distribution

The choice between applying the correction factor on the lift coefficient or the local velocity does not make much of difference. However, since the latter looks more physically correct, this will be used in the analysis of the CFD results. The adjusted LL method is based on local 2D correction and hence the proximity of the slipstream boundary is not directly experienced by the segments directly outside the jet. The correction factor of each segment is only indirectly applied to the neighboring sections via the circulation calculation. The approach of images can also be expanded into 3D and is discussed in Chapter 8. To see if the adapted LL tool correctly predicts the lift reduction compared to the conventional LL method, CFD simulations are needed to validate this approach.

8

3D Image Methods to Account for the Circular Jet Boundary

The method discussed in the previous chapter is the application of the 2D correction tool, which models the effect of the finite slipstream on the sectional lift of an airfoil, in the lifting-line approach of modeling the propeller-wing interaction. This means that the effect of the slipstream correction on a specific wing segment only influences the neighboring sections indirectly via the computation of the circulation. However, the proximity of the propeller slipstream boundary influences all the spanwise wing sections and hence the questions arises if the former mentioned 2D correction method is sufficient to capture all the 3D phenomena. In this chapter, the image method as presented in 2D is expanded to 3D and two new correction methods are defined. The first method still uses the 2D Ting method but includes the images in the complete system of horseshoe vortices. The second method, which is more complete, is based on the theory developed by Rethorst [50]. To develop these two methods, the LL approach was improved to include the downwash generated by the bound vortex parts of the horseshoe vortices. The principles of this single panel vortex lattice method are discussed in Section 8.1. The first of the two new methods is still based on the definition of the 2D images and is, therefore, the intermediate solution between the 2D and full 3D images method. This method is discussed in Section 8.2. The second of the two new methods is based on the division of horseshoe vortices in an odd and even part. The strength and location of the image vortices are redefined with respect to the 2D analysis and this method is discussed in Section 8.3. The sensitivity and convergence study of the 3D full image method is presented in Section 8.4.

8.1. Vortex Lattice Method

In the LL method, as described in the previous chapter, the sectional lift of the 2D segment submerged in the slipstream, is corrected by placing images on both sides of the slipstream edge. By using this method, the effect of the finite height of the slipstream is included in each section by lowering the produced circulation. However, the images of these sections would theoretically also impose induced velocities in the spanwise direction and hence influence all neighboring wing segments. To expand the system of images to 3D, the images of each section must be added to the whole system of horseshoe vortices and their position and strength must be determined such that the boundary conditions along the circular boundary of the slipstream are satisfied. As a first attempt, the system of 2D images is simply expanded to 3D by placing the images above and below the wing segments, as is done in the 2D case. This will be further explained in Section 8.2. However, by including the images into the 3D flow regime, the images will induce velocities at each control point along the wingspan. This simple expansion means that the position and strengths of these images are still determined by the 2D analysis of the slipstream height. To include the effect of the image vortices on all spanwise stations, the LL is not sufficient.

The LL method uses the principle that the change in circulation of the wing is created by the trailing vortex sheet. The downwash generated at each section influences the induced angle of attack and this changes the created circulation computed using the thin airfoil theory. This theory is not based on the boundary condition of zero normal velocity and also the induced velocity of the bound vortex is not taken into account.

However, the system of equations for the LL method, explained in Section 7.1, is not able to include the influence of vortex sheets located at a different vertical position compared to the lifting line plane. Therefore, the LL is not usable in this approach and the method had to be expanded into a VLM. The VLM requires more computational time than the LL method, as explained in Section 3.2.2. To simplify the analysis and hence reduce the computational cost, the VLM used will only have a single panel in chordwise direction and therefore it can be seen as an enhanced version of the lifting-line method [51]. The schematic representation of the single panel VLM can be seen in Figure 8.1a.

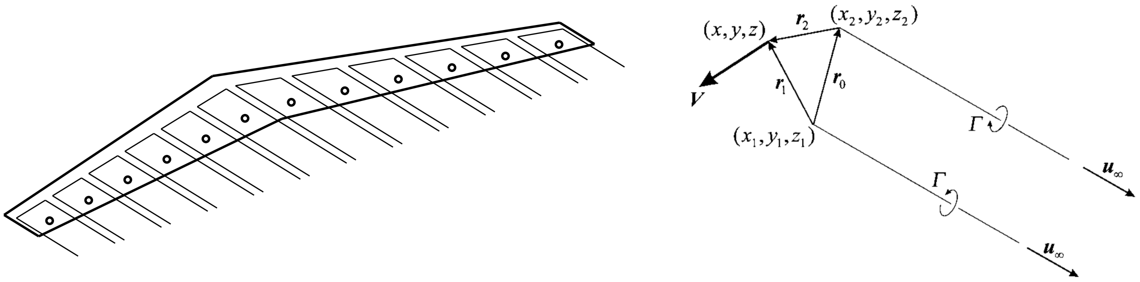

(a) Single panel VLM including the control points

(b) Position vectors of a horseshoe vortex

Figure 8.1: Schematic representation of the VLM [51]

The horseshoe vortices are all located with the bound part on the quarter chord line and the control points are located at the three quarter chord line of each section. The VLM is based on the boundary conditions of zero normal velocity at the control points. This means that the induced velocity of all the horseshoe vortices must be equal, but opposite in direction compared to the freestream velocity in the direction normal to the panel. This is mathematically shown in Equation 8.1 and for a straight wing without dihedral, $\vec{n}$ is in the y-direction. The induced velocities due to the horseshoe vortices ($\vec{V_\Gamma}$) can be calculated using the Biot-Savart law, see Equation 8.2.

$$\vec{V} \bullet \vec{n} = \left(\vec{V_\infty} + \vec{V_\Gamma}\right) \bullet \vec{n} = 0 \tag{8.1}$$

$$\vec{V_\Gamma} = \sum \frac{\Gamma_i}{4\pi} \frac{\vec{dl} \times \vec{r}}{|\,\vec{r}\,|^3} \tag{8.2}$$

The Biot-Savart equation can be rewritten in such a form that the influence of the left and the right trailing vortex, and the bound vortex is expressed as three separate components. For the influence of the three vortices, the edges of the bound vortex part are used as a reference point. This can be seen in Equation 8.3 [51]. Depending on the distance from these three components to a specific control point, the induced velocity is different. The position vectors of this equation can be seen in Figure 8.1b, in which $\vec{V_\infty}$ is the freestream velocity vector. The control points are located in the middle of each horseshoe vortex at 1/2 chord distance from the bound vortex.

$$\vec{V_\Gamma} = \frac{\Gamma}{4\pi}\left[\frac{\vec{V_\infty} \times \vec{r_2}}{r_2\left(r_2 - \vec{V_\infty} \cdot \vec{r_2}\right)} + \frac{(r_1 + r_2)\left(\vec{r_1} \times \vec{r_2}\right)}{r_1 r_2\left(r_1 r_2 + \vec{r_1} \cdot \vec{r_2}\right)} - \frac{\vec{V_\infty} \times \vec{r_1}}{r_1\left(r_1 - \vec{V_\infty} \cdot \vec{r_1}\right)}\right] \tag{8.3}$$

The influence of all the horseshoe vortices on the control points results in a system of linear equations, similar to the lifting-line method, see Equation 8.4. The system will consist of a square matrix for the influence of each horseshoe vortex on each control point (denoted by F_{ij}). Note that the total number of spanwise segments is again presented by I. No Fourier coefficients are needed and the system is solved for the unknown circulation strengths. Using the KJ theorem, the local lift force of each panel can be calculated. On the right hand side of the equation, V_∞ is replaced by V_l. This means that the local increase in axial velocity can be taken into account if a certain horseshoe vortex is located inside the slipstream. Furthermore, the change in local angle of attack due to the swirl component of the slipstream could be included in the α term. The verification of the single panel VLM without jet, using XFLR5, can be seen in Appendix C. The single panel VLM code was programmed and analyzed using Matlab. The data from the new VLM code is also compared to CFD data to check its validity. This is discussed in Chapter 10, including the results of the other image vortex techniques, which will be discussed in the next sections.

$$\begin{bmatrix} F_{11} & F_{12} & \cdots & F_{1I} \\ F_{21} & F_{22} & \cdots & F_{2I} \\ \vdots & \vdots & \ddots & \vdots \\ F_{I1} & F_{I2} & \cdots & F_{II} \end{bmatrix} \begin{bmatrix} \frac{\Gamma_1}{4\pi} \\ \frac{\Gamma_2}{4\pi} \\ \vdots \\ \frac{\Gamma_I}{4\pi} \end{bmatrix} = - \begin{bmatrix} V_{l,1} \cdot \sin(\alpha_1) \\ V_{l,2} \cdot \sin(\alpha_2) \\ \vdots \\ V_{l,I} \cdot \sin(\alpha_1) \end{bmatrix} \tag{8.4}$$

8.2. Intermediate 3D Image Method

The first step in solving the 3D influence of the slipstream on the wing lift distribution is done by using a similar approach to the one applied in the 2D case, described in Section 4.3.3. The method presented in this section will therefore be referred to as the intermediate 3D image method, since it is halfway between the 2D and a full 3D image method. With the use of the single panel VLM tool, the images that would be created using the 2D correction method are added to the whole system of horseshoe vortices. So instead of calculating the effect of finite slipstream height only locally, the effect of each image is now imposed on all VLM panels. This is schematically shown in Figure 8.2. The strength of the images is determined by using the 2D analysis of Ting and is therefore a function of the velocity ratio V_j/V_∞. For a constant velocity slipstream, all images have the same strength, since V_j does not vary along the spanwise strips. Furthermore, the distances to the images are known since they are simply related to the local slipstream height, and hence the influence of these images on the local circulation distribution can be simply added to the influence matrix (F_{ij}) in Equation 8.4. As was found for the 2D method, only a few image sets were needed to get a converged solution, see Section 4.4. Therefore, only two images sets were used for this intermediate 3D image method, resulting in a total of eight images per horseshoe vortex located in the slipstream.

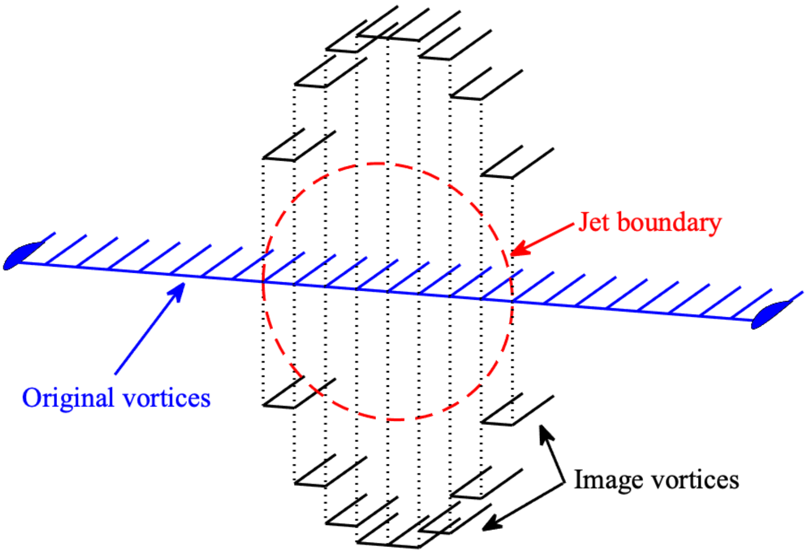

Figure 8.2: Schematic representation of the intermediate 3D image method

Using this approach, the effects of the horizontal boundaries of the jet are still not captured. In other words, the effect of the finite height at each section is now directly influencing all the horseshoe vortices, but the proximity of the jet to the panels just outside the slipstream is not modeled properly. If for example, a wing would be submerged into a rectangular jet, which has a very small width along the span but is infinitely high, the use of this intermediate image method would create no change in circulation compared to the conventional approach, since the images would be located infinitely far from the wing. By performing CFD simulations of both the circular jet and this specific case of a rectangular jet, the possible effect of neglecting the horizontal component of the slipstream boundary can be calculated. In the next section, the third image correction method is presented. In this method, the use of image vortices is redefined to fully capture the 3D influences of the slipstream boundary on the wing lift distribution.

8.3. Full 3D Image Method

To increase the accuracy of the use of image vortices in 3D, the downwash generated by the complete slipstream circular boundary should be taken into account. The method described in this section is completely based on the work of Rethorst [50]. This full 3D image method can be used to analyze circular jets and is based on the division of horseshoe vortices in even and odd systems. Furthermore, the method is based on satisfying the physical boundary conditions at the jet boundary and is therefore a better approach compared to the intermediate 3D image method. However, it is computationally the most expensive method.

8.3.1. Boundary Conditions and Image Locations

The full 3D correction method is based on the application of two separate potential functions, one for the flow inside the jet and one for the flow outside of it, similar to the 2D correction method, as discussed in Section 4.3.3. The potential functions must include the effect of the introduced image vortices, such that the boundary conditions at the slipstream edge are met, assuming the small perturbation theory. There are certain assumptions and simplifications made by the above-mentioned author and hence this method only works for slipstreams having a circular boundary and a constant axial velocity increase, just as in 2D. The setup of the problem is shown in Figure 8.3. The front view of the wing and jet is shown in 8.3a, where also the coordinate system is presented. This is equivalent to the one used throughout the complete thesis. In Figure 8.3b, the top view of a rectangular wing is shown including the incoming axial velocity components. Furthermore, a single horseshoe vortex is shown, which is located inside the jet. The method makes use of a single panel VLM, as is described in Section 8.1, meaning the control point of each horseshoe vortex is located at the 3/4 chord point.

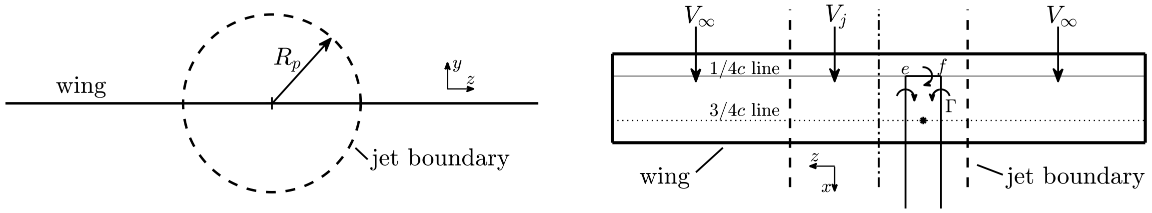

(a) Front view indicating the circular jet

(b) Top view indicating a specific horseshoe vortex located inside the jet

Figure 8.3: Geometric setup of the full 3D image method

The two conditions that are needed to be satisfied at the jet boundary are equal to that of the 2D approach. However, the boundary conditions must be expressed in the cylindrical coordinate system. To boundary condition of equal pressure on both sides is given by Equation 8.5, where u_a indicates the disturbance velocity in the axial direction, both inside (j) and outside the jet (∞). In this method, it is assumed that the propeller axis is parallel to the x-axis and hence the axial velocity component can be added to the incoming velocity component. The second boundary condition, that of equal slope on both sides of the jet boundary, takes the radial velocity component into account, see Equation 8.6. In this equation, u_r is the radial component of the disturbance velocity in both the jet and the freestream flow.

$$V_j u_{a,j} = V_\infty u_{a,\infty} \tag{8.5}$$

$$V_j u_{r,\infty} = V_\infty u_{r,j} \tag{8.6}$$

To satisfy these boundary conditions, the introductions of images is needed. The strength of the images is again a function of the velocity ratio between V_∞ and V_j. Due to the circular boundary, the application of image vortices is less straight forward compared to the 2D case. Furthermore, since the wing spans the jet on both sides, there are both vortices located inside and outside the jet. For the circular slipstream, the relation between the image position of a vortex and the position of the vortex itself can be determined by using complex coordinates [36]. The complex coordinate of a horseshoe vortex on the y-z plane is denoted by $\varsigma = z + iy$. The subscripts o and i are for the original and image vortex respectively. The image of a vortex is located at the inverse point of the complex conjugate of this vortex, see Equation 8.7. Using this relation, the position of the image vortex can be calculated and this is presented in Equation 8.8 and 8.9 for the spanwise and vertical coordinate respectively.

$$\varsigma_i = \frac{R_p^2}{\bar{\varsigma}_o} \tag{8.7}$$

$$z_i = \frac{R_p^2 \, z_o}{z_o^2 + y_o^2} \tag{8.8}$$

$$y_i = \frac{R_p^2 \, y_o}{z_o^2 + y_o^2} \tag{8.9}$$

For the single panel VLM, it is assumed that the horseshoe vortices are all located in the same plane, which is at $z = 0$, which means only Equation 8.8 is used. So the way to determine the location of the images is by using the inverse point of the original vortex with respect to the center of the jet [36]. To visualize this process, Figure 8.4 is used, which shows the location of two vortices located inside the jet including their images.

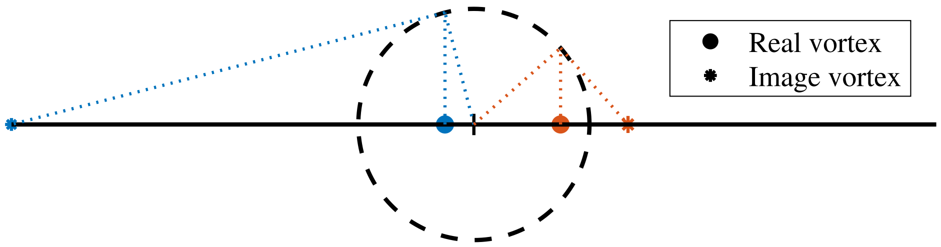

Figure 8.4: Schematic visualization of two line vortices including their images

The images of the original vortices are located at the inverse positions compared to the non-dimensionalized spanwise jet position. For example, if the blue vortex is located at $z/R_p = -0.25$, the image of it will be located at $z = 1/-0.25 = -4R_p$. Similarly, the red vortex, which is located at $z/R_p = 0.75$, will have an image at $z = 1/0.75 = 4/3R_p$. The same can be done for vortices which are located outside of the jet, meaning their images will be located inside the jet. This process of inverse distances also means that a vortex located at the center of the jet will have an image infinitely far away. Vortices close to the center will have an image that is located outside of the wingspan. Furthermore, the vortices close to the jet boundary will have an image that is close by and hence the influence of the horizontal jet boundaries on the local lift distribution will be largest close to these boundaries. The induced velocity components of all the images (G_{ij}) can be added to the downwash generated by the original vortices (F_{ij}) to solve for the unknown circulation values, as can be seen in Equation 8.10.

$$V_l \sin(\alpha) = \frac{\Gamma}{4\pi}\left\{F_{ij} + G_{ij}\right\} \cdot n \tag{8.10}$$

The most difficult part is finding these G values, since the strength of the images is not simply scaled as was done in the 2D case. For the determination of the image strengths and hence the effect of the jet boundary on the wing lift distribution, the two governing potential functions must be defined and the derivatives of these result in the perturbation velocity components, from which the scaling factors can be determined. To ease the calculations, the horseshoe vortices are split into an even and odd part with respect to the direction of the incoming flow [50].

8.3.2. Division of Horseshoe Vortices

A single horseshoe vortex of strength Γ can be decomposed into an even and odd half, which is visualized in Figure 8.5. The two halves satisfy the set boundary conditions independently and hence this division must not pose any problem [50]. The decomposition of the horseshoe vortex is done with respect to the x-axis and the even system turns therefore effectively into a 2D problem of trailing vortices. The influence of the trailing vortices was captured before using similar correction methods by Koning [36]. Furthermore, this method was used to also model non-uniform propeller slipstreams [31, 52, 53]. However, the effect of the odd system and hence the influence of the bound vortex can not be neglected for analyses where the slipstream velocity is significantly larger than the freestream velocity [50]. The effect of neglecting the odd part is further discussed in Section 10.4.

For the odd system, the situation is much more complicated. Rethorst suggested to make use of Bessel functions to come up with a series representation of the potential functions. The use of these Bessel functions makes the equations rather lengthy and complicated. Therefore, only the final equations for G will be given in this thesis. For further explanation, see the original paper [50]. The use of Bessel functions as part of series representations can be partially simplified again by assuming that the potential functions are odd with respect to the x-axis.

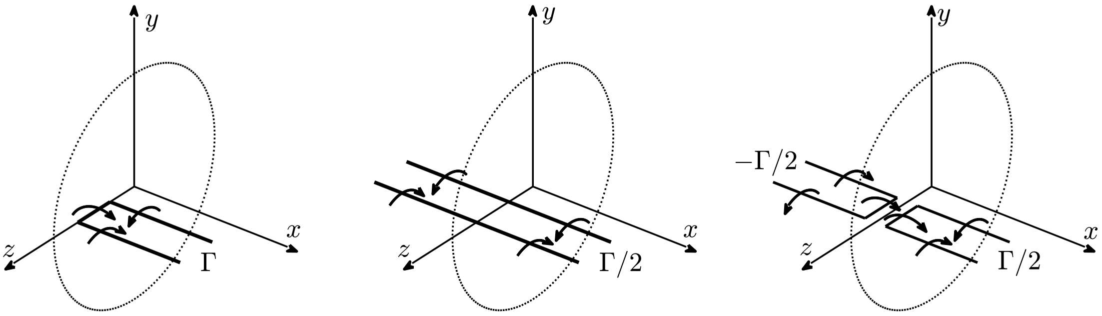

(a) Complete horseshoe vortex (b) Even system (c) Odd system

Figure 8.5: Division of a horseshoe vortex into an even and odd system [50]

To make use of the assumption that the velocity potential is odd with respect to the x-axis, the downwash field must be symmetrical with respect to this axis, which means the jet must be in the symmetry plane of the wing. The equations presented by Rethorst are derived for propeller-wing interactions where the jet is located at the center of the wing. This poses a large limitation on this method, but the effect of these simplifications is investigated further in Section 8.4.3. By assuming a symmetrical case, the system of equations for the even halves can be simplified even more. This leads to the use of image vortex pairs, spaced symmetrically with respect to the jet center. The use of image vortex pairs can be seen in Figure 8.6. In the figure, a horseshoe vortex is located with the bound vortex between $z = e$ and f. The other horseshoe vortex of this pair is located between $z = -e$ and $-f$. Also, the four image points are located at the inverse locations of these positions.

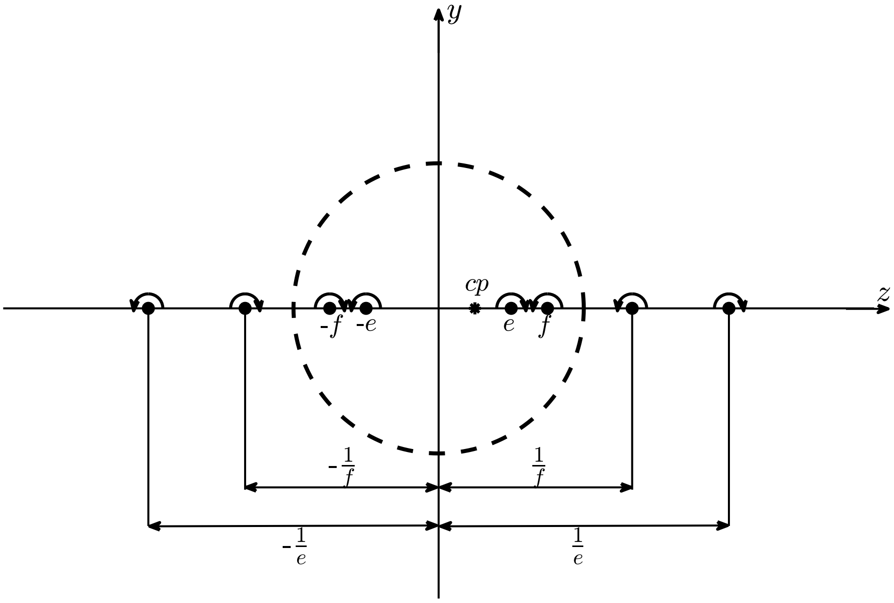

Figure 8.6: Two-dimensional vortex system of a pair of symmetrically spaced horseshoe vortices [50]

For vortex pairs which are located outside the jet, the situation is similar to the presented figure, but then with the image located inside the jet. The case for a vortex inside or outside the jet and for the representative flow field caused by the image inside or outside the jet are treated separately and hence, four different equations are presented for both the odd and even system. The solutions are only available for the symmetric case at the moment. The asymmetric case would require additional derivations, which was outside of the scope of this thesis and is therefore left as a recommendation for future work.

Even System

For the even system, Equations 8.11, 8.12, 8.13 and 8.14 are applicable. In these equations, ζ is the non-dimensionalized spanwise coordinate, with respect to the jet radius (z/R_p), for the control point location. The first index of the G denotes the position of this control point. j stands for inside the jet, meaning for $-1 < \zeta < 1$, while o stands for outside the jet and hence when $|\zeta| > 1$. The second index denotes the position of the original vortex pair. Again j and o are used as described above, but now for the values of e and f. Finally, μ is similar to the 2D image strength and is defined as the inverse of the velocity ratio (V_∞/V_j) [50].

$$G_{jj_{even}}(\zeta) = \frac{1}{5}\frac{1-\mu^2}{1+\mu^2}\left[\frac{1}{(1/f)-\zeta} - \frac{1}{(1/e)-\zeta} + \frac{1}{(1/f)+\zeta} - \frac{1}{(1/e)+\zeta}\right] \tag{8.11}$$

$$G_{oj_{even}}(\zeta) = -\frac{1}{5}\frac{(1-\mu)^2}{1+\mu^2}\left[\frac{1}{\zeta-e} - \frac{1}{\zeta-f} + \frac{1}{\zeta+f} - \frac{1}{\zeta+e}\right] \tag{8.12}$$

$$G_{jo_{even}}(\zeta) = -\frac{1}{5}\frac{(1-\mu)^2}{1+\mu^2}\left[\frac{1}{f-\zeta} - \frac{1}{e-\zeta} + \frac{1}{f+\zeta} - \frac{1}{e+\zeta}\right] \tag{8.13}$$

$$G_{jo_{even}}(\zeta) = -\frac{1}{5}\frac{1-\mu^2}{1+\mu^2}\left[\frac{1}{\zeta-(1/e)} - \frac{1}{\zeta-(1/f)} + \frac{1}{\zeta+(1/f)} - \frac{1}{\zeta+(1/e)}\right] \tag{8.14}$$

Odd System

For the odd system, the equations are more complicated, due to the use of the Bessel functions. Equations 8.15, 8.16, 8.17 and 8.18 are used. Since the influence of the bound vortex is dependent on the distance to the control point, the four equations for the odd system are also functions of the non-dimensionalized x-coordinate ($\xi = x/R_p$). However, for a straight wing without sweep, taper or dihedral, the positions of the control points are on a straight line and hence the value of ξ is fixed. The computationally expensive part is the double integral of modified Bessel functions of order ν. In theory, also an infinite amount of values for ν are used. I_ν denotes the modified Bessel function of the first kind, while K_ν represents the modified Bessel function of the second kind. I'_ν and K'_ν are the first-order derivatives of the modified Bessel function of the first and second kind respectively. The Bessel functions have argument λ, which is the dummy running variable for the integrals, unless otherwise stated [50].

$$G_{jj_{odd}}(\xi,\zeta) = \frac{8}{5\pi\zeta}\sum_{\nu=0}^{\infty}(2\nu+1)^2\int_0^\infty \frac{K_\nu K'_\nu I_\nu(\zeta\lambda)\sin(\xi\lambda)}{\left[1/\left\{(1/\mu^2)-1\right\}\right]-\lambda I_\nu K'_\nu}\int_{e\lambda}^{f\lambda}\frac{I_\nu(\lambda_\beta)}{\lambda_\beta}\,d\lambda_\beta\,d\lambda \tag{8.15}$$

$$G_{oj_{odd}}(\xi,\zeta) = \frac{8}{5\pi\zeta}\sum_{\nu=0}^{\infty}(2\nu+1)^2\int_0^\infty \left[\frac{1}{\mu-\lambda\left\{(1/\mu)-\mu\right\}I_\nu K'_\nu} - 1\right]\frac{K_\nu(\zeta\lambda)\sin(\xi\lambda)}{\lambda}\int_{e\lambda}^{f\lambda}\frac{I_\nu(\lambda_\beta)}{\lambda_\beta}\,d\lambda_\beta\,d\lambda \tag{8.16}$$

$$G_{jo_{odd}}(\xi,\zeta) = \frac{8}{5\pi\zeta}\sum_{\nu=0}^{\infty}(2\nu+1)^2\int_0^\infty \left[\frac{1}{\mu-\lambda\left\{(1/\mu)-\mu\right\}I_\nu K'_\nu} - 1\right]\frac{I_\nu(\zeta\lambda)\sin(\xi\lambda)}{\lambda}\int_{e\lambda}^{f\lambda}\frac{K_\nu(\lambda_\beta)}{\lambda_\beta}\,d\lambda_\beta\,d\lambda \tag{8.17}$$

$$G_{oo_{odd}}(\xi,\zeta) = \frac{8}{5\pi\zeta}\sum_{\nu=0}^{\infty}(2\nu+1)^2\int_0^\infty \frac{I_\nu I'_\nu K_\nu(\zeta\lambda)\sin(\xi\lambda)}{\left[1/\left\{(1/\mu^2)-1\right\}\right]-\lambda I_\nu K'_\nu}\int_{e\lambda}^{f\lambda}\frac{K_\nu(\lambda_\beta)}{\lambda_\beta}\,d\lambda_\beta\,d\lambda \tag{8.18}$$

The second integral is nested within the first integral, meaning for every value of the running variable λ, there is a complete integral on the scaled domain $e\lambda$ till $f\lambda$, having running variable λ_β. For the calculation of the local circulation, see Equation 8.10, the local velocity is used. Furthermore, for the calculation of the local lift from this circulation distribution, the local velocity is used again. In the next section, the sensitivity analysis of the 3D full image method is discussed. The 3D full image method was verified using the data presented in the paper of Rethorst [50], but was left out of this report since it was very lengthy.

8.4. Convergence and Sensitivity Study

This section focuses on the sensitivity and convergence of the 3D full image method. The single panel VLM without any correction method only has the discretization of the wing as a numerical aspect and therefore, this was not analyzed in this section. Furthermore, the intermediate image method is based on the placement of the 2D images and the convergence study of this method was already presented in Section 6.2. The even system of the full 3D image method also does not show any numerical evaluation besides the discretization of the wing. However, the odd system has two additional numerical aspects, namely the summation of ν, the order of the Bessel functions, and the upper limit of the integration of the running variable λ. Both numbers should, in theory, be infinitely large. By varying the numbers of both parameters, the convergence can be checked.

8.4.1. Order of Bessel Functions

The used Bessel functions are characterized by the order of the function and only the odd numbers are taken into account due to the symmetry assumption. To check the convergence, the relative discretization error (ϵ_{rel}) is used. The definition of this error can be seen in Equation 4.29. In Figure 8.7, the convergence trend for the total order of Bessel functions is shown. As can be seen in the figure, the solution quickly converges for the used order and for $\nu = 3$, the relative error is less than 0.5%. This is similar to the observed convergence by Rethorst, who decided to use $\nu = 4$ in the calculation of his results [50]. In the remainder of this thesis, the summation limit of ν was set to 3.

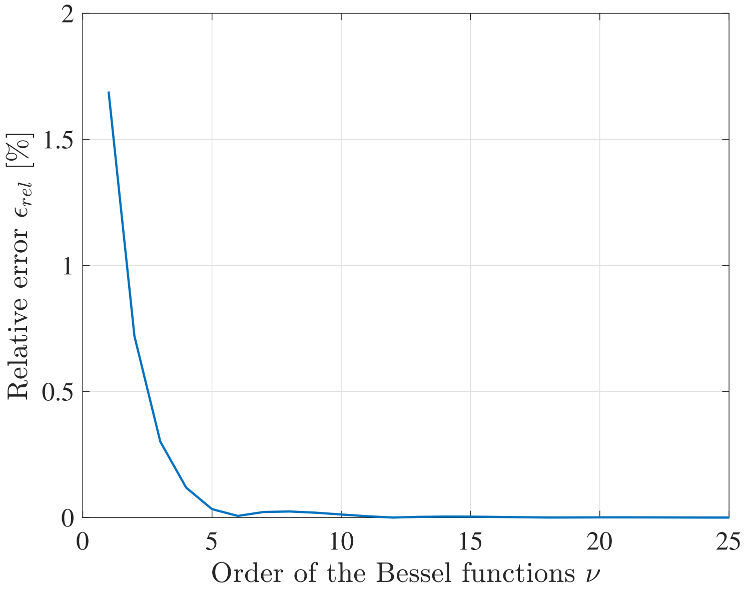

Figure 8.7: Convergence trend for the used orders of the Bessel functions

8.4.2. Upper Limit of Bessel Functions Integrals

The second numerical aspect of the odd system is the integral from zero to infinity, see for example Equation 8.15. These integrals were numerically solved using the trapezoidal method. For the stepsize, a small value of 0.05 was used to make sure this did not influence the convergence results. The convergence trend for the upper limit of the integration is shown in Figure 8.8. As can be seen, the relative error is less than 0.5% already for an upper limit of 8. Rethorst used an upper limit of 12, but used a significantly larger stepsize of 0.5 [50]. It can be concluded that by decreasing the stepsize of the trapezoidal method, the upper limit can also be reduced. The upper limit was set to 8 for the analysis of the propeller-wing interactions in this thesis.

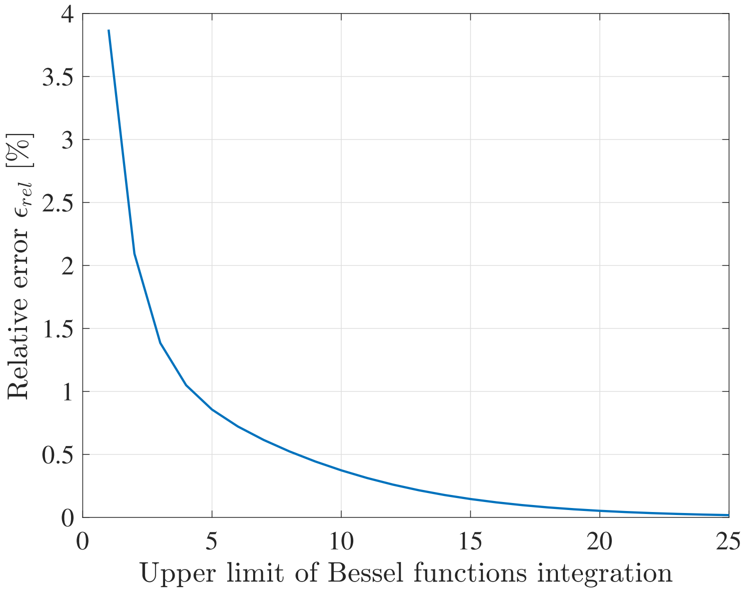

Figure 8.8: Convergence trend for the upper limit of λ in the numerical evaluation of the Bessel function integrals

8.4.3. Influence of the Symmetry Condition

The equations of the odd system are derived based on the assumption that the circular jet is located at the center of the wing. By doing so, the equations could be simplified by only using the odd terms. However, the case of an aircraft with a single propeller in the middle is not much encountered nowadays and this poses a limitation to the method. Especially in research projects which are about distributed propulsion systems, such as the NASA SCEPTOR project, many propellers are distributed over the wing. In this section, the sensitivity of the influence matrix G_{ij} is analyzed, to see the effect of the images on the wing. By doing so, an addition to the Rethorst method was defined which allows for the analysis of non-symmetric cases.

The influence matrix G_{ij} is the summation of all the even and odd equations presented in Section 8.3.2. The elements of this matrix represent the influence of all the vortex images (j) on all the control points (i). This influence matrix can be visually represented, see Figure 8.9. Note that matrix G_{ij} normally only contains half of the number of wing segments, since the symmetry conditions allow for solving only one half of the wing. In the figure, the matrix is mirrored to get the situation for the complete wing. With mirroring, the process is meant which transforms the matrix from an NxN to a $2Nx2N$ matrix by copying both the rows and the columns. The case analyzed for this influence matrix was that of a straight wing with $AR = 10$. The wing was discretized into 25 segments and the jet was centered in the middle of the wing. The radius of the slipstream was equal to the chord and the velocity ratio was set to $V_j = 1.5V_\infty$. The colors indicate the strength of the created downwash of the images on the control points. On the x-axis of the figure, the control points are represented, while on the y-axis, the images of the horseshoe vortices are shown. So each row shows the influence of image j on all the control points, while each column shows the influence of all the images on a single control point.

As can be seen, the influence of the jet is primarily visible inside the jet and close to the boundaries of it. This means that the effect of the slipstream edges quickly becomes negligible when moving away from the slipstream. The results from this analysis can be used to develop an approach to analyze non-symmetric cases. In the case of a jet which is centered in the middle of the wing, only one side of the wing is analyzed. However, the matrix can be mirrored to allow for the calculation of the complete wing. When the propeller slipstream is no longer centered in the middle of the wing, this expansion of the G_{ij} matrix can still be applied. However, the distances from the center of the jet to the tips are now not equal anymore. To continue the analysis, the part of the wing on the side the propeller slipstream which is the largest is used to calculate the initial G_{ij} matrix, as if the jet would be centered in the middle of the wing with a larger span.

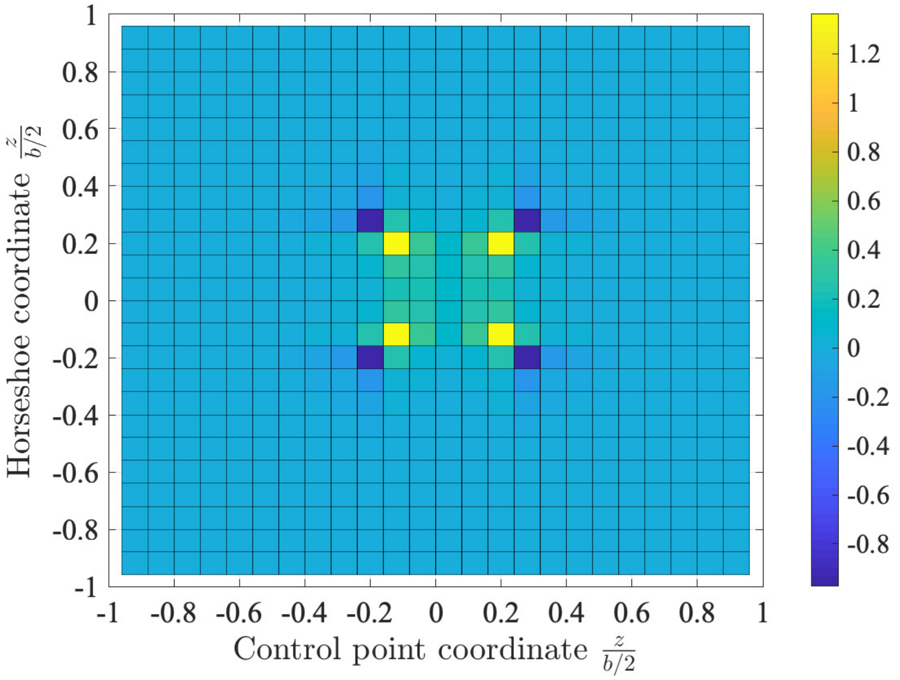

Figure 8.9: Visualization of influence matrix G for a wing with a jet at the center

This process is visualized in Figure 8.10. In this figure, the slipstream is placed towards the right tip. This means that the part of the wing on the left (seen from the front) of the slipstream now is bigger than the part on the right. The analysis described in Section 8.3.2 is now performed as if the wing would be longer, denoted by the imaginary part in Figure 8.10. The equations are solved as was done for the true symmetric case. Then the influence matrix G_{ij} is added to the original horseshoe downwash matrix F_{ij}. However, the images of the horseshoe vortices that would be located at the imaginary part of the wing are now neglected. This would, in theory, not produce a large error, since the influence of the slipstream is concentrated in and around it. However, by doing so, the boundary conditions on the slipstream edge are no longer satisfied, since part of the influence of the images is neglected. To see if this method is usable, CFD simulations of non-symmetrical propeller-wing interaction were performed.

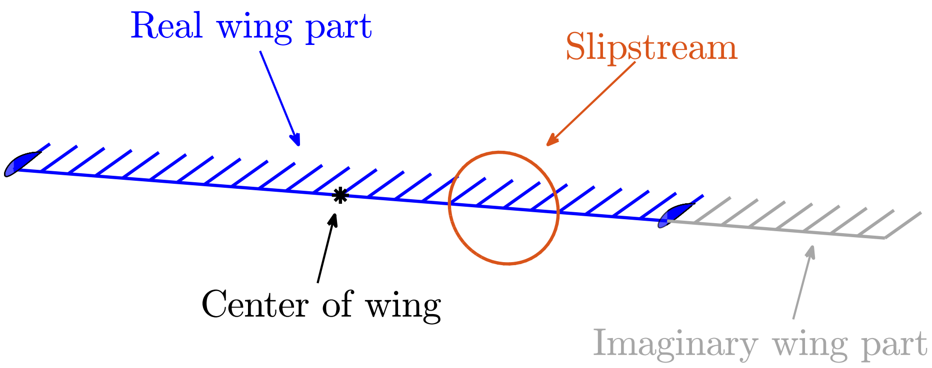

Figure 8.10: Visualization of the extension of the 3D full image method for non-symmetric slipstream cases

9

3D CFD Simulation Setup

The 2D potential flow method to account for the finite slipstream height was validated using CFD analyses and applied in the adjusted LL method. One of the most important observations from Chapter 6, is that a very fine grid was needed to get reliable results, since modeling of the potential flow using Euler equations introduces numerical viscosity. The method of successive reflections was applied in the strip analysis by correcting the local lift coefficient slope and a substantial reduction of local lift was observed using this correction. Furthermore, the direct influence of the sectional image vortices on the neighboring segments is included using the intermediate 3D image method. Finally, a full 3D image method was presented which includes the complete downwash effect of the jet boundary. To validate the three 3D potential flow methods, again CFD simulations were performed and the setup is presented in this chapter. In Section 9.1 the computational domain of the simulations is discussed. The explanation of the used grid is done in Section 9.2.

9.1. 3D CFD Computational Domains

For the 3D CFD analyses, a similar approach was followed as for the 2D simulations. Ansys CFX was used and the turbulence model was set to the laminar model. The viscosity was set to a very low value to approximate the inviscid flow assumption of the potential flow tools. In Section 9.1.1, the information regarding the circular jet is presented. For the validation of the intermediate 3D image method, two more simulations were performed using a rectangular jet. In Section 9.1.2 and 9.1.3 the domains with the infinitely wide and infinitely large rectangular jet are discussed respectively.

9.1.1. Circular Slipstream

For the domain of the 3D simulations, a box was created with the wing in the middle of the domain. The wing modeled is a straight NACA 0012 wing with no taper or dihedral. The aspect ratio for this analysis was set to 10, meaning the span is 10 times the value of the chord for the straight wing. The α is set to be 2° and no twist was applied. The domain can be schematically seen in Figure 9.1. Unfortunately, the simulations of the potential flow need a large number of mesh cells to avoid numerical viscosity, as is discussed in Section 5.3. This gives limitations to the possible sizes of the domain, otherwise, the number of cells gets too large. The domain was modeled to have the inlet and outlet planes $10c$ away from the wing. Also, the top and bottom boundaries were placed at this distance from the center point. The wing tips are both placed at $5c$ from the center and it was decided to place the side boundaries at $25c$ from the center.

The propeller slipstream was modeled as a circular inlet plane in the middle of the freestream inlet. For the simulations, it was decided to use an h/c of 2, such that the reduction in lift is clearly present, while the numerical errors of small slipstream heights are omitted. Both the inlet planes were modeled as a velocity inflow condition and the outlet was modeled as a static pressure outlet. The four sides and the wing were modeled as free slip walls to avoid viscosity effects while maintaining the zero normal velocity condition. Two different jets were simulated, namely with $V_j = 1.5V_\infty$ and $V_j = 2V_\infty$.

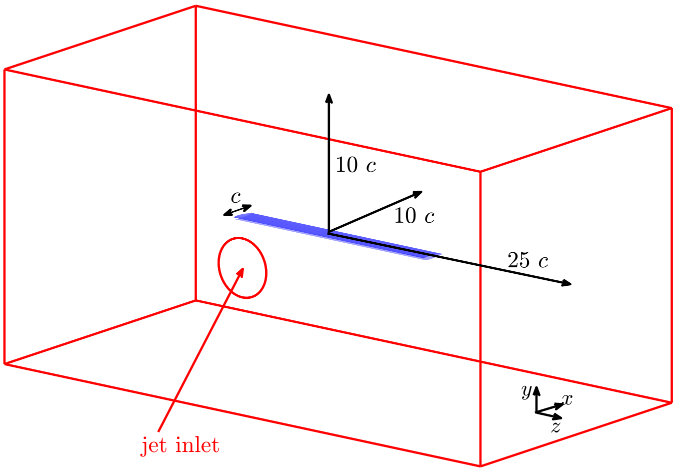

Figure 9.1: 3D computational domain including the circular propeller inlet

The full 3D domain with the complete wing was modeled, in contrary to only halve of the wing, since also a non-symmetric case and a simulation including swirl were performed. For the non-symmetric case, the propeller inlet plane was moved to one side of the wing and was centered at the middle of the semi-span. For the simulations including the slipstream swirl component, a tangential velocity profile was specified on the jet inlet plane. A sine function was used to define the swirl velocity along the radius of the propeller slipstream, since this was easy to define and this distribution comes close to the swirl component profile from the BEM analysis.

9.1.2. Spanwise Jet

The intermediate 3D image method, using the 2D sectional images and their influence on all spanwise sections is checked using a simplified flow problem. The case modeled in this section is that of a wing submerged in a spanwise jet with finite height. The wing is the same as the one used in previous analyses, namely the straight NACA 0012 wing with $AR = 10$. The wing has an angle of attack of 2°. The slipstream is modeled as a constant velocity jet and $V_j = 1.5V_\infty$. The computational domain is shown in Figure 9.2. The jet inlet plane was altered to have the spanwise jet and this plane spans the whole width of the domain. The height of the jet was taken to be equal to the diameter of the previously analyzed circular slipstream, hence $h = 2c$.

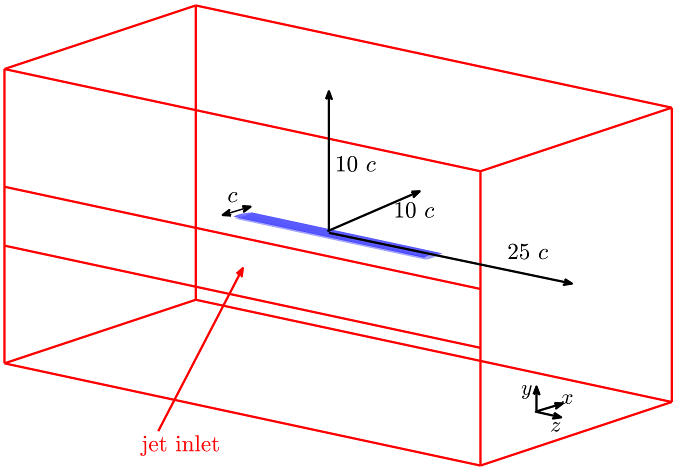

Figure 9.2: 3D computational domain including the spanwise jet inlet

9.1.3. Vertical Jet

To see the influence of the horizontal dimension of the jet and hence the lack of modeling using only vertical images in the intermediate 3D image method, the infinitely large jet but finite in width is modeled. The case is the same as presented before, namely the straight NACA 0012 wing with $AR = 10$ and $\alpha = 2°$. The slipstream is modeled as a constant velocity jet and $V_j = 1.5V_\infty$. Similarly to the case with a spanwise jet, the inlet plane was changed to allow for the vertical jet, see Figure 9.3. For the potential flow, it is assumed that the height of the jet extends from $y = -\infty$ to $y = +\infty$. The jet was modeled to have a width equal to the diameter of the circular slipstream and hence the same value as the height of the spanwise jet, namely $2c$.

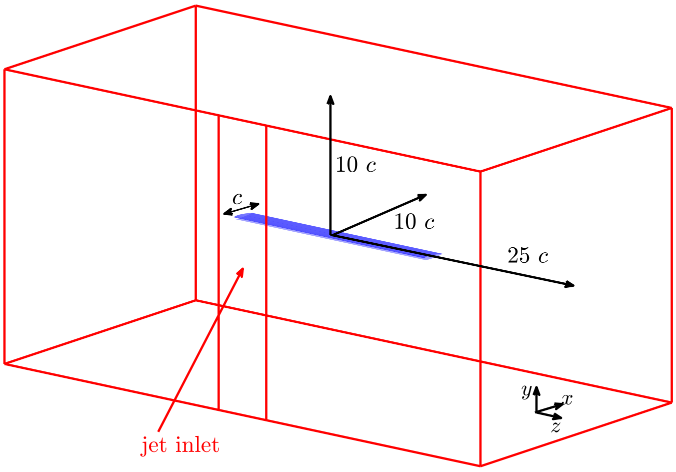

Figure 9.3: 3D computational domain including the vertical jet inlet

9.2. 3D Mesh

For the grid of the 3D simulation, a very large number of cells was needed. The mesh was generated using ICEM CFD and an unstructured mesh was set up. To perform a grid dependency study, multiple meshes were created by varying the maximum grid sizes on both the domain boundaries and the wing surface. The maximum size of the mesh cells on the wing was varied from from 0.1 to 0.005. The maximum mesh size in the domain was varied from 0.75 to 0.1. This resulted in eight different grids and their characteristics are shown in Table 9.1. For the gird dependency study, the previously discussed wing was analyzed at a freestream velocity of 100 m/s. The jet was not modeled in the mesh dependency study to ease the convergence of the simulations.

Table 9.1: Overview of the wing mesh size and volume refinement dimensions for the mesh dependency study including the generated lift value

Grid	Wing refinement [c]	Volume refinement [c]	Total number of nodes	total lift [N]
1	0.01	0.25	20,756,624	4646
2	0.01	0.1	144,955,296	4641
3	0.01	0.5	5,298,635	4654
4	0.01	0.75	3,346,721	4657
5	0.1	0.5	1,189,180	3506
6	0.05	0.5	1,292,046	4202
7	0.005	0.5	14,203,839	4547
8	0.005	0.25	30,878,635	4546

The integral lift value of the wing was used to determine the convergence of the used meshes. As can be seen, the wing refinement is the most important aspect of the grid generation, since grid 1 to 4 show good agreement which each other, while the variation of volume refinement has less of an influence on the lift value. When the grid size on the wing surface is increased, there is a significant change in lift value and therefore grid 5 and 6 were deemed to be too coarse. The grid dependency study was only performed for the case without jet. So the convergence might be different when the jet is added to the simulations. In the end, it was chosen to use grid number 1 in the validation simulations since this grid is a good compromise between accuracy and computational cost. To be sure that the simulations of the jet showed a converged result, an extra density region was applied in the slipstream. For the simulations of the rectangular jet, the same mesh was used, but without the density region, since this would result in too many cells. To be sure that the mesh was fine enough for the simulation of the slipstream, the flow field was investigated after the simulations and the development of the jet was inspected. In the next chapter, the results of the adjusted LL, the intermediate 3D image method and the full 3D image method are presented and compared to the results of the 3D simulations.

10

Results of the 3D Propeller-Wing Analysis

Three different potential flow methods were defined in Chapter 7 and 8, which correct the spanwise lift distribution of the wing for the effect of the slipstream boundary. These methods needed to be validated using CFD simulations. In Section 10.1, the computational cost of the three correction methods is discussed. The results for the LL method are presented in Section 10.2. The results of the potential flow analysis and the CFD simulations for the intermediate 3D image method using a single panel VLM is presented in Section 10.3. The results of the full 3D image method, as presented by Rethorst, are discussed in Section 10.4. To conclude this chapter, the full analysis of a propeller slipstream, including the swirl component, is discussed in Section 10.5.

10.1. Numerical Model Execution Time

For the use of the potential flow methods discussed in for example an optimization framework, the execution time can be an important factor. In this section, a short overview is given of the three 3D correction models regarding the time it takes to analyze a propeller-wing problem. A total of 100 spanwise segments was used for the three tools. In Table 10.1, the results are shown. Analyses were performed with and without the correction techniques. So for the adjusted LL, the analysis without correction is just the conventional LL calculation. For the intermediate and full 3D image method, the basis is the single panel VLM and therefore, their execution time without image correction is the same.

Table 10.1: Execution times for the three potential flow methods with and without the correction for the slipstream boundaries using 100 panels

Method	Execution time [s]	
	without correction	with correction
Adjusted LL	0.04	1.41
Intermediate 3D	0.32	0.35
Full 3D	0.32	26.77

As can be seen in the table, the LL tool shows the shortest execution time if no correction is applied. However, once the 2D Ting correction method is applied at each segment in the propeller slipstream, the computational time is increased. For the intermediate 3D image method, the computational time is only increased marginally, since the images are simply added to the total system of horseshoe vortices. This means that the intermediate 3D image method is quicker than the adjusted LL tool. The 3D full image method is considerably more expensive computationally wise when the image corrections are applied and this is caused by the nested integrals as discussed in Section 8.3.2.

10.2. Results of the LL Method

In this section, the results of the adjusted LL tool are presented and compared to the CFD data. The resulting pressure field over the wing was used to determine the lift distribution. This was done by defining chordwise contours and integrating the pressure along these. The 3D CFD results of simulations with and without jet are shown in this section. For the case with the jet, the velocity in the slipstream was set to $V_j = 1.5V_\infty$ and $R_p = 1c$, meaning a maximum of $h/c = 2$. First, the wing without propeller slipstream is discussed in Section 10.2.1, after which the case of an axial jet is discussed in Section 10.2.2.

10.2.1. No Slipstream

For the case where no slipstream is present, the CFD data can be seen as a validation of the LL method. Note that the results from the LL tool are based on the thin airfoil theory and hence the thickness of the wing is not taken into account. For the NACA 0012, the thin airfoil C_{l_α} value is simply equal to 2π, while for the 2D panel method, the C_{l_α} is close to 6.9. This means that for the 2D thin airfoil case, a correction of 1.09 has to be applied on the sectional lift to account for the thickness. Unfortunately, as discussed in Section 7.2.1, this thickness correction coming from the panel method compared to the VLM (using XFLR) is dependent on the aspect ratio of the wing and it is not simply equal to the ratio of lift in the 2D case. Only for an infinitely wide wing, this thickness correction approaches that of the 2D case. The C_l distribution along the span for both the LL tool and the CFD analysis without the jet can be seen in Figure 10.1a.

The maximum local lift coefficient is higher for the CFD data, as is expected due to the thickness of the wing. To correct for this difference, a single correction value is determined, such that the LL shows a good agreement with the CFD data. In this way, the difference in C_l obtained from both methods for the analysis including the slipstream can be assumed to be only from the 2D correction method. The thickness correction of the CFD data was determined to be 1.06. This value might seem arbitrary, but in Figure 10.1b, the lift distribution is shown for the LL and VLM technique including this newly defined thickness correction factor and the data of the VLM is matching that of the CFD analysis quite precisely. This correction factor was applied to the LL code to ensure better comparison between the tool and the CFD simulation results in the coming sections.

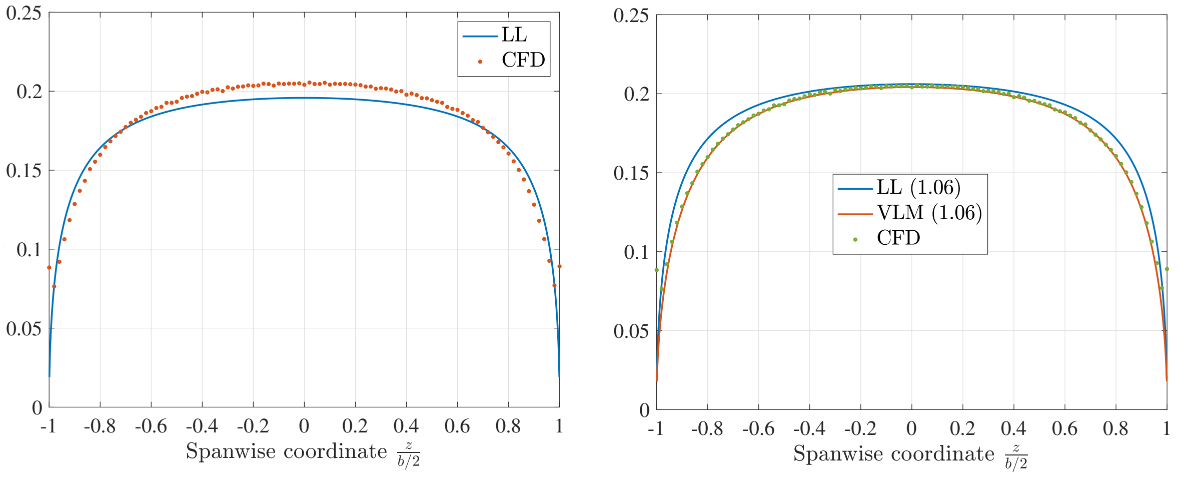

(a) Comparison of the LL tool and the CFD analysis

(b) Comparison of the LL tool, VLM and CFD analysis including the thickness correction

Figure 10.1: Spanwise C_l distribution for the case without slipstream

10.2.2. Circular Propeller Slipstream

To validate the use of the 2D correction method in the LL tool, the axial propeller slipstream analysis was performed. As described in Section 9.1, the slipstream was modeled as a circular jet, only having an axial velocity increase compared to the freestream inlet conditions. The analysis with the adjusted LL tool and the CFD simulations were performed for $V_j = 1.5V_\infty$. For the analysis using the LL tool, 1000 panels were used, of which 200 inside the slipstream. This was found to be in the asymptotic region of the convergence trend. Also, the thickness correction factor was applied to the analysis and this was implemented by changing the C_{l_α} of all sections. The results can be seen in Figure 10.2a, where the original LL solution is shown, together with the corrected lift distribution, created by both methods as discussed in Section 7.3. The lift distribution of the CFD simulation was determined by the integration of the pressure and is normalized using V_∞ at every section, similar to the definition used in the adjusted LL.

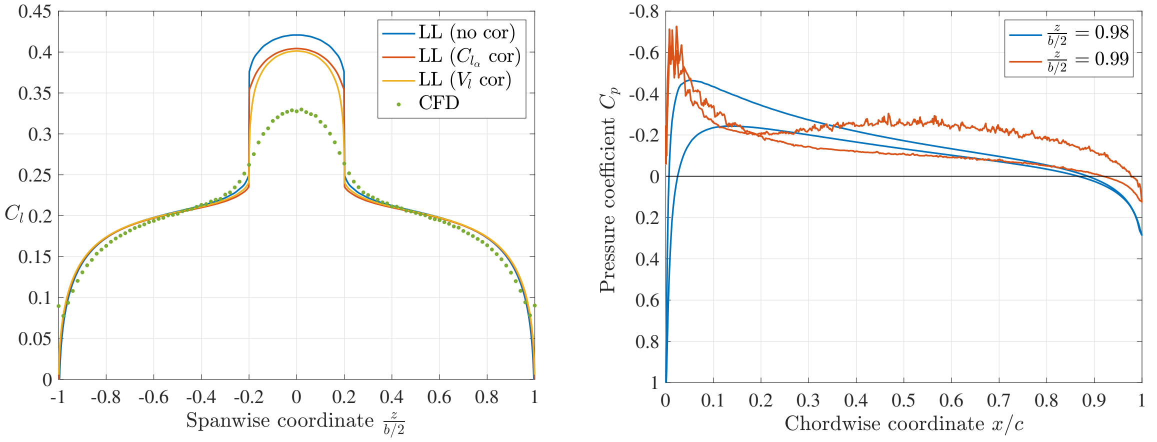

(a) Spanwise C_l distribution comparison between the LL and CFD

(b) Chordwise C_p distribution for two locations close to the tip

Figure 10.2: Results of the analysis of a wing with a circular axial jet in the middle

As can be seen, the lift outside the slipstream is modeled properly using the LL model. At the tips, there is a sudden spike of lift in the CFD simulation that is not present in the LL analysis. The lift should go to zero near the tips because of the pressure equalization. However, this peak is caused by the local impingement of the tip vortex. The tip will increase the pressure locally on the top side, since the vortex runs from the lower surface to the top surface [54]. This is a very local effect and does not influence the lift distribution away from the tip. To check this phenomenon, the C_p distribution along the chord contour for two locations close to the tip is shown in Figure 10.2b. The pressure distribution at $^{z}/_{b/2} = 0.98$ looks like a normal distribution as is expected from an airfoil, but slightly closer to the tip, the pressure distribution looks very irregular due to the tip vortex.

Unfortunately, there is a very large discrepancy between the results computed with the adjusted LL and the CFD simulation results for the lift values inside the slipstream. This suggests that the 2D correction method is insufficient to capture the 3D effect of the slipstream. The method of applying 2D corrections at each spanwise station in the LL tool to correct for the local slipstream height does not seem to predict the correct lift distribution. The use of the KJ theorem was validated in Section 6.3.3 and it turned out that for contours close to the airfoil, the circulation seems to match the value of the theoretical potential flow. The flaw is probably in the fact that at each section, only the influence of the slipstream is taken into account on its own circulation and not that of the neighboring sections. Therefore, it might improve the method if the image procedure is expanded to 3D to include the effect of the images on each panel. The results of the intermediate 3D image method are discussed in the next section.

10.3. Results of the Intermediate 3D Image Method

The intermediate 3D image method, which makes use of the single panel VLM, is used to analyze the wing with a circular jet in the middle, as was done in previous analyses for the adjusted LL tool. Furthermore, to test the applicability of this method, two cases of a rectangular jet are modeled. The first one is a wing submerged in a spanwise jet with finite height and the second case is with a jet which is limited in width but has a large height.

10.3.1. Circular Propeller Slipstream

The LL tool showed large discrepancies compared to the CFD results for the sectional lift values in the jet. In Figure 10.3, the results of the intermediate 3D image analysis are shown, including the data from the LL method to see the difference with this new VLM method. There is a noticeable difference between the adjusted LL and the intermediate 3D image method. This also confirms the need for taking the 3D effects of the images into account in the analysis of the wing. However, the region outside of the jet is also altered and the C_l here is lowered compared to the adjusted LL method. Unfortunately, the reduction in local lift is still not sufficient to come close to the CFD data, but this VLM image method seems more promising compared to the LL method using 2D corrections. As already presented in Section 7.2.1, the VLM method shows a slightly different trend towards the tips compared to the LL method. This is confirmed again and the C_l values of the CFD show a better agreement near the tips with the VLM.

Both the LL method and the VLM use images to correct for the local height of the slipstream, which is not infinite compared to the potential flow assumptions. Apparently, only correcting for the vertical dimensions of the jet is not sufficient and hence the horizontal dimensions should be taken into account. To check the influence of the horizontal finiteness of the jet in this method, two simplified cases are simulated. As a consequence, the jets are of a rectangular shape and will be physically more comparable to an open-jet windtunnel flow than a propeller slipstream. The results of the spanwise jet will be presented in Section 10.3.2, while the infinitely high jet is modeled in Section 10.3.3.

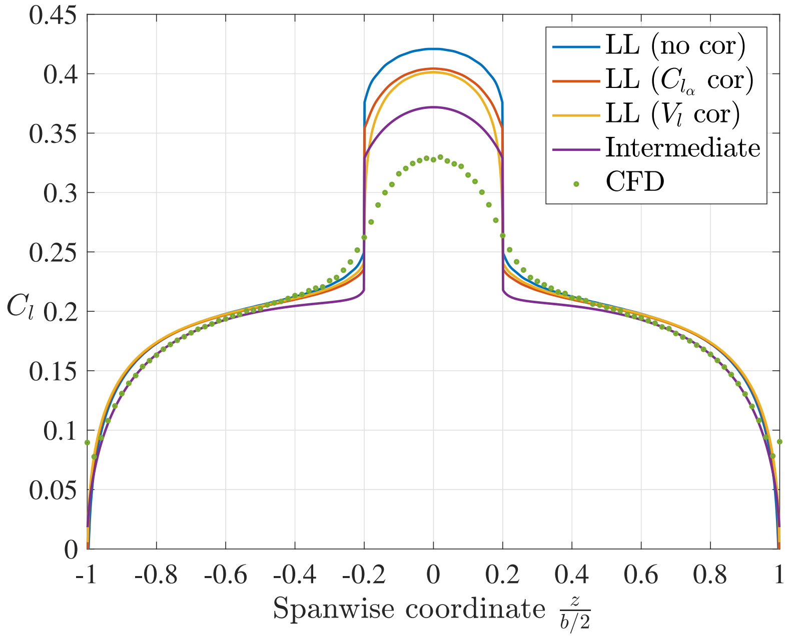

Figure 10.3: Comparison of the LL and VLM methods with the CFD data for a circular slipstream

10.3.2. Rectangular Spanwise Jet

The analysis results of both the adjusted LL and the intermediate 3D image method, and the CFD data are presented in Figure 10.4. This analysis was done for $V_j = 1.5V_\infty$. The data of the LL are also presented, to see the difference between the two potential flow methods. The data of these two are generated using 1000 spanwise panels to ensure a sufficiently accurate distribution. Note that the C_l is defined again by using the lift from the KJ theorem and non-dimensionalized using the freestream conditions. The blue line represents the original LL solution, where no correction is applied. This is equivalent to a wing with $V_\infty = V_j$ since each station is inside the slipstream. When the 2D image method is applied to correct for the local C_{l_α}, there is a constant correction, since the height is constant along the span. The 2D image correction method shows a reduction in local sectional lift. By using the other correction method, for the local velocity, there is a small difference with the former correction, but this is less than 1%.

What is important to see is that the lift data of the CFD analysis is substantially lower than the data from the adjusted LL method, confirming once again that this 2D correction method is not sufficient to capture the 3D effects. However, the CFD data matches the intermediate 3D data quite accurately, which seems to confirm the correctness of the intermediate 3D image method. Note that the same thickness correction factor as defined in Section 10.2.1 was used for the data of the intermediate 3D image method and the adjusted LL method. This simplified analysis is only applicable when the complete wing is submerged in a jet of constant height, which is not often encountered in reality.

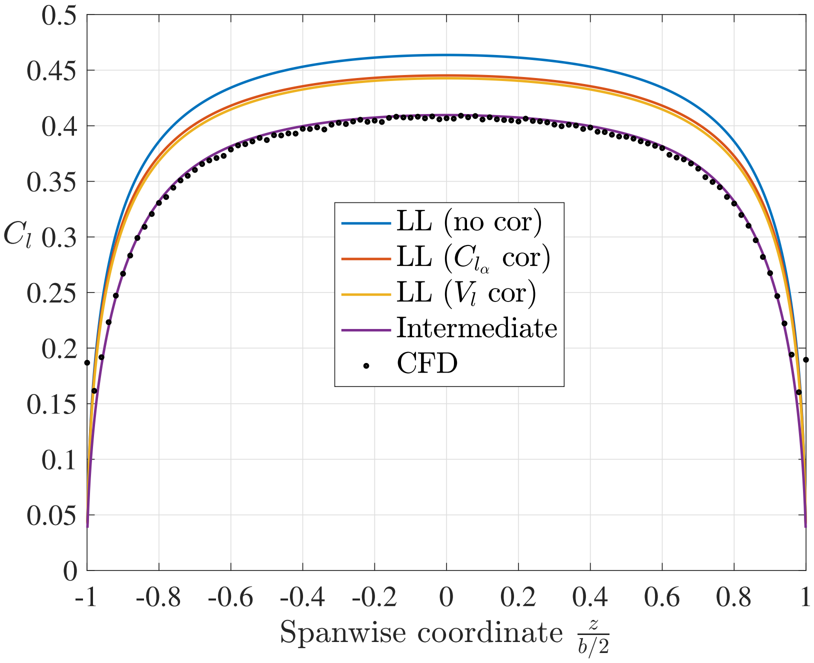

Figure 10.4: Comparison of the LL and VLM methods with the CFD data for a rectangular spanwise jet

10.3.3. Rectangular Vertical Jet

The results of the analysis of the vertical jet are shown in Figure 10.5. A total number of 1000 panels was used for the analysis and since there is no correction factor, only a single LL result is shown. The same jet velocity ratio was used as before, namely $V_j = 1.5V_\infty$. The lifting-line shows the same trend as before, since the circular jet modeled had the same width. As can be seen, the VLM (without images) predicts the lift coefficient to be slightly lower inside the jet compared to the LL method. This is due to the inherent difference between the two methods. For the CFD analysis, the results of both the original (circle) and the new rectangular jet (full) are shown. The lift distribution of the latter is higher as expected since the slipstream is not limited in the vertical direction.

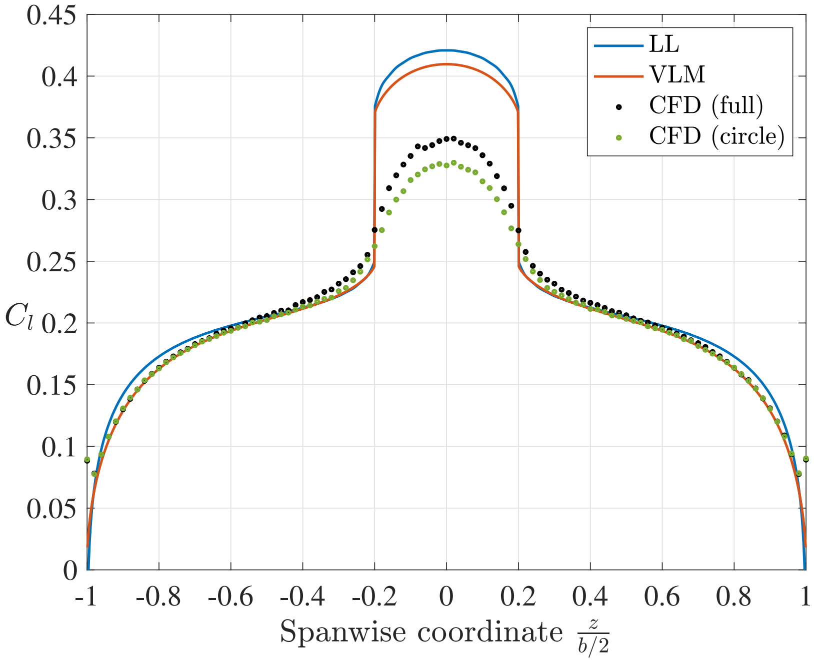

Figure 10.5: Comparison of the LL and VLM methods with the CFD data for a rectangular vertical slipstream

As clearly can be observed, the horizontal boundary of the jet heavily influences the lift distribution, since the analysis results of the potential flow tools are showing a large discrepancy with the CFD data for the infinitely high jet. If the adjusted LL and intermediate 3D image method would work using only 2D vertical images, the data of the potential flow and CFD would match, since there is no need for height corrections. This is not the case, confirming the need for the full 3D image method.

10.4. Results of the Full 3D Image Method

The full 3D image method, which makes use of the even and odd horseshoe vortex systems, was analyzed and the data were compared for the case of a circular jet. This was done for two different velocity ratios. The first analysis was done for the same case as discussed before, namely that of V_j=1.5V_∞. The results can be seen in Figure 10.6. As can be seen, the full 3D image method shows a remarkably good agreement with the CFD data. This is a large improvement compared to the other two potential flow methods, which largely over-predicted the sectional lift coefficient. Note that the thickness correction factor was applied again.

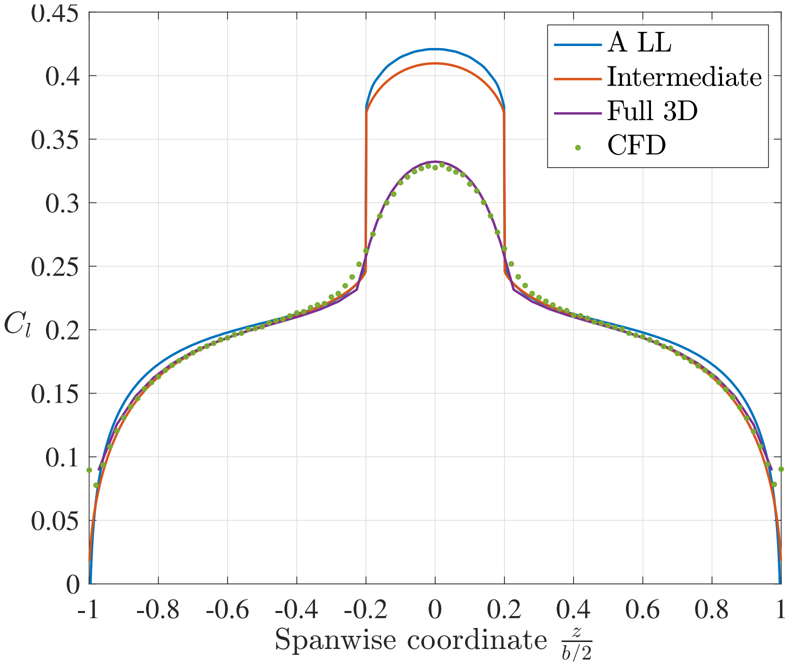

Figure 10.6: Comparison of the three different potential flow tools with the CFD data for a circular slipstream

The full 3D image method seems to work for this specific case of propeller-wing interaction. To further check the correctness of the method and to see if it is not limited to lower velocity ratios, another jet velocity was analyzed. The second CFD simulation which was performed for the circular jet was that of V_j=2V_∞. To clearly see the results of this analysis, the data created by the LL and intermediate VLM method are left out of the figure. The results of this second analysis are shown in Figure 10.7. As can be seen for this velocity ratio, the full 3D image method seems to be correct and the discrepancy between the potential flow tool and the CFD data is small. This confirms the correctness of the method and the need for a full image method instead of the adjusted LL or the intermediate 3D slipstream corrections. Furthermore in this figure, the results of the full 3D image method are shown in which only the even image system is taken into account. As can be seen, the difference with the addition of the odd system is large and this confirms the need for the odd image system.

Unfortunately, the full 3D image method is limited to circular jets, with constant axial velocity throughout the jet, similar to the 2D image method. The method is computationally the most expensive, but the running time is in the same order of magnitude as the other two methods and hence the use of the full 3D image method seems to be the only right one. The results from this method also seem to confirm the statements made regarding the physical incorrectness of the empirical correction methods, as discussed in Section 3.3. In the full 3D image method, the local velocity was used for all the calculations, also in the KJ theorem, and hence the use of V_∞ is incorrect for calculating the sectional lift coefficient.

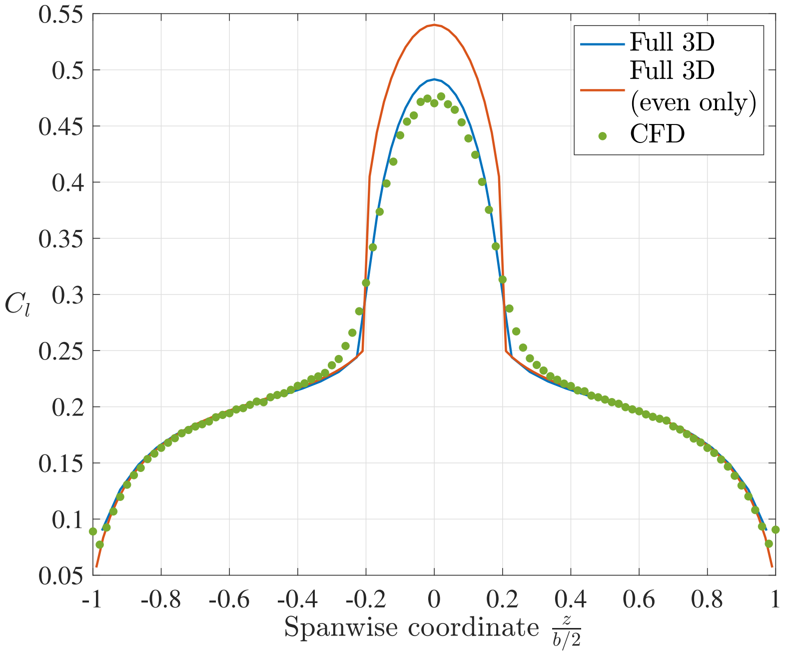

Figure 10.7: Comparison of the full 3D image method with CFD for $V_j = 2V_\infty$

The 3D image method seems to predict the propeller-wing interaction well and the sectional lift is reduced significantly compared to the conventional analysis approach without any corrections. However, the full 3D method was based on the assumption of a symmetric propeller-wing problem, meaning that the slipstream is centered in the middle of the wing. This poses a large limitation on the method, but the influence of the image correction was found to be small, as discussed in Section 8.4.3. In the section, a new approach was formulated to analyze non-symmetric cases. This method was also validated using CFD and therefore, the jet inlet was placed in the middle of the semi-span, meaning at $z = 0.25b$, instead of the center of the domain. The results of this non-symmetric analysis are shown in Figure 10.8.

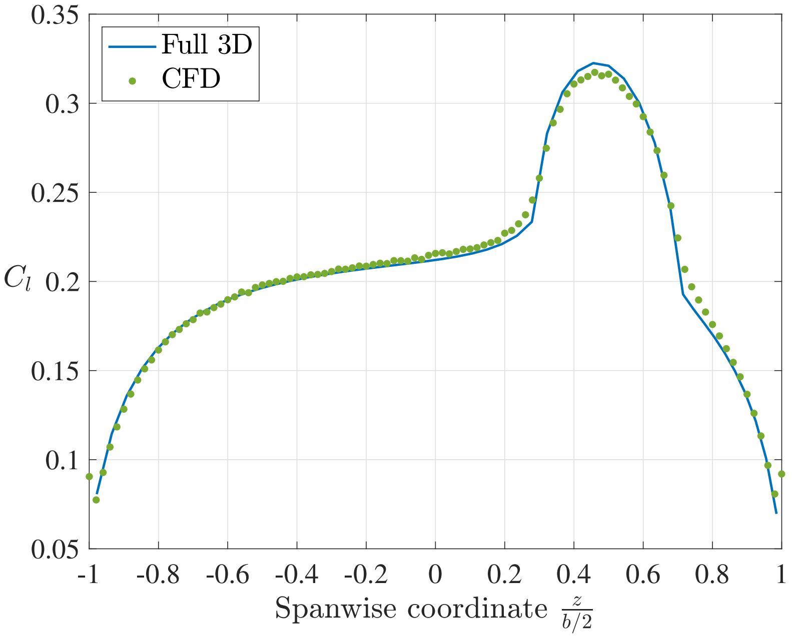

Figure 10.8: Comparison of the full 3D image method with CFD for a non-symmetric propeller slipstream case

Again, the full 3D image method seems to accurately predict the propeller-wing interaction, since the discrepancy with the CFD data is small. This means that the symmetry condition is not necessarily needed in the analysis. This increases the usability of the method and means that the 3D image method can be used for more propeller-slipstream cases than just the symmetrical case. However, the method is still limited to the assumption of a constant jet velocity throughout the slipstream. Furthermore, the current analyses were performed using a single jet. It is uncertain if the modeling of multiple propeller slipstreams can be done using this method and this should be investigated for future work. The three presented potential flow methods all have a single shortcoming in common. The propeller swirl is not included in the analysis. To see the effect of including the swirl component to the 3D full image method, a final CFD simulation was performed, which includes the tangential velocity component in the slipstream.

10.5. Propeller Slipstream including Swirl

The three potential flow tools in this thesis corrected the local lift of each wing segment submerged in the slipstream only based on the induced axial velocity component in the slipstream. To see the effect of not applying a correction to the swirl component, the full 3D method was adjusted to take this swirl into account and the results were compared with the data of a CFD simulation. The swirl was added in the full 3D method similarly as is done in existing tools. In the theory of the adjusted LL method, see Section 7.1, it is explained how the swirl is 'simply' added as a change in local angle of attack. The swirl component was modeled with a sine function since this was easy to implement and comes close to the results obtained from the BEM technique. The maximum tangential velocity at the peak of the sine wave was set to 5 m/s, which is a fraction of 0.05 of the freestream velocity. The results of the full 3D method and the CFD simulation can be seen in Figure 10.9.

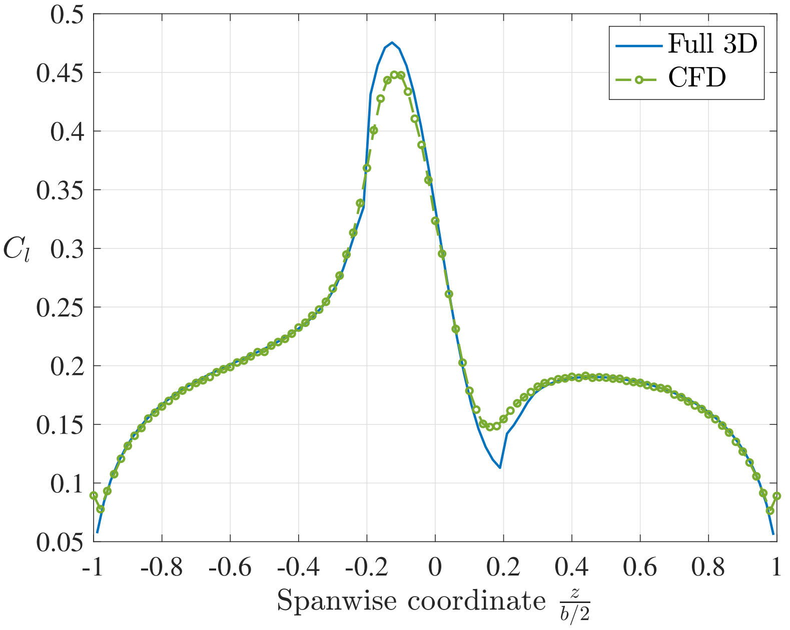

Figure 10.9: Comparison of the full 3D image method with CFD including the swirl component in the slipstream

The results of the full 3D method show a reasonable agreement with the data from the CFD simulation. As can be seen, the effect of the swirl is slightly over-estimated by the full 3D tool, since the lift is over-predicted behind the up-going blade side while it is under-predicted behind the down-going blade side. This seems to confirm the hypothesis that also the swirl component of the flow must be corrected to account for the effect of the finite slipstream height on the lift distribution. More research should be performed to define this correction method for the swirl component and is therefore a recommendation for the future.

To conclude this chapter, the 3D image method improves the modeling of the propeller slipstream and its effect on the lift distribution of the wing. Using the 2D images in 3D, the images of one section also directly introduce a downwash on the neighboring sections. For the circular jet however, the difference between the intermediate 3D image method and the CFD data was still substantial. To further check the applied method, a spanwise jet was modeled, such that only the vertical dimension of the slipstream is finite and needed correction. This showed a remarkably good agreement with the presented CFD data confirming the need of a 3D image system instead of only 2D sectional corrections. The flaw of the presented intermediate method is the fact that it only corrects for the vertical slipstream dimension and not for the influence of the horizontal boundaries. This is confirmed by the second rectangular jet analysis, being infinite in height. This flow case would result in no correction in the potential flow tool since the vertical images are placed infinitely far away. However, the CFD does not show a match with the data of the intermediate 3D image method and hence the need for images in the horizontal planes.

The use of the full 3D image method as described by Rethorst resulted in a very good agreement between the potential flow tool and the CFD data for an axial jet, confirming the need to include the horizontal influence of the slipstream boundary. The images were placed at the inverse of the spanwise position and the horseshoe vortices were split in an even and odd system. The equations of the method were defined for the case where the jet is located at the center of the wing. However, since the influence of the slipstream boundary is concentrated in and around the jet, the image can be enhanced to analyze non-symmetric cases. This analysis showed also a very good agreement, even though the equations were not derived for this case. However, the results of the CFD simulation also showed the need for the odd vortex system, since the use of only the even system largely over-predicted the lift compared to the complete method. Finally, a CFD simulation including the swirl component in the slipstream was performed to see the effect of simply adding the swirl component to the wing analysis, as is done in conventional wing analysis tools. The possible discrepancy between the 3D full image method and the CFD data by not applying a correction method to the swirl component was investigating . It turned out that the full 3D image method slightly over-predicted the effect of the swirl component, but that this was reasonably small. To fully model the effect of the finite slipstream dimensions on the lift distribution of the wing, a correction method must found which can be applied to the swirl component.

11

Conclusions and Recommendations

This chapter finalizes the thesis with the conclusions in Section 11.1 and the recommendations for future work in Section 11.2.

11.1. Conclusions

The high propulsive efficiency of propellers makes them attractive to reduce fuel consumption of aircraft even further, especially with the ongoing research into electrification of aircraft and the use of distributed propulsion. The flow behind the propeller has an increased axial velocity compared to the freestream. Furthermore, the rotation of the propeller introduces swirl into the propeller slipstream. From the propeller slipstream analysis, it was concluded that the slipstream will influence the lift aerodynamics and vice versa. However, for this thesis, only the interaction of the propeller on the wing was taken into account, since the emphasis was put on the improvement of existing wing analysis tools.

Most of the propeller-wing analysis tools are based on potential flow assumptions. The simplest analysis tool is the lifting-line method, which is only usable for straight and unswept wings and therefore limited in application. From the implementation of the method, it turned out that the 2D sectional aerodynamics are easy to be altered. To model more complex wings, including sweep, dihedral and taper, the vortex lattice method can be used. This method makes use of a lattice of horseshoe vortices and the boundary condition of zero normal velocity must be satisfied at each control point. From literature review of existing tools, it turned out that the axial component is simply included in the freestream velocity and the swirl component is modeled as a vertical velocity component resulting in a change of local angle of attack, similar to the effect of the created downwash by the horseshoe vortices.

Unfortunately, large discrepancies are found between the analysis results of the existing potential flow tools and high-fidelity validation data such as from CFD analyses and wind tunnel experiments. This is due to the simplifications made in the addition of the slipstream induced velocities in these tools. The stripwise approach does not account for the relative position of the wing segment in the propeller slipstream. A segment at the edge of the slipstream experiences a different flow field than one in the middle of the slipstream, due to the different relative height of the slipstream at the different spanwise positions. All segments submerged in the slipstream are assumed to have an infinitely large jet, but in reality the local lift is influenced by the proximity of the slipstream boundaries. Especially for small slipstream heights, the lift increase is heavily over-predicted by assuming an infinitely large jet. This over-prediction must be corrected for and this was done using a potential flow technique known as the image vortex method. In this thesis, three different 3D correction models were developed which can be applied to the existing wing analysis tools.

Firstly, a correction method for the 2D sectional lift of an airfoil submerged in a jet of finite height was defined, since the lifting line model is based on a 2D strip approach. On these wing segments, the Kutta-Joukowski theorem is used to calculate the local lift. Since the velocity used in this theorem is independent of the slipstream height, the correction method must reduce the produced local circulation. The approach taken is similar to that found in wind tunnel wall correction methods. A system of reflected images is created, where the dividing streamlines are the reflection planes. By solving the resulting system of linear equations, a Fourier coefficient representation of the airfoil distributed vorticity is calculated. The integrated circulation can be used to recalculate the lift created by the airfoil and to find the difference compared to the case of an infinite slipstream height. From the results of this 2D tool, it is concluded that at low values of h/c, the lift coefficient of the airfoil is reduced significantly compared to the conventional approach of assuming an infinitely high jet. Unfortunately, this method is limited to thin airfoils and the determination of the airfoil position in the jet must be defined locally, meaning the solution is not valid far from the airfoil. The potential flow correction method does not take the swirl velocity in the slipstream into account and hence, the swirl will be modeled as a vertical velocity component as is done in existing tools.

This 2D airfoil analysis tool that corrects for the influence of the propeller slipstream on the sectional lift was validated using CFD simulations. A square domain of 100 chord lengths was used to minimize the effects of the boundaries on the simulation. Furthermore, a fine mesh was needed to reduce the effect of numerical viscosity, especially to prevent the diffusion of the jet boundary. The data from the 2D CFD analyses showed good agreement with the potential flow analysis result, validating the presented method of image vortices. From the CFD results, it was further concluded that the pressure distribution over an airfoil, which is submerged in a jet with a small height, shows the reduction in generated lift and the main effect of the slipstream is observed in the reduction of the suction peak at the LE. Furthermore, the analysis of the 2D circulation around the airfoil confirmed the correctness of the Kutta-Joukowski theorem, as long as the contours are maintained within the jet.

The validation of the 2D correction method showed a right implementation of the image vortex technique. The first step towards a 3D analysis tool which included the mentioned sectional lift correction was to adjust the lifting-line method. For each 2D segment of the wing in the slipstream, the local slipstream height can be determined and the 2D analysis method can be applied to correct the local sectional lift. So this adjusted LL tool only takes the influence of the images into account in the 2D strip analysis and the influence of the finite slipstream height on neighboring sections is indirectly accounted for due to the decrease in produced downwash. Unfortunately, this simple 2D correction did not provide the correct lift distribution and still a large discrepancy between the CFD data and the potential flow analysis tool was present. It was concluded that this was due to the fact that the influence of the image vortices on neighboring segments was not taken into account and this was the motivation to expand the image method into 3D.

To overcome the shortcomings of this 2D correction method applied in the LL tool, the image approach was applied in 3D. The image system of each 2D section was now added to the complete 3D horseshoe lattice. In this way, the influence of the slipstream boundaries is experienced by all the wing segments, since the produced downwash of the images is added to the lattice of horseshoe vortices. The positions of the images were however still determined by the 2D slipstream height. It turned out that this intermediate 3D image method was actually computationally less expensive than the adjusted lifting-line method, and also produced slightly better results compared to the adjusted lifting-line. However, the decrease in over-prediction compared to the adjusted lifting-line was not substantial and still a large over-prediction was present compared to the CFD data. From analysis of the CFD results, it was concluded that this method is still insufficient in modeling the complete 3D effects of the slipstream on the wing. The shortcomings of this intermediate method were emphasized by the analysis of a rectangular jet of finite width, but with an infinite height. This hypothetical jet would not result in any image corrections, since the vertical slipstream boundary is infinitely far away. However, the results of this analysis also did not show agreement with the results of a similar CFD simulation.

The third and most complicated slipstream correction method was the full 3D image method. The method is based on the fact that a horseshoe vortex can be split up into an odd and even part. The even part is similar to the 2D approach, but the images are placed at the inverse spanwise location to satisfy the boundary conditions of equal pressure and continuity along the slipstream boundaries. So the images are no longer placed in the vertical direction. However, the height of the slipstream still influences the results through the selected approach to position the image vortices. The difference with adjusted lifting-line and the intermediate 3D image method is that the effect of the bound vortex part on the disturbances of the slipstream must be taken into account. The odd system represents this effect, but also adds complexity to the method. The results of this third correction method showed remarkably good agreement with the CFD simulations and the method overcomes the shortcomings of the adjusted lifting-line and the intermediate 3D image method. From the analysis of the results, it was also concluded that the removal of the odd part resulted in a significant decrease in lift correction and hence an increase again in over-estimation. This means that the complicated odd system can not be neglected as was done in previous studies. The full 3D image method also seems to work for a slipstream which is not in the middle of the wing. This increases the usability of the approach significantly, since the equations used were derived based on symmetry conditions.

The equations of the full 3D image method were based on the assumption of symmetry, meaning the method would be limited to the propeller-wing analysis where the slipstream is centered in the middle of the wing. Fortunately, from the sensitivity analysis, it was concluded that the influence of the propeller slipstream is concentrated in and around the jet, meaning that the observed downwash from the slipstream quickly becomes negligible when moving away from the slipstream. This allows for the analysis of non-symmetrical cases and the CFD data showed that his enhanced method indeed also showed a good agreement. So even though the full 3D image method is computationally much more expensive than the other two correction methods, it is concluded that this is the only correction method that can produce accurate results.

The three potential flow methods, which correct for the slipstream boundaries, were all based on the addition of the axial slipstream component only. No correction method was found that can be applied to the swirl in the slipstream. From the CFD simulation including propeller swirl, it was concluded that the analysis results showed a small over-prediction of the effect of the swirl component in the lift of the wing. This means that the wing segments behind the up-going blade showed an over-prediction of lift coefficient, while the wing segments behind the down-going blade showed an under-prediction of the lift coefficient. It is suggested that a potential flow method to correct the swirl component is found to improve the full 3D method even further.

To conclude, the finite dimensions of the propeller slipstream result in a decrease of local lift of each wing segment submerged in the slipstream compared to the existing approach of assuming infinitely high slipstream heights. The effect of the finite height and width of the propeller slipstream on the wing lift distribution is based on the introduction of images in the flow. The use of these images results in a correction model that can be applied to the existing potential flow methods. This correction tool corrects the axial flow component of the propeller slipstream, but not for the finite extent of the swirl velocity. The use of the full 3D image method provided a good agreement with CFD simulation data and hence can be used in future propeller-wing interaction models to account for the finite slipstream dimensions.

11.2. Recommendations

This section elaborates on the recommendations that should be taken into account when this thesis is used for future work. During the thesis, it was realized that the results could be improved such that the methods can be used for more realistic analyses.

- The current, only accurate, image correction approach is the full 3D image method. Unfortunately, this method is quite complicated due to the equations involved and to simplify the analysis, Rethorst applied multiple assumptions. Fortunately, the symmetry condition does not seem to be restrictive, since the analysis of a slipstream in the middle of the mid-span still shows good agreement with the CFD data. For further research into non-symmetric flow problems, the effect of the assumptions on the derivations of the equations should be investigated. Perhaps new equations can be defined for more general cases.

- The full 3D image method is used to calculate the effect of a single propeller slipstream. However, current distributed propeller aircraft have many slipstreams influencing the lift distribution. The influence matrix of the images of a single slipstream could theoretically be added to the influence matrix of another slipstream on the same wing. However, by this superposition, the interaction between the two slipstreams is not modeled. This superposition approach should be validated by CFD simulations such that discrepancies can be defined.

- The three correction methods discussed in this thesis are applied to the axial velocity component only. The 3D full image method, including the swirl component modeled as a change in angle of attack, showed a small discrepancy for the lift distribution, meaning the current approach of adding the swirl component should also be corrected. Future research should be performed to investigate the possibility of including the finiteness of the tangential velocity field by using a potential flow tool.

- The three correction methods are all based on the assumptions of a constant velocity throughout the jet. This would correspond to using the AD theory to define the flow field in front of the wing. However, real propeller slipstreams are not as simple as this and will have variations of the velocity components in all directions. The use of the BEM already includes the radial variation of the axial and tangential velocity. The influence of these variations in the current image correction method should be investigated. Perhaps, the same analyses can be performed by calculating a mean velocity value and using this in the potential flow tool.

- The potential flow propeller-wing analysis tools were validated in this thesis using the Euler equations in the CFD simulations. This was done to remove the effect of viscosity and to be sure that possible discrepancies are not originating from the used turbulence models. However, by neglecting all viscous effects, the analyses are not representative for real flows. CFD simulations including the viscous effects and a corresponding turbulence model should be performed to see if the results of full 3D image method show agreement with more accurate CFD simulations. Even better would be to analyze flow cases of which experimental wind tunnel data are available. In this way, the effect of the image correction method can be compared to the previously used empirical correction factors.

Bibliography

[1] J. D. Anderson. *Introduction to Flight*. 7th ed. McGraw-Hill (Education), 2011. ISBN: 978-0-07-108605-9.

[2] L. L. M. Veldhuis. *Propeller Wing Aerodynamic Interference*. PhD thesis. Delft University of Technology, 2005.

[3] D. P. Witkowski, A. K. H. Lee, and J. P. Sullivan. "*Aerodynamic Interaction Between Propellers and Wings*". *Journal of Aircraft* Vol. 26. No. 9 (1989), pp. 829–836. DOI: 10.2514/3.45848.

[4] APUS Group. *APUS I-6*. URL: https://apus-aero.com/aeronautical-engineering/i-planes/i-6/. (accessed: 03/04/2020).

[5] S. Clarke et al. "*SCEPTOR Power System Design: Experimental Electric Propulsion System Design and Qualification for Crewed Flight Testing*". *16th AIAA Aviation Technology, Integration, and Operations Conference* (2016). Washington, D.C.

[6] H. K. Epema. *Wing Optimisation for Tractor Propeller Configurations*. MSc thesis. Delft University of Technology, 2017.

[7] C. Alba. *A Surrogate-Based Multi-Disciplinary Design Optimization Framework Exploiting Wing- Propeller Interaction*. MSc thesis. Delft University of Technology, 2017.

[8] E. A. P. Marcus. *Aerodynamic Modelling and Performance Analysis of Over-the-Wing Propellers*. MSc thesis. Delft University of Technology, 2018.

[9] J. T. Goates. *An Enhanced Propeller Design Program Based on Propeller Vortex Lattice Lifting Line Theory*. MSc thesis. Utah State University, 2018.

[10] L. Ting and C. H. Liu. "*Thin Airfoil in Nonuniform Parallel Stream*". *Journal of Aircraft* Vol. 6. No. 2 (1969), pp. 173–175. DOI: 10.2514/3.44030.

[11] J. D. Anderson. *Fundamentals of Aerodynamics*. 5th ed. McGraw-Hill (Education), 2010. ISBN: 978-0-07-339810-5.

[12] A. C. Kermode. *Mechanics of Flight*. 11th ed. Pearson (Education), 2006. ISBN: 978–1–4058–2359–3.

[13] T. C. A. Stokkermans. *Design and Analysis of Swirl Recovery Vanes for an Isolated and a Wing Mounted Tractor Propeller*. MSc thesis. Delft University of Technology, 2015.

[14] I. Philipsen, H. Hoeijmakers and S. Hegen. "*An Overwiew of Advanced Propeller Simulation Tests in the German Dutch Wind Tunnels (DNW)*". *22nd AIAA Aerodynamic Measurement Technology and Ground Testing Conference* (2002). St. Louis, Missouri. DOI: 10.2514/6.2002-2920.

[15] A. W. Stuermer. "*Unsteady CFD Simulations of Propeller Installation Effects*". *AIAA/SAE/ASME/ASEE 28th Joint Propulsion Conference and Exhibit* (2006). Sacramento, California. DOI: 10.2514/6.2006-4969.

[16] A. Bacchini, E. Cestino and G. Romeo. *A Reduced Order Model to Estimating Propeller/Wing Interaction in Solar Powered Aircraft Preliminary Design*. Technical report. Politecnico di Torino, 2017.

[17] R. T. Johnston and J. P. Sullivan. "*Unsteady Wing Surface Pressures in the Wake of a Propeller*". *Journal of Aircraft* Vol. 30. No. 5 (1993), pp. 644–651. DOI: 10.2514/3.46393.

[18] B. R. Rakshith, S. M. Deshpande, R. Narasimha and C. Praveen. "*Optimal Low-Drag Wing Planforms for Tractor-Configuration Propeller-Driven Aircraft*". *Journal of Aircraft* Vol. 52. No. 6 (2015), pp. 1791–1801. DOI: 10.2514/1.C032997.

[19] T. Sinnige, T. C. A. Stokkermans, D. Ragni, G. Eitelberg and L. L. M. Veldhuis. "*Aerodynamic and Aeroacoustic Performance of a Propeller Propulsion System with Swirl-Recovery Vanes*". *Journal of Propulsion and Power* Vol. 34. No. 6 (2018), pp. 1376–1390. DOI: 10.2514/1.B36877.

[20] MIT. *Performance of Propellers*. URL: https://web.mit.edu/16.unified/www/FALL/thermodynamics/notes/node86.html. (accessed: 10/04/2019).

[21] Y. Yang. *Aerodynamic Interaction between Propeller and Vortex*. PhD thesis. 2017.

[22] G. J. D. Zondervan. "*A Review of Propeller Modelling Techniques Based on Euler Methods*". 1st ed. Delft University Press, 1998. ISBN: 978-9040715686.

[23] Aerodynamics for Students. *Analysis of Propellers; Glauert Blade Element Theory*. URL: `http://www-mdp.eng.cam.ac.uk/web/library/enginfo/aerothermal_dvd_only/aero/propeller/prop1.html`. (accessed: 10/04/2019).

[24] O. Gur and A. Rosen. "*Comparison between blade-element models of propellers*". *The Aeronautical Journal* Vol. 112. No. 1138 (2008), pp. 689–704. DOI: `10.1017/S0001924000002669`.

[25] M. H. McCrink and J. W. Gregory. "*Blade Element Momentum Modeling of Low-Reynolds Electric Propulsion Systems*". *Journal of Aircraft* Vol. 54. No. 1 (2017), pp. 163–176. DOI: `10.2514/1.C033622`.

[26] Y. A. P. Teeuwen. *Propeller Design for Conceptual Turboprop Aircraft*. MSc thesis. Delft University of Technology, 2017.

[27] Z. S. Montgomery. *A Propeller Model Based on a Modern Numerical Lifting-Line Algorithm with an Iterative Semi-Free Wake Solver*. MSc thesis. Utah State University, 2018.

[28] B. P. Epps and R. W. Kimball. "*Unified Rotor Lifting Line Theory*". *Journal of Ship Research* Vol. 57. No. 4 (2013). DOI: `10.5957/JOSR.57.4.110040`.

[29] I. Kroo. "*Propeller-Wing Integration for Minimum Induced Loss*". *Journal of Aircraft* Vol. 23. No. 7 (1986), pp. 561–565. DOI: `10.2514/3.45344`.

[30] J. Katz and A. Plotkin. *Low-Speed Aerodynamics*. 2nd ed. Cambridge University Press, 2010. ISBN: 978-0-521-66219-2.

[31] R. K. Prabhu. *Studies on the Interference of Wings and Propeller Slipstreams*. PhD thesis. Old Dominion University, 1984.

[32] M. D. Patterson and B. J. German. "*Simplified Aerodynamics Models to Predict the Effects of Upstream Propellers on Wing Lift*". *53rd AIAA Aerospace Sciences Meeting* (2015). Kissimmee, Florida. DOI: `10.2514/6.2015-1673`.

[33] M. D. Patterson, J. M. Derlaga and N. K. Borer. "*High-Lift Propeller System Configuration Selection for NASA's SCEPTOR Distributed Electric Propulsion Flight Demonstrator*". *16th AIAA Aviation Technology, Integration, and Operations Conference* (2016). Washington, D.C. DOI: `10.2514/6.2016-3922`.

[34] L. Ting, C. H. Liu and G. Kleinstein. "*Interference of Wing and Multipropellers*". *AIAA Journal* Vol. 10. No. 7 (1972), pp. 906–914. DOI: `10.2514/3.50244`.

[35] F. Chow, E. Krause, C. H. Liu and J. Mao. "*Numerical Investigations of an Airfoil in Nonuniform Stream*". *Journal of Aircraft* Vol. 7. No. 6 (1970), pp. 531–537. DOI: `10.2514/3.44208`.

[36] C. Koning. "Influence of the Propeller on Other Parts of the Airplane Structure". *Aerodynamic Theory* (1938), pp. 361–430. DOI: `10.1007/978-3-642-91487-4_4`.

[37] H. C. Garner, E. W. E. Rogers, W. E. A. Acum and E. C. Maskell. *Subsonic Wind Tunnel Wall Corrections*. AGARDograph 109, 1966.

[38] B. F. R. Ewald, ed. *Wind Tunnel Wall Corrections*. AGARDograph 336, 1998. ISBN: 92-836-1076-8.

[39] X. Liu. *Design of Swirl Recovery Vanes for Wing-Mounted Tractor Propeller Propulsion System*. MSc thesis. Delft University of Technology, 2018.

[40] S. Koltakov and O. B. Fringer. "*Moving grid method for numerical simulation of stratified flows*". *International Journal for Numerical Methods in Fluids* 71.12 (2013), pp. 1524–1545. DOI: `10.1002/fld.3724`.

[41] Converge CFD Software. *Numerical Viscosity*. URL: `https://convergecfd.com/resources/numerical-viscosity-convergent-science.pdf`. (accessed: 12/05/2019).

[42] M. Drelaand & H. Youngren. *XFOIL: an interactive program for the design and analysis of subsonic isolated airfoils*. `http://web.mit.edu/drela/Public/web/xfoil`. Accessed: 20/05/2019.

[43] Inc. ANSYS. *ANSYS CFX-Solver Theory Guide*. `http://read.pudn.com/downloads500/ebook/2077964/cfx_thry.pdf`. Accessed: 03/06/2019.

[44] T. C. A. Stokkermans, N. van Arnhem, T. Sinnige and L. L. M. Veldhuis. "*Validation and Comparison of RANS Propeller Modeling Methods for Tip-Mounted Applications*". *2018 AIAA Aerospace Sciences Meeting* (2018). DOI: `10.2514/6.2018-0542`.

[45] T. S. Phillips and C. J. Roy. "*Richardson Extrapolation-based Discretization Uncertainty Estimation for Computational Fluid Dynamics*". *Journal of Fluid Engineering* 136.12 (2014), pp. 401–410. DOI: 10.1115/1.4027353.

[46] L. Eça and M. Hoekstra. "*A procedure for the estimation of the numerical uncertainty of CFD calculations based on grid refinement studies*". *Journal of Computational Physics* 262 (2014), pp. 104–130. DOI: 10.1016/j.jcp.2014.01.006.

[47] H. Chung. *An Enhanced Propeller Design Program Based on Propeller Vortex Lattice Lifting Line Theory.* MSc thesis. MIT, 2007.

[48] J. J. A. van Kuijk. *Analysis of Swirl Recovery Vanes, Propulsion system performance and slipstream-wing interaction.* MSc thesis. Delft University of Technology, 2015.

[49] A. Deperrois. *XFLR5 — Analysis of Airfoils, Wings and Planes.* http://www.xflr5.tech/xflr5.htm. Accessed: 18/10/2019.

[50] S. Rethorst. "*Aerodynamic of Nonuniform Flows as Related to an Airfoil Extending Through a Circular Jet*". *Journal of the Aerospace Sciences* Vol. 25. No. 1 (1958), pp. 11–28. DOI: 10.2514/8.7479.

[51] W. F. Phillips and D. O. Snyder. "*Modern Adaptation of Prandtl's Classic Lifting-Line Theory*". *Journal of Aircraft* 37.4 (2000), pp. 662–670. DOI: 10.2514/2.2649.

[52] G. Kleinstein and C. H. Liu. "*Application of Airfoil Theory for Nonuniform Streams to Wing Propeller Interaction*". *Journal of Aircraft* Vol. 9. No. 2 (1972), pp. 137–142. DOI: 10.2514/3.44327.

[53] A. Jameson. "*Analysis of Wing Slipstream Flow Interaction*". *NASA* CR-1632 (1970).

[54] S. Kim and S. H. Rhee. "*Efficient Engineering Prediction of Turbulent Wing Tip Vortex Flows*". *Computer Modeling in Engineering & Sciences* 62.3 (2010), pp. 291–309. DOI: 10.3970/cmes.2010.062.291.

A

Difference between Contour Integration and Trapezoidal Method

In the 2D potential flow analysis of the airfoil submerged in a jet of finite height, multiple integrals were evaluated. Equations 4.20 and 4.21 were solved using a numerical method, namely the trapezoidal method. However, Ting gave a solution for these integrals in an analytical form by solving the integrals using contour integration [10]. Unfortunately, the values obtained by numerically evaluating the integrals are different compared to the the values resulting from the the presented analytical formulas [10]. This discrepancy is shown in Figure A.1. The numerical results were calculated with a large number of airfoil segments, at which the results converged. The values were calculated for the integral of J_0 for the first image set ($m = 0$), the first image of this set ($k = 1$) and for an slipstream of height c.

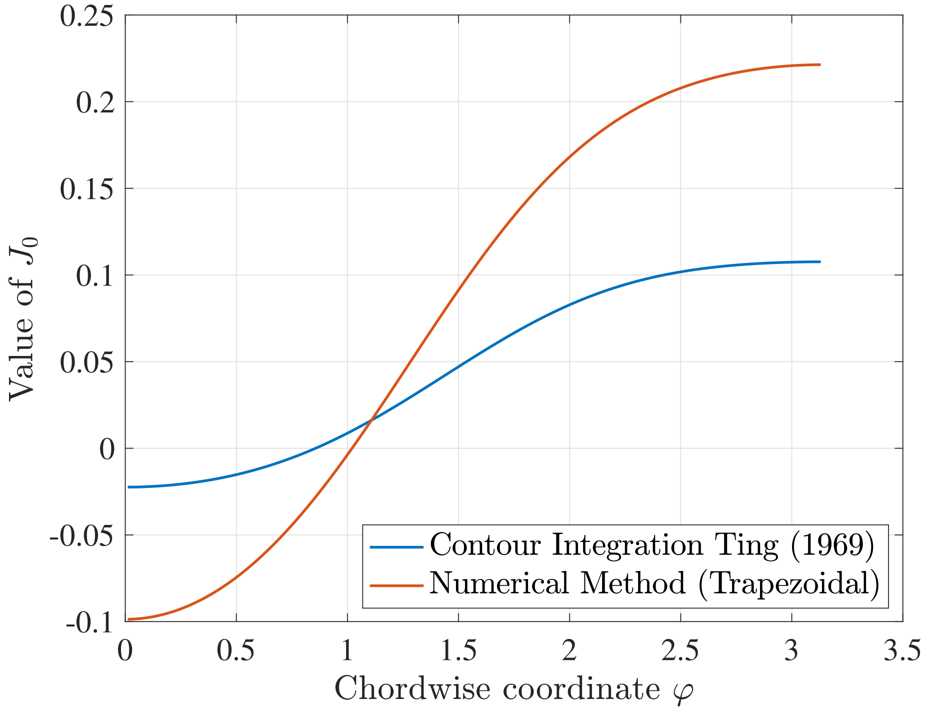

Figure A.1: Difference in integral values of J_0 for $m = 0$, $k = 1$, $h/c = 1$ and $a = b = h/2$ at different chordwise segments

Similar trends were observed for different values of m, k and h/c and also for the values of the different J_m integrals, see Figure A.2. It is unknown where the discrepancies come from, but it is assumed that the presented analytical equations are derived incorrectly or at least some typing errors are present in the discussed literature [10]. The incorrectness of these Equations was confirmed by the results of the 2D analysis and also by another research [31].

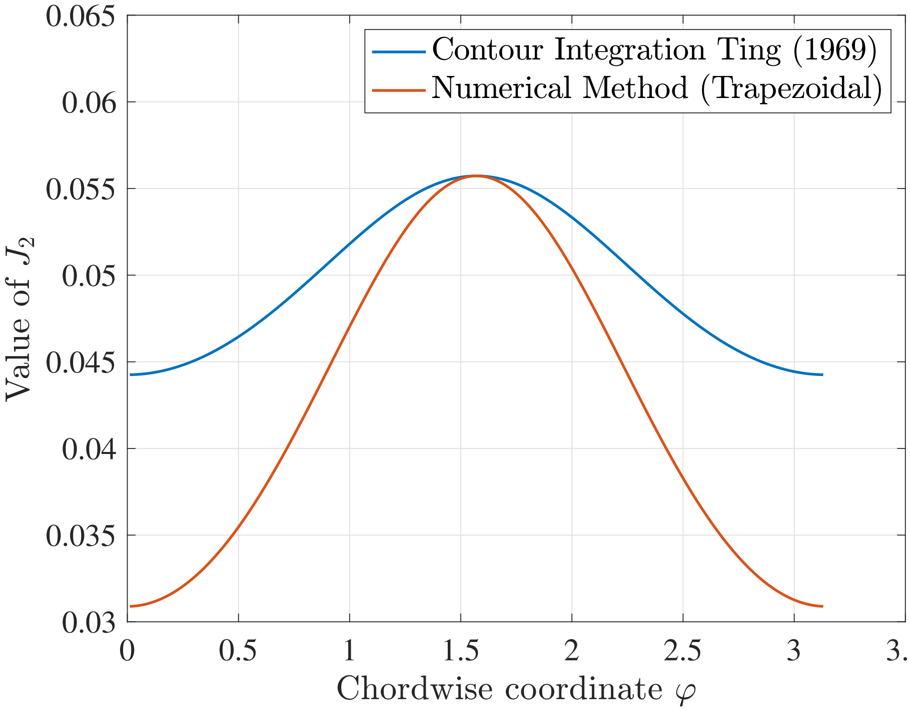

Figure A.2: Difference in integral values of J_2 for $m = 0$, $k = 1$, $h/c = 1$ and $a = b = h/2$ at different chordwise segments

B

2D Domain Convergence Study

For the 2D CFD simulations, a rectangular domain with sides of 100c was used. The smaller the domain, the larger the effect of the domain boundaries on the lift of the airfoil. In the potential flow method, it is assumed that the flow does not contain any disturbance infinitely far away form the airfoil. The proximity of the boundaries will result in additional flow components, similarly as those obtained by the effect of the finite slipstream height in the first place. The difficulty in determining the convergence trend of the lift coefficient with varying domain size is the corresponding mesh. Increasing the domain size will also increase the number of cells and hence change the average grid size. The mesh is finer close to the airfoil and depending of the proximity of the boundaries, this refinement region changes size.

In this domain size convergence study, it was tried to keep the meshes similar to one and another. The meshes were generated using ICEM CFD and the grid size was specified only on the domain boundaries, including the airfoil surface. The grid size specifications was kept the same for all domains. To remove the influence of the numerical viscosity as much as possible, the mesh size on the airfoil was set to a value of 0.001, similar to the used mesh for the converged CFD simulations of the airfoil in Figure 5.6. The results of the study can be seen in Figure B.1. Finally, the domain size of 100c was chosen since there was no significant increase in lift coefficient between the two last domain sizes ($< 0.1\%$). Furthermore, the use of a domain which was larger resulted in an increase in mesh cells and to have compromise between accuracy and computational time, the distance of 50c was used for the validation CFD simulations.

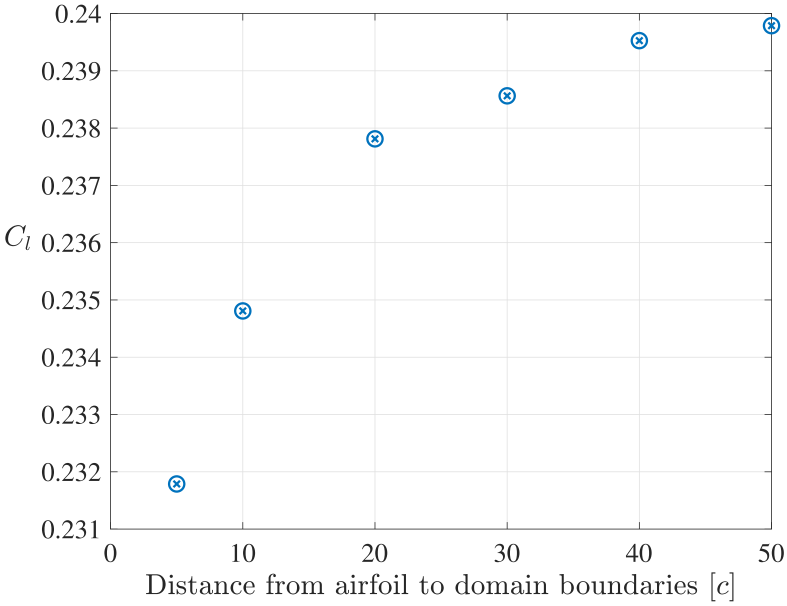

Figure B.1: Domain size convergence of C_l

C

Verification of the VLM

In the use of the intermediate and full 3D image methods, the lifting-line approach is enhanced to a single panel VLM technique, also known as the Weissinger approximation [50]. The verification of the VLM method was done to be sure that no programming errors were present and that the single panel VLM could be used for the mentioned correction methods. The analyzed case is the same as that of the CFD simulations, namely a straight wing with constant chord and no sweep or taper. The used airfoil was the NACA 0012 and the AR was set to 10. The wing was discretized into 100 panels for both methods. The results can be seen in Figure C.1, where VLM stands for the calculated results from the method described in Section 8.1. As can be seen, the results of the single panel VLM shows exact agreement with the results from XFLR5, verifying the implementation of the method.

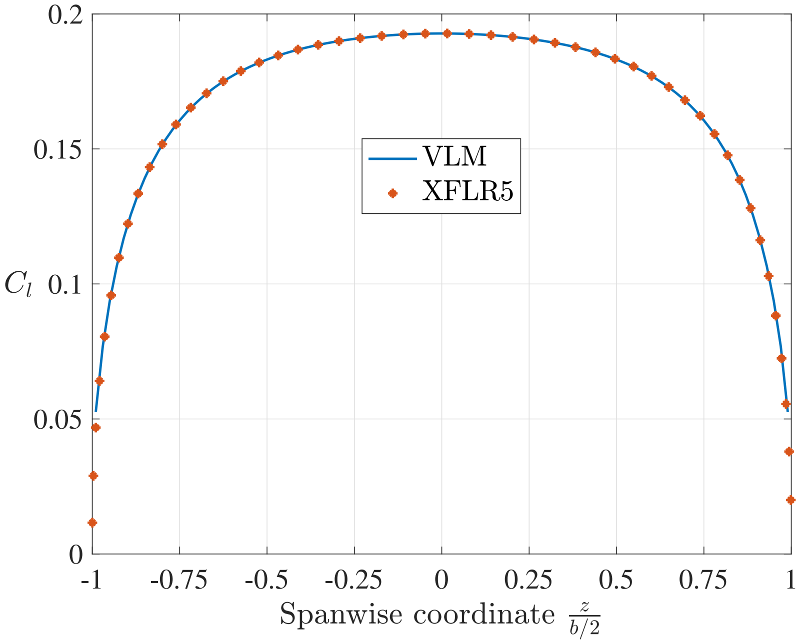

Figure C.1: Comparison between the implemented VLM method and the VLM analysis of XFLR5